

1-1-2012

## **Studies in Applied Materials Science: Drug-Biofluid Interactions and Light-Emitting Polymer Films**

Ashley Lynn Cornell

Follow this and additional works at: <https://scholarsjunction.msstate.edu/td>

---

### **Recommended Citation**

Cornell, Ashley Lynn, "Studies in Applied Materials Science: Drug-Biofluid Interactions and Light-Emitting Polymer Films" (2012). *Theses and Dissertations*. 4118.  
<https://scholarsjunction.msstate.edu/td/4118>

This Graduate Thesis - Open Access is brought to you for free and open access by the Theses and Dissertations at Scholars Junction. It has been accepted for inclusion in Theses and Dissertations by an authorized administrator of Scholars Junction. For more information, please contact [scholcomm@msstate.libanswers.com](mailto:scholcomm@msstate.libanswers.com).

STUDIES IN APPLIED MATERIALS SCIENCE: DRUG-BIOFLUID  
INTERACTIONS AND LIGHT-EMITTING POLYMER FILMS

By

Ashley Lynn Cornell

A Thesis  
Submitted to the Faculty of  
Mississippi State University  
in Partial Fulfillment of the Requirements  
for the Degree of Master of Science  
in Chemical Engineering  
in the Dave C. Swalm School of Chemical Engineering

Mississippi State, Mississippi

May 2012

Copyright 2012

By

Ashley Lynn Cornell

STUDIES IN APPLIED MATERIALS SCIENCE: DRUG-BIOFLUID  
INTERACTIONS AND LIGHT-EMITTING POLYMER FILMS

By

Ashley Lynn Cornell

Approved:

---

Keisha B. Walters  
Associate Professor  
(Director of Thesis and Advisor)

---

Priscilla J. Hill  
Associate Professor  
(Committee Member)

---

Bill B. Elmore  
Associate Professor and Hunter Henry Chair  
(Committee Member)

---

Rafael Hernandez  
Associate Professor and Texas Olefins  
Professorship  
(Graduate Coordinator)

---

Sarah A. Rajala  
Dean of the Bagley College of Engineering

Name: Ashley Lynn Cornell

Date of Degree: May 11, 2012

Institution: Mississippi State University

Major Field: Chemical Engineering

Major Professor: Dr. Keisha B. Walters

Title of Study: STUDIES IN APPLIED MATERIALS SCIENCE: DRUG-BIOFLUID INTERACTIONS AND LIGHT-EMITTING POLYMER FILMS

Pages in Study: 183

Candidate for Degree of Master of Science

*Interactions of Asthma Drugs with Artificial Saliva and Mucus.* Modeling pulmonary particulate transport requires related biofluid physicochemical properties. Aims included measuring the effects of common aerosol drugs on artificial saliva and diffusivities of asthma medications in mucus. Artificial saliva solutions doped with asthma medications were characterized by pH, interfacial tension, and rheology. To measure diffusion, drug concentration was monitored by time-dependent FTIR spectra, and diffusivity obtained using Fick's second law. Measured theophylline and albuterol diffusivities were ca.  $10^{-6}$  cm<sup>2</sup>/s.

*Surface Modification of Polymer Films with Light-Emitting Chemicals.* To develop a polymer film system that changed color in response to radiation, acid groups of poly(ethylene-co-acrylic acid) were used to attach two light-emitting polymers: 4'-(octyloxy)-4-biphenylcarboxylic acid and 2,7-bis(bromomethyl)-9,9-dihexyl-9H-fluorene. Each reaction step was confirmed using static contact angle goniometry, FTIR spectroscopy, and X-ray photoelectron spectroscopy. UV-Vis and fluorescence

spectroscopy measured the absorption spectra. Modified films were irradiated ( $\lambda=254$  nm) and produced blue emissions.

## DEDICATION

This thesis is dedicated to my fiancé and best friend, Zach Wynne, who never lets me give up on myself and cheers me on in every aspect of life, my parents, Mark and Linda Cornell, for always encouraging me and supporting every one of my adventures, and to my sister Chelsea, for always making me laugh when I need it most.

## ACKNOWLEDGEMENTS

These research efforts could not have been completed without the help and assistance of many people. Most importantly, I'd like to thank my advisor Dr. Keisha Walters. Without her giving me a chance to prove myself, I would never have achieved as much as I did or really learned my true potential. Her academic and personal guidance has transformed a graduate degree from a dream to a reality, and I'm grateful to have had such an excellent advisor during this process. I'd also like to thank the members of my committee, Dr. Bill Elmore and Dr. Priscilla Hill, for their time and feedback both in the classroom and in my research throughout my time at MSU.

The other graduate students in the PolySEL group have contributed in so many ways to my research as well as my overall experience at Mississippi State. They have not only helped in endless ways in the lab and in the classroom, but I truly value their friendship as well. Thank you Caitlin Naske, Zach Wynne, Erick Vasquez, Ersan Eyiler, Mat Rowe, and Maryam Dadgarmoghaddam!

I'd also like to thank my family, who have supported me in every endeavor, have offered advice whenever needed, and can always make me laugh. I learned my work ethic from my dad, perseverance from my mom, and sense of humor and optimism from my sister. The love and encouragement of my fiancé and best friend Zach has also been essential to my achievements in graduate school. Without them, I would not be where I am today.



I greatly appreciate all of the help from Dr. Jonathan Frisch with the UV-Vis and fluorescence spectroscopy on the light-sensitive films project, as well as Maria Cebada-Ricalde for her help with UV illumination of the films. Thank you to Ersan Eyiler for running XPS on my samples, and to Dr. Mark Bricka for use of the rheometer. Also, thank you to Jennifer Miller with help running samples. Thank you to Entergy and the National Science Foundation [EPS-0903787], through the Mississippi EPSCoR program, for funding this research.

## TABLE OF CONTENTS

	Page
DEDICATION .....	ii
ACKNOWLEDGEMENTS .....	iii
LIST OF TABLES .....	x
LIST OF FIGURES .....	xi
CHAPTER	
I. INTRODUCTION TO ARTIFICIAL SALIVA, AEROSOL DRUGS, AND MODELING DIFFUSION OF DRUGS THROUGH PULMONARY MUCUS .....	1
1.1 Background .....	1
1.2 Types of Asthma Treatments .....	3
1.3 Saliva .....	5
1.4 Mucus .....	6
1.5 Drug Inhalation, Deposition, and Diffusion .....	8
1.6 Research Objectives .....	10
1.7 References .....	11
II. CHARACTERIZATION OF THE PHYSICOCHEMICAL PROPERTIES OF NEAT AND DRUG-DOPED ARTIFICIAL SALIVA .....	13
2.1 Abstract .....	13
2.2 Introduction .....	14
2.3 Materials and Methods .....	17
2.3.1 Drugs .....	17
2.3.2 Artificial Saliva Components and Modifying Substances .....	17
2.3.3 Preparation of Standard Artificial Saliva Solutions .....	18
2.3.4 Preparation of Altered Artificial Saliva Solutions .....	19
2.3.5 pH Measurements of Neat and Drug-Doped Artificial Salivas .....	20
2.3.6 Interfacial Tension Measurements .....	20
2.3.7 Shear Rate and Viscosity Measurements .....	21

2.4	Results.....	21
2.4.1	pH of Neat Saliva Solutions and Drug-Doped Saliva Solutions .....	21
2.4.2	Interfacial Tension .....	23
2.4.3	Rheology.....	30
2.5	Conclusions.....	35
2.6	References.....	37
III.	DIFFUSION OF THEOPHYLLINE AND ALBUTEROL THROUGH ARTIFICIAL MUCUS .....	39
3.1	Abstract.....	39
3.2	Introduction.....	39
3.2.1	Mucus Diffusion using ATR-FTIR.....	43
3.3	Materials and Methods.....	46
3.3.1	Materials .....	46
3.3.1.1	Diffusants.....	46
3.3.1.2	Preparation of Artificial Mucus .....	47
3.3.2	Methods: FTIR Spectroscopy .....	47
3.4	Results and Discussion .....	48
3.4.1	Data Collection .....	48
3.4.2	Data Analysis.....	51
3.5	Conclusions.....	58
3.6	References.....	59
IV.	INTRODUCTION TO POLYMER SURFACE MODIFICATION USING LIGHT-EMITTING POLYMERS .....	61
4.1	Background: Polymer Surface Modification .....	61
4.2	Uses of Light-Emitting Polymers .....	64
4.3	Classes of Light-Emitting Polymers.....	66
4.4	Research Objectives.....	70
4.5	Approach.....	71
4.6	References.....	72
V.	MODIFICATION AND CHEMICAL GRAFTING OF POLY(ETHYLENE-CO-ACRYLIC ACID) FILMS .....	75
5.1	Abstract.....	75
5.2	Introduction.....	75
5.3	Materials and Methods.....	79
5.3.1	Materials .....	79
5.3.2	FTIR Spectroscopy .....	79
5.3.3	Contact Angle Goniometry.....	80
5.4	Results and Discussion .....	80
5.4.1	Preliminary Reactions of EAA Film.....	80

5.4.2	Primary Reactions of EAA Films .....	82
5.4.2.1	Reaction Path “A”: Grafting of OBC.....	82
5.4.2.2	Reaction Path “B”: Grafting of BDMF.....	85
5.4.3	Static Contact Angle Results .....	90
5.5	Conclusions.....	93
5.6	References.....	94
VI.	OPTICAL PROPERTY CHARACTERIZATION OF EAA-OBC AND EAA-BDMF POLYMER FILMS .....	96
6.1	Abstract.....	96
6.2	Introduction.....	97
6.3	Materials and Methods.....	99
6.3.1	Materials .....	99
6.3.2	Methods.....	100
6.3.2.1	UV-Vis Spectroscopy .....	100
6.3.2.2	Fluorescence Spectroscopy.....	100
6.3.2.3	UV Lamp Illumination.....	100
6.3.2.4	FTIR Spectroscopy .....	100
6.4	Results and Discussion .....	101
6.4.1	UV-Vis Spectroscopy .....	101
6.4.2	Fluorescence Spectroscopy.....	102
6.4.3	UV Lamp Illumination.....	105
6.4.4	FTIR and Fluorescence Spectroscopy of 6 Month Old Films .....	106
6.5	Conclusions.....	111
6.6	References.....	112
VII.	RECOMMENDATIONS .....	113
7.1	Recommendations for Artificial Saliva .....	113
7.2	Recommendations for Light-sensitive Polymer Films .....	114
APPENDIX		
A	FTIR METHODS: ATR, TRANSMISSION, AND DRIFTS .....	116
A.1	FTIR Methods: ATR, Transmission, and DRIFTS.....	117
A.2	FTIR Set-Up.....	117
A.3	Data Collection and Use of OMNIC Software .....	121
A.4	Sample Set-Up .....	128
A.4.1	Veemax II ATR.....	128
A.4.2	MIRacle ATR.....	131
A.4.3	DRIFTS.....	132
A.4.4	Transmission FTIR .....	134

B	SURFACE ANALYSIS AND DEPTH OF PENETRATION: A COMPARISON OF DIFFERENT SURFACE-SENSITIVE FTIR TECHNIQUES .....	136
B.1	Introduction to Surface Chemistry Characterization Methods .....	137
B.2	Depth of Penetration .....	141
B.3	Depth of Penetration: Comparing ATR Techniques.....	142
B.4	Comparing spectra of ATR Techniques .....	143
B.5	References.....	145
C	COMPRESSION MOLDER OPERATIONAL GUIDELINES AND PRODUCTION OF EVOH FILMS USING COMPRESSION MOLDING.....	146
C.1	Compression Molder Operational Guidelines .....	147
C.2	Using the Compression Molder to Make EVOH Films.....	150
D	CONTACT ANGLE GONIOMETRY OPERATIONAL GUIDELINES FOR DATA COLLECTION AND ANALYSIS .....	152
D.1	Instrument Specifications.....	153
D.2	Instrument Set-Up.....	153
D.3	Static Contact Angle .....	155
D.4	Pendant Drop .....	156
D.5	References.....	158
E	DETERMINATION OF OPTIMAL REACTION TIMES FOR PRELIMINARY EAA SURFACE MODIFICATION STEPS .....	159
E.1	Determination of Optimal Reaction Times for Preliminary EAA Surface Modification Steps.....	160
E.2	References.....	165
F	GRATING OF POLY(ETHYLENE GLYCOL DIACRYLATE) TO AMINE SURFACE-MODIFIED EAA FILMS.....	166
F.1	Introduction.....	167
F.2	Results.....	167
F.3	References.....	171
G	NANOPARTICLES IN DRUG DIFFUSION .....	172
G.1	Introduction.....	173
G.2	Characteristics of Nanoparticles .....	173
G.3	Fate of Nanoparticles in the Lung.....	175
G.4	Nanoparticles in Inhalation Medicine.....	176
G.5	Toxicity of Nanoparticles .....	179

G.6	Conclusions.....	180
G.7	References.....	182

## LIST OF TABLES

TABLE		Page
2.1	Artificial Saliva Compositions [Preetha and Banerjee, 2005].	19
3.1	Summary of measured diffusivity coefficients for theophylline and albuterol in artificial mucus.	57
5.1	Summary of average contact angle values for surface-modified EAA films at each reaction step.	92
B.1	Tabulated Summary of Commonly used ATR-FTIR Crystal Properties Important for Crystal Selection [Pike Technologies, 2011].	139
B.2	Table of Refractive Indices [Kazarian and Chan, 2010], Incidence Angles, and Calculated Depth of penetration ( $d_p$ ) ranges for an EAA film sample ( $n_2=1.408$ ) for the four ATR crystal options available in our laboratories.	143
D.1	Reference static contact angles for standard materials.	157
E.1	Carbonyl peak height values for the transformation from carboxylic acid ( $1700\text{ cm}^{-1}$ ) to acid chloride ( $1795\text{ cm}^{-1}$ ) during the reaction of EAA with $\text{PCl}_5$ to form EAA-Cl.	162
E.2	Peak height values for functional groups of interest in the reaction of EAA-Cl to EAA-NH <sub>2</sub> .	164

## LIST OF FIGURES

FIGURE	Page
1.1 Chemical structures of the asthma treatments used in this study: albuterol, theophylline, KI, and fluticasone propionate and salmeterol xinafoate, respectively, which in combination constitute Advair®. ....	5
1.2 Depiction of gel and sol mucus layers above the pulmonary epithelial cells with cilia penetrating the sol layer. ....	7
1.3 Depiction of human lung generations. ....	9
2.1 Chemical structures of asthma drugs used in this study. ....	17
2.2 pH data for neat and drug-doped artificial saliva solutions. ....	22
2.3 Average interfacial tension values for three artificial salivas (X1, X2, and Saliveze) and natural saliva [A: Preetha and Banerjee, 2005; B: Kasakov, 2009]. Error bars represent 95% confidence intervals. ....	25
2.4 Comparison of IFT for artificial saliva solutions with and without the addition of mucus and/or phosphatidylserine (PS), compounds representative of those found in natural saliva. ....	26
2.5 Interfacial tension of drug-doped X1 saliva solution. IFT of neat X1 (67.24 mN/m) indicated by blue dashed line. ....	27
2.6 Interfacial tension of drug-doped X2 saliva solution. IFT of neat X2 (69.31 mN/m) indicated by blue dashed line. ....	28
2.7 Interfacial tension of drug-doped saliveze saliva solution. IFT of neat saliveze (IFT 67.05 mN/m) indicated by blue dashed line. ....	29
2.8 Viscosity versus shear rate for neat artificial saliva solutions and natural saliva [*Preetha and Banerjee, 2005, ^Vissink et al., 1984]. ....	32
2.9 Plot of viscosity versus shear rate for comparison of neat xialine 1 to drug-doped xialine 1. ....	33



2.10	Plot of viscosity versus shear rate for comparison of neat xialine 2 to drug-doped xialine 2.....	34
2.11	Plot of viscosity versus shear rate comparing neat (unmodified) saliveze to drug doped saliveze.....	35
3.1	Illustration of gel-sol mucus structure above the pulmonary epithelial cells with beating cilia penetrating the sol layer. ....	41
3.2	Chemical Structures of theophylline (left) and albuterol (right).....	46
3.3	Schematic of the experimental FTIR diffusion set-up. The artificial mucus layer is sandwiched between a layer of the drug-doped solution and the ATR-FTIR crystal. Not to scale. ....	48
3.4	ATR-FTIR spectra for a concentration series of theophylline in IPA. ....	49
3.5	Time-resolved ATR-FTIR spectra collected over 600 sec for the diffusion of a 25 mg/mL theophylline/IPA solution through a 3.5 mm artificial mucus layer.....	50
3.6	Stacked spectra of the artificial mucus components. Boxed peaks around $\sim 1640\text{ cm}^{-1}$ are of interest due to the overshadowing the peaks have on secondary amine peaks in the drugs.....	51
3.7	Theophylline concentration profile based on measured FTIR peak height fitted to a linear function. ....	52
3.8	Schematic representation of boundary conditions applied to the mucus-drug diffusion system. ....	54
3.9	Comparison of experimental and calculated concentrations for a 10-mg/mL theophylline-IPA solution diffusing through an artificial mucus layer.....	56
4.1	Chemical structure of poly( <i>p</i> -phenylenevinylene) (PPV).....	67
4.2	Chemical structure of polyacetylene (PA). ....	68
4.3	Chemical structure of polyfluorene (PF).....	69
4.4	Chemical structure of the repeat unit for polydiacetylene (PD).....	70
4.5	Chemical structure of 4'-(octyloxy)-4-biphenyl carboxylic acid (OBC). ....	71
4.6	Chemical structure of 2,7-bis (bromomethyl)-9,9-dihexyl-9H-fluorene (BDMF).....	71

5.1	Chemical structures of OBC (a) and BDMF (b). .....	78
5.2	Reaction schematic of the preliminary reaction steps of EAA prior to reactions with light-sensitive chemicals.....	81
5.3	ATR-FTIR spectra of preliminary film reactions steps: (a) EAA-Neat, (b) EAA-Cl, (c) and EAA-NH <sub>2</sub> . .....	81
5.4	Conversion of carboxylic acid of OBC chemical to acid chloride.....	83
5.5	Reaction schematic of the reaction steps of EAA-NH <sub>2</sub> with acid chloride converted OBC chemical to EAA-OBC.....	83
5.6	ATR-FTIR spectra of preliminary film reactions steps: EAA-Neat (a), EAA-Cl (b), EAA-NH <sub>2</sub> (c), and EAA-OBC (d).....	84
5.7	FTIR spectral comparison of OBC chemical and EAA-OBC reacted film. The peaks used to identify OBC on the surface of EAA-OBC are boxed around both spectra.....	85
5.8	Reaction schematic of the reaction steps of EAA-NH <sub>2</sub> with BDMF chemical to form EAA-BDMF.....	86
5.9	ATR-FTIR spectra of preliminary film reactions steps: EAA-Neat (a), EAA-Cl (b), EAA-NH <sub>2</sub> (c), and EAA-BDMF (d). .....	87
5.10	FTIR spectral comparison of BDMF chemical and EAA-BDMF reacted film. The peaks used to identify BDMF on the surface of EAA-BDMF are boxed around both spectra.....	88
5.11	Transmission FTIR spectra of the preliminary step reaction films, as well as the final reaction products, EAA-OBC and EAA-BDMF. ....	89
5.12	Representative image of a sessile droplet showing the intermolecular forces used to calculate the static contact angle.....	91
5.13	From left, EAA-Neat, EAA-Cl, EAA-NH <sub>2</sub> , and EAA-OBC static contact angle images. ....	93
5.14	From left, EAA-Neat, EAA-Cl, EAA-NH <sub>2</sub> , and EAA-BDMF static contact angle images. ....	93
6.1	Chemical structures of OBC (a) and BDMF (b). .....	98
6.2	Visible spectrum with wavelengths for each color range [Madigan, 2011].....	99
6.3	UV-Vis spectra for EAA-Neat, EAA-Cl, EAA-NH <sub>2</sub> , and EAA-OBC.....	101

6.4	UV-Vis spectra for EAA-Neat, EAA-Cl, EAA-NH <sub>2</sub> , and EAA-BDMF.....	102
6.5	FS spectra for EAA-Neat, EAA-Cl, EAA-NH <sub>2</sub> , and EAA-OBC.....	103
6.6	FS spectra for EAA-Neat, EAA-Cl, EAA-NH <sub>2</sub> , and EAA-BDMF.....	104
6.7	Films prior to UV irradiation (a) and during irradiation (b). ....	105
6.8	MIRacle-ATR FTIR spectral comparison of newly made EAA-OBC film with EAA-OBC film after 6 months.....	106
6.9	MIRacle ATR FTIR spectral comparison of newly made EAA-BDMF film with EAA-BDMF film after 6 months. ....	107
6.10	FS spectra of EAA-OBC film after six months and newly made EAA- OBC film for comparison.....	108
6.11	FS spectra of EAA-BDMF film after six months and newly made EAA- BDMF film for comparison.....	109
6.12	UV illumination of six month old EAA-BDMF (left) and EAA-OBC (right) at a wavelength of 254 nm. ....	110
A.1	Airline valve setup in PolySEL Lab 180.....	118
B.1	Spectra collection using a single-bounce attenuated total reflectance (ATR) FTIR accessory. ....	141
B.2	Comparison of MIRacle and Veemax ATR spectra for an EAA-NH <sub>2</sub> film with absorbance presented on a common scale. ....	144
C.1	Main power source switch.....	147
C.2	Picture indicating red switch for powering compression molder.....	148
C.3	Instrument control panel.....	148
C.4	Carver, Inc. compression molder (model 3893.4PR1A00). ....	149
C.5	EVOH film produced at 190° C and 4000 lb <sub>f</sub> without drying pellets. ....	151
C.6	EVOH film produced at 190° C 4000 lbs. with dried pellets.....	151
D.1	Kruss EasyDrop Contact Angle Goniometer with syringe loaded.....	153
D.2	Images depicting the proper syringe (left) and syringe plunger (right) placement on the Kruss EasyDrop Contact Angle Goniometer. ....	154

E.1	Primary reaction steps for surface modification of EAA film: conversion of carboxylic acid to acid chloride using $\text{PCl}_5$ and subsequent conversion to primary amines using ethylene diamine. ....	160
E.2	ATR-FTIR spectra of EAA-Cl films at reaction times of 0, 5, 15, 35, and 45 minutes showing progressive decrease in the acid carbonyl (at $\sim 1700 \text{ cm}^{-1}$ ) and increase in the acid chloride carbonyl (at $\sim 1795 \text{ cm}^{-1}$ ). ....	161
E.3	ATR-FTIR spectra of EAA-NH <sub>2</sub> films at reaction times of 0, 60, 90, and 150 min and 24 hours—with and without sonication. Sonicated films had complete surface reaction with the ethylene diamine, while unsonicated films contained some unreacted surface -Cl groups (presence of peak at $\sim 1800 \text{ cm}^{-1}$ ). ....	163
F.1	Chemical structure of poly(ethylene glycol diacrylate) (PEGD). ....	167
F.2	Reaction scheme for the reaction of PEGD with EAA-NH <sub>2</sub> . ....	169
F.3	ATR-FTIR spectra of EAA-NH <sub>2</sub> (2), EAA-PEGD575-Acetone (3a), EAA-PEGD575-Toluene (3b), EAA-PEGD258-Acetone (4a) and EAA-PEGD258-Toluene (4b). Spectral peaks of interest are boxed. ....	170

CHAPTER I  
INTRODUCTION TO ARTIFICIAL SALIVA, AEROSOL DRUGS, AND MODELING  
DIFFUSION OF DRUGS THROUGH PULMONARY MUCUS

**1.1 Background**

The implementation of inhalation aerosol drugs has been one of the most successful and effective treatments for respiratory illnesses. This delivery mechanism has allowed for the direct application of therapeutic drugs to damaged, diseased, or distressed lungs needing immediate treatment. Asthma is one of the most common respiratory illnesses treated by aerosol drugs. Studies of the various types of inhalation drugs have led to improvements in the treatment of asthma and how they can promote reversal of bronchoconstriction (immediate response treatment) or act as preventative agents to provide continuous systemic therapy against the emergence of bronchoconstriction [Volsko and Reed, 2000].

Aerosols are also being investigated as treatments for other ailments, such as diabetes. An inhalation form of insulin called Oralin<sup>®</sup>, a high-velocity fine particle aerosol, was developed as an alternate delivery method for insulin for diabetic patients. The invasiveness of current diabetes treatments provoked the interest in using aerosols to control the disease. The small particle size and direct deposition into the lungs resulted in more rapid absorption and metabolic control than the previous methods of subcutaneous injection [Modi, 2005]. Insulin bioavailability can reach 37% with inhalation administration as opposed to 1% via oral, sublingual nasal or transdermal administration

[Todoroff and Vanbever, 2011]. Infection in the lungs of cystic fibrosis (CF) patients is also an ailment for which the use of aerosol drugs is being investigated. *Pseudomonas aeruginosa* is an infection that is nearly impossible to cure with antibiotics and is a leading cause of death in CF patients. Due to the denser, more highly glycosylated pulmonary mucus of CF patients, it is increasingly difficult to diffuse any treatments through these layers to treat the *P. aeruginosa*. Photodynamic antimicrobial therapy was found to be a successful treatment by delivering photosensitizers to the lungs through inhalation. Delivery of red light at 635 nm and two photosensitizers across artificial CF mucus was successful, validating the theory of using aerosols as treatments for CF complications [Donnelly et al., 2007, Khanvilkar et al., 2001]. Recent research has also investigated the use of nanoparticle agglomerate suspensions composed of asthma treatments fluticasone and/or albuterol. The resulting aerosols contained an ideal water-soluble nanostructure as well as a range of particle diameters from 1-5 micron, which can be tailored for localized treatments. This method would be a solution to the recurring issue of drug particle size, exhalation of nanoparticle (>0.5-1 micron in diameter) sized drugs, and poor water solubility by some drugs in saliva and pulmonary mucus. A tailored drug particle size avoids the physiological barriers of the lung physiology and delivers the drug to the desired lung region [El-Gendy et al., 2011, Todoroff and Vanbever, 2011].

Along with research on current and developing treatments for asthma, other factors affecting the efficiency of aerosol treatments need to be investigated to result in the most effective treatment for lung inflammation. Saliva, being the ultimate carrier of the aerosols to the lungs, needs to be considered when engineering aerosol drugs, as well as the pulmonary mucus that serves as a protective barrier for the lungs while obstructing

the diffusion of the drugs to the lung surface. Drugs need to be designed to diffuse through the viscous mucus layer quickly while retaining their medicinal properties. Model mucus membranes have been developed, as well as mathematic simulation models for the diffusion of the drugs through mucus. Lipophilicity has been found to be one of the most influential characteristics of the ability of drug diffusion, as well as particle size [Larhed et al., 1997].

The deposition patterns and diffusion mechanisms of the drugs are also under intense investigation. Understanding drug properties, deposition patterns, drug-mucus interactions, and drug diffusion will ultimately lead to the development of the least invasive, most effective drug that will diffuse the lung mucus at the highest concentration and in the fastest manner. Developments in this field could contribute to an even wider range of illnesses being treated with aerosol drugs.

## **1.2 Types of Asthma Treatments**

Aerosols are frequently used as a delivery mechanism in the lungs for the treatment of respiratory and systemic illnesses. Compared to other drug delivery methods, smaller dosages, low cost and minimal side effects, bypassing of the digestive system, non-invasiveness, chemical stability, patient compliance, and faster action make inhalation drug delivery worth further investigation and development [Chan, 2006].

Significant advances have been made, especially in the past decade, for the treatment of respiratory illnesses via pulmonary drug delivery [Chan, 2006]. Treatments range from fast acting rescue  $\beta_2$ -receptor agonists and systemic corticosteroids to long-term medications that prevent lung inflammation and control of diseases such as asthma [Chan, 2006; Volsko and Reed, 2000]. Aerosol fast-acting  $\beta_2$ -receptor agonists are

typically the treatment of choice of most physicians due to their effectiveness in relaxing the bronchoconstriction by binding to the  $\beta_2$ -receptors of the bronchial smooth muscle. Fast acting  $\beta_2$ -receptor agonists also have minimal systemic absorption and side effects. Corticosteroids, when administered short-term and in high doses, can speed the resolution of bronchoconstriction as well as lessen the likelihood of relapse. Systemic effects limit this treatment to short term for acute attacks [Volsko and Reed, 2000]. Long-term treatments are administered to patients to provide continuous therapy and eliminate or lessen the frequency and severity of attacks. These drugs prevent the bronchoconstriction that cause asthma attacks as well as control acute symptoms. Treatment types include long-acting  $\beta_2$ -receptors, corticosteroids, and leukotriene modifiers, which block the immune system chemicals that cause asthma symptoms, leukotrienes, from affecting the body [Mayo Clinic, 2010].

Some of the most common drugs used in the treatments of asthma include albuterol/salbutamol, a short-acting  $\beta_2$ -receptor agonist, prednisone, a systemic corticosteroid, salmeterol and theophylline, both long-acting  $\beta_2$ -receptor agonists, or an anti-inflammatory corticosteroid, such as fluticasone [Volsko and Reed, 2000]. Other long-term treatments include drugs such as Advair<sup>®</sup>, a salmeterol-fluticasone propionate mixture and Singulair<sup>®</sup>, a leukotriene modifier comprised of montelukast sodium. Theophylline was one of the most widely used treatments for asthma for decades as both a fast-acting and long-acting treatment, however, due to misuse, abuse, toxicity with high doses, and difficulty determining the optimal dosage [Volsko and Reed, 2000], albuterol surpassed theophylline as the leading treatment for fast-acting asthmatic management. Theophylline is still used as a long-term treatment, but with increased patient monitoring. Albuterol/salbutamol, on the other hand, is most commonly used in rescue situations as a



response to an asthma attack. Albuterol is one of the most effective immediate treatments when inhaled via aerosol inhaler, since it provides direct effect to the inflamed bronchial smooth muscle. Potassium iodide (KI), an expectorant, is another treatment that thins mucus secretions in the respiratory tract, making it easier for patients to clear the airway by coughing. KI is not a commonly used treatment for asthma. This research focuses on four asthma treatments: albuterol/salbutamol, theophylline, KI, and Advair<sup>®</sup>. The chemical structures of these drugs can be seen in Figure 1.1.

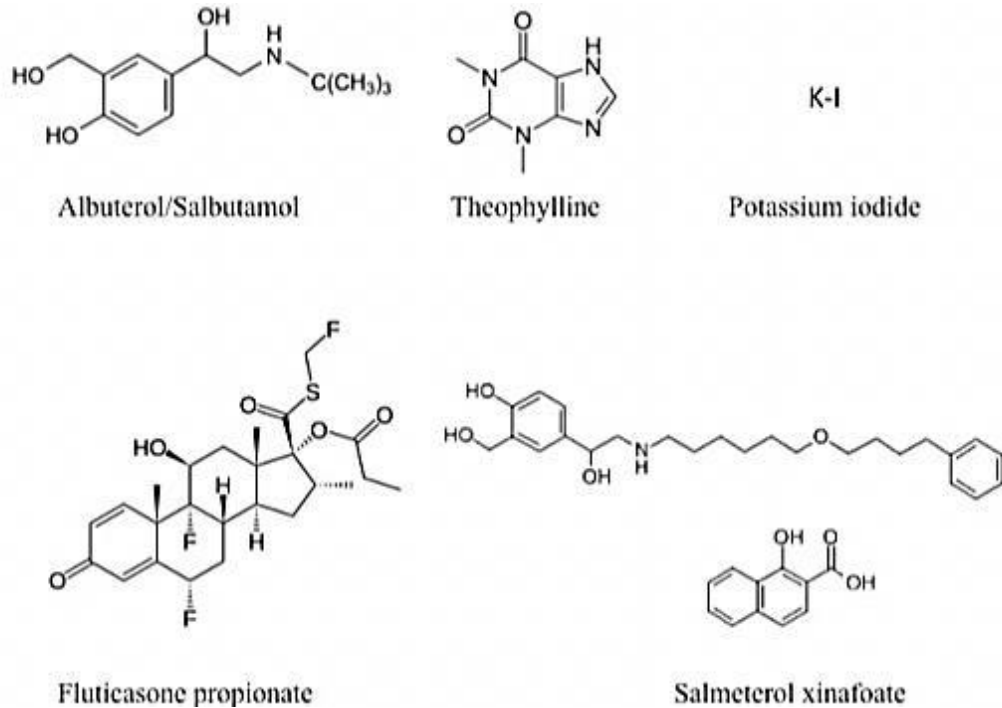


Figure 1.1 Chemical structures of the asthma treatments used in this study: albuterol, theophylline, KI, and fluticasone propionate and salmeterol xinafoate, respectively, which in combination constitute Advair<sup>®</sup>.

### 1.3 Saliva

Saliva is a complex biological fluid that first contacts the inhaled pharmaceuticals. The three human salivary glands, parotid, submandibular, and sublingual glands [Rossetti

et al., 2008], secret saliva at a rate of approximately 1.5 liters per day [Preetha and Banerjee, 2005, Juniper et al., 1995]. It is an aqueous non-Newtonian slightly alkaline fluid comprised primarily of water, lipids, glycoproteins, and digestive enzymes [Preetha and Banerjee, 2005]. Saliva has many functions that contribute to mouth lubrication, digestion, management of oral microbes [Rossetti et al., 2008], and has recently been investigated as a biomarker for diseases and the detection of systemic illnesses [Schipper et al., 2007].

Artificial saliva can act as a close replicate for patients who lack an adequate amount of natural saliva to satisfy the body's functions. Artificial salivas must be as close as possible in a biophysical capacity to the physiological properties of natural saliva. For research purposes, artificial salivas must model natural saliva accurately for the validity of any conclusions. Properties such as viscosity, wettability, interfacial and viscoelastic tension, and uniformity must be closely replicated [Levine, 1993].

#### **1.4 Mucus**

Mucus is a viscous secreted fluid that is produced by goblet cells and sub-mucosa glands of mucous membranes as a protective barrier [Todoroff and Vanbever, 2011, Hombach and Bernkop-Schnurch, 2010]. It is secreted at a rate of approximately one liter per day in the human body [Hombach and Bernkop-Schnurch, 2010]. Mucus contains antiseptic enzymes, immunoglobulins, proteins, and glycoproteins (mucins). It covers the entire airway and protects the membrane against bacteria and other foreign agents that enter the lung. Mucus exists in two layers: an upper gel phase and a lower sol phase. The upper gel phase is 95% water, 2% mucin, and the remainder salts, proteins, and lipids. The lower sol layer is less viscous, which allows for cilia beating [Todoroff and

Vanbever, 2011]. Figure 1.2 illustrates the setup of the gel-sol mucus layer on top of the pulmonary epithelial cells and beating cilia.

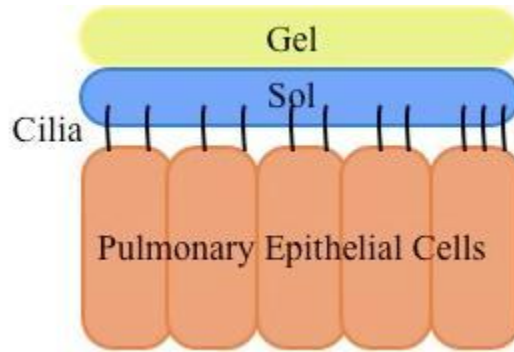


Figure 1.2 Depiction of gel and sol mucus layers above the pulmonary epithelial cells with cilia penetrating the sol layer.

In the respiratory system, the mucus protects the lungs by trapping foreign particles that enter the respiratory tract and lungs. By protecting the lungs from foreign particles, the lung mucus also acts as a barrier that impedes the diffusion of drug particulates. The structure of the mucosal barrier is one of the most influential factors against the diffusion of particles. Mucin causes the viscoelastic property of mucus and is the backbone of the cross-linked network structure of mucus. [Khanvilkar et al, 2001]. The crosslinking phenomenon is caused by disulfide bridges and hydrophobic bonds of polymerized mucin aggregate rods [Khanvilkar et al, 2001]. In addition, mucus is hydrophobic due to the presence of several phospholipids [Khanvilkar et al, 2001].

When making artificial mucus, several factors must be considered. The artificial mucus must be close in viscosity to natural mucus in order to accurately mimic the viscosity differences between mucus and saliva. In using a more complex artificial mucus network, any resulting conclusions regarding useful diffusion and air-liquid interface behavior observations will be increasingly accurate. Valid conclusions can be made for

inhaled drug behavior when the artificial system is as close to natural physiologic characteristics as possible.

### **1.5 Drug Inhalation, Deposition, and Diffusion**

Understanding the fate of aerosol drugs in the lungs is essential to the therapeutic properties of treatments provided by the drugs. Chemical interaction is an important characteristic to consider, since the pharmacodynamic response is determined by these interactions [Todoroff and Vanbever, 2011]. Drugs that are quickly uptaken by pulmonary macrophages provide rapid response to ailing lungs, while uptake by other cell types may redirect the drugs to another pathway, deeming them ineffective to their desired pathway [Todoroff and Vanbever, 2011]. Drugs must also be small enough to avoid being swept away by cilia in the lung epithelial cells (mucociliary clearance), but large enough to avoid being exhaled. In order to minimize the amount of exhaled particles and dose variability, particles should be greater than 0.5-1  $\mu\text{m}$ . These particles will settle in the central and distal tracts of the lung by gravitational settling [Todoroff and Vanbever, 2011]. Particles less than 1  $\mu\text{m}$  are most likely to be exhaled [El-Gendy et al., 2011]. Ultrafine particles less than 100 nm can reach the alveolar region, where systemic drug absorption occurs, by Brownian motion [Todoroff and Vanbever, 2011]. Particles in the range of 1-3  $\mu\text{m}$  also reach the alveolar region, while particles 3-10  $\mu\text{m}$  deposit in the tracheo-bronchial tree for airway treatment [Todoroff and Vanbever, 2011].

The structure of the lung tissue that interacts with the inhaled particles is largely dependent on the airway generation where the particle deposits. The particle deposition location is based on the aerodynamic diameter of the aerosol particle, and is a function of particle density, particle diameter and particle dynamic shape factor [Todoroff and

Vanbever, 2011]. Drug behavior at the air-liquid interfaces also needs to be evaluated. Proteins, protein aggregation, and particle immersion must also be considered [Todoroff and Vanbever, 2011].

Lung geometry is the last important factor to consider when modeling particle fate with inhalation drugs. Lungs are similar to inverted trees, with a large trunk (the trachea) and branches that are bifurcated into many generations, with the largest generations branching off the trachea and becoming increasingly smaller with thicker lung walls [Gehr et al., 1990]. The thinner, larger generations, where drugs are most likely deposited, have more ideal properties such as larger surface area and thinner lung walls for drug diffusion [Martonen and Katz, 1993, Gehr et al., 1990]. A depiction of lung geometry can be seen in Figure 1.3.

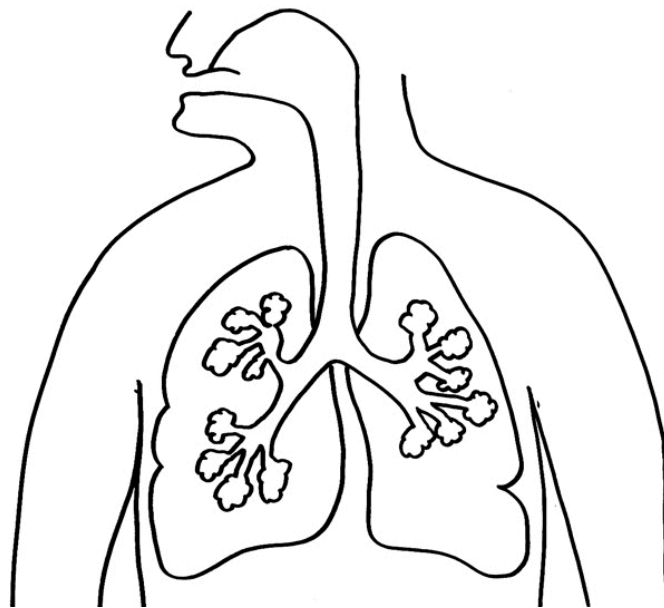


Figure 1.3 Depiction of human lung generations.

## 1.6 Research Objectives

Using the information provided from previous sections, a comprehensive understanding of asthma, treatments of the disease, the geometry of the lung, and mucus and saliva properties has been formed. This study investigates the physicochemical properties of saliva and mucus that impact the ultimate fate of the drug being administered and its bioavailability. Three artificial salivas were made and evaluated for pH, interfacial tension and rheological properties in both the neat and drug-doped forms. It is also important to understand the path of the particulates that exist in these inhalation drugs through the respiratory tracts, deposition patterns, and the ultimate bioavailability of these medications. By using representative drug-doped solutions and an artificial mucus layer, materials and transport parameters can be measured for modeling the behavior of drug particles in the human lung.

Once the evaluation of the data demonstrated how the drugs affect the physical properties of saliva, the diffusivity properties of the drugs were then tested. Two drugs, theophylline and albuterol, were then selected for diffusion experimentation using an artificial mucus. Using Fick's second law of diffusion, the diffusivity coefficients of the drugs through the mucus were determined.

This research is part of a larger project that models the deposition pattern of drug particulates on the surface, and then follows the drug particulates through the mucus layer to the lung surface. The mucus layer compositions are also being investigated. This part of the research focuses on the effects of the drugs on the properties of saliva and pulmonary mucus, as well as the diffusion of the drug particles through the mucus layer.

## 1.7 References

- Asthma Medications: Know your options. 2010. Mayo Clinic. <http://www.mayoclinic.com/health/asthma-medications/AP00008> (accessed September 9, 2011).
- Chan, Hak-Kim. Dry Powder Aerosol Delivery Systems: Current and Future Research. *Journal of Aerosol Medicine*, 2006, 19.1, 21-27.
- Donnelly, Ryan F.; McCarron, Paul A.; Cassidy, Corona M.; Elborn, J. Stuart; Tunney, Michael M. Delivery of photosensitisers and light through mucus: Investigations into the potential use of photodynamic therapy for treatment of *Pseudomonas aeruginosa* cystic fibrosis pulmonary infection. *Journal of Controlled Release*, 2007, 117, 217-226.
- El-Gendy, Nashwa; Pornputtapitak, Warangkana; Berkland, Cory. Nanoparticle agglomerates of fluticasone propionate in combination with albuterol sulfate as dry powder aerosols. *European Journal of Pharmaceutical Sciences*, 2011.
- Gehr, P.; Schurch, S.; Geiser, M, Im Hof, V. Retention and Clearance Mechanisms of Inhaled Particles. *Journal of Aerosol Science*, 1990, 21, S491-S296.
- Hombach, Juliane.; Bernkop-Schnurch, Andreas. Mucoadhesive Drug Delivery Systems. *Drug Delivery, Handbook of Experimental Pharmacology*, 2010, 197, 251-266.
- Juniper, E.F.; Johnston, P.R.; Borkhoff, C.M.; Guyatt, G.H.; Boulet, L.P.; Haukioja, A. Quality of life in asthma clinical trials: comparison of salmeterol and salbutamol. *American Journal of Respiratory Critical Care Medicine*, 1995, 151.1, 66-70.
- Khanvilkar, Kavita; Donovan, Maureen D.; Flanagan, Douglas R. Drug transfer through mucus. *Advanced Drug Delivery Reviews*, 2001, 48, 173-193.
- Larhed, Agneta Wikman; Artursson, Per; Grasja, Johan; Bjork, Erik. Diffusion of Drugs in Native and Purified Gastrointestinal Mucus. *Journal of Pharmaceutical Sciences*, 1997, 86, 660-665.
- Levine, Michael J. Development of Artificial Salivas. *Critical Reviews in Oral Biology and Medicine*, 1993, 4, 279-286.
- Martonen, Ted B.; Katz, Ira M. Deposition Patterns of Aerosolized Drugs Within Human Lungs: Effects of Ventilatory Parameters. *Pharmaceutical Research*, 1993, 10, 871-878

Modi, P. The evolving role of Oralin (Oral Spray Insulin) in the treatment of diabetes using a Novel RapidMist Diabetes Management System. *Modern Biopharmaceuticals; Design, Development and Optimization*, 2005, 4, 1445-1461.

Preetha, A.; Banerjee, R. Comparison of Artificial Saliva Substitutes. *Trends Biomater. Artif. Organs*, 2005, 18, 178-186.

Rossetti, D.; Yakybov, G.E.; Stokes, J.R.; Williamson, A.M.; Fuller, G.G. Interaction of human whole saliva and astringent dietary compounds investigated by interfacial shear rheology. *Food Hydrocolloids*, 2008, 22, 1068-1078.

Schipper, Raymond G.; Silletti, E.; Vingerhoeds, Monique H. Saliva as research material: Biochemical, physicochemical, and practical aspects. *Archives of Oral Biology*, 2007, 52, 1114-1135.

Todoroff, Julie; Vanbever, Rita. Fate of nanomedicines in the lungs. *Current Opinion in Colloid and Interface Science*, 2011, 16, 246-254.

Volsko, Teresa; Reed, Michael D. Drugs Used in the Treatment of Asthma. *Respiratory care clinics of North America*, 2000, 6, 41-55.



CHAPTER II  
CHARACTERIZATION OF THE PHYSICOCHEMICAL PROPERTIES OF NEAT  
AND DRUG-DOPED ARTIFICIAL SALIVA

**2.1 Abstract**

Three artificial saliva solutions, xialine 1, xialine 2, and saliveze, were prepared and their properties compared to natural/physiological saliva. The interfacial tensions of the saliva solutions were evaluated in addition to rheological properties. All three artificial saliva solutions varied minimally (1.62-8.46%) from the interfacial tension values given for natural saliva in the literature [Preetha and Banerjee, 2005; Kasakov, 2009]. The artificial salivas were more viscous than natural saliva at all shear rates evaluated by rheology. Each saliva solution was then doped with four drugs used in the treatment of asthma: albuterol/salbutamol, theophylline, potassium iodide (KI), and Advair<sup>®</sup>. KI, salbutamol and Advair<sup>®</sup> consistently increased the interfacial tension measurements. Albuterol and theophylline gave inconsistent interfacial tension results showing both increased and decreased values. The salbutamol- and Advair<sup>®</sup>-doped salivas consistently demonstrated lower viscosities over the shear rate ranges examined (0.1-100 s<sup>-1</sup>) as compared to the neat salivas. Theophylline had minimal impact on the viscosity of the saliva solutions. At lower shear rates, KI-doped salivas were more viscous than the neat salivas, but varied minimally from the neat solutions at higher shear rates. pH data was also collected for the neat and drug doped saliva solutions. Albuterol and theophylline produced minimal changes in the saliva solutions, as well as producing

both increases and decreases in pH levels. KI and Advair<sup>®</sup> produced consistent increases in pH levels for all three saliva solutions.

## 2.2 Introduction

Drugs can be aerosolized using a propellant as a pulmonary drug delivery mechanism for the treatment of respiratory and systemic illnesses. Inhalation drugs have been researched as treatment options for conditions such as asthma [Chan, 2006; Volsko and Reed, 2000], diabetes [Modi, 2005; Todoroff and Vanbever, 2011], and cystic fibrosis [Donnelly et al., 2007; Khanvilkar et al., 2001], among others. Chemical stability, patient compliance, low cost, and small dosages [Chan, 2006] make inhalation drug delivery systems worth further investigation and development.

With inhalation drugs, the drug particles are typically either dry powder or dissolved in an aqueous solution dispensed as small droplets. Regardless of the medium used to carry the drug to the lung, the drug arrives to the lung with some saliva that gets inhaled with each breath. It is therefore important to consider the properties of saliva when researching and modeling drug interactions with the lung. In addition, understanding the complexity of salivary composition and biological function could lead to the development of new salivary substitutes that can combat a number of oral diseases and disorders. Saliva is multifunctional and contributes to not only general health, but also plays major roles in mouth lubrication [Preetha and Banerjee, 2005; Schipper et al., 2007], the management of oral microbes [Rossetti et al., 2008] and digestion [Preetha and Banerjee, 2005; Schipper et al., 2007]. Additionally, saliva has been recently investigated as a provider of biomarkers for diseases and the detection of systemic illnesses [Schipper et al., 2007].

Saliva is a complex natural fluid secreted by human salivary glands (parotid, submandibular and sublingual glands, and minor salivary glands on the tongue [Schipper et al., 2007]) at about 1.5 liters per day [Juniper et al., 1995]. Saliva is an aqueous non-Newtonian fluid [Juniper et al., 1995] comprised mostly of water (99.5%), proteins (0.3%), and inorganic and trace constituents (0.2%) [Schipper et al., 2007]. The proteins that are found in saliva are mostly glycoproteins [Schipper et al., 2007; Juniper et al., 1995], enzymes, immunoglobulins, antimicrobial peptides [Schipper et al., 2007], and lipids [Juniper et al., 1995]. The inorganic portion of saliva contains the standard electrolytes found in bodily fluid but at different concentrations, which causes saliva to be a hypotonic fluid [Schipper et al., 2007].

Saliva has many functions in the body, and artificial saliva acts as a close replicate for patients who lack enough natural saliva for the body's lubrication, mucoadhesive, and protective needs [Juniper et al., 1995]. The artificial saliva used to model natural saliva for experimental purposes must be as close as possible in a biophysical capacity for the accuracy and validity of any conclusions. Asthmatic patients deal not only with inflamed and constricted airways, but also more viscous saliva [Shimura et al., 1988; Keal, 1971]. Studying the effects of pharmaceutical treatments have on the viscosity and interfacial tension of saliva is crucial to understanding the impact these drugs can have on the physiological properties of saliva.

Since initial investigations into asthma inhalation drugs in the early 1900s [Volsko and Reed, 2000], many subtypes of inhalation treatments have been developed. Currently, inhalation-based asthma treatments range from fast-acting "rescue"  $\beta_2$ -receptor agonists to long-acting  $\beta_2$ -receptor agonists that prevent lung inflammation and control the disease [Ullman and Svedmyr, 1998; Volsko and Reed, 2000]. This study

investigates four drugs (albuterol/salbutamol, theophylline, potassium iodide, and a fluticasone/salmeterol mixture) that are used in the treatment of asthma.

Albuterol (salbutamol) is a fast-acting bronchodilator that can be administered through an inhaler or a nebulizer. It is the most commonly used fast-acting treatment for acute asthmatic symptoms. Albuterol can be applied as either a fast-acting rescue treatment or a long-acting treatment [Chan, 2006, Juniper et al., 1995], and is typically administered in solution with saline. Theophylline is a methylxanthine drug initially used in the 1920s [Hendel and Weinberger, 1983]. It is a bronchodilator and respiratory stimulant that can be used as a fast-acting treatment for acute symptoms or can be administered for long-acting relief as well. Potassium iodide (KI) is an expectorant that works by thinning mucous secretions and reduces chest congestion [Hendel and Weinberger, 1983]. The fourth drug is a 2:1 mixture of fluticasone propionate and salmeterol xinafoate marketed commercially as Advair<sup>®</sup>. Fluticasone is a corticosteroid and is used for anti-inflammatory purposes, and salmeterol, which has also been used by itself as a treatment for asthma, is used to treat the constriction of the airways [GlaxoSmithKline, 2010]. Figure 2.1 shows the chemical structures of all the drugs being investigated. The work presented compares some physicochemical characteristics of three artificial salivas, and examines how the addition of asthma medications affects the saliva properties.

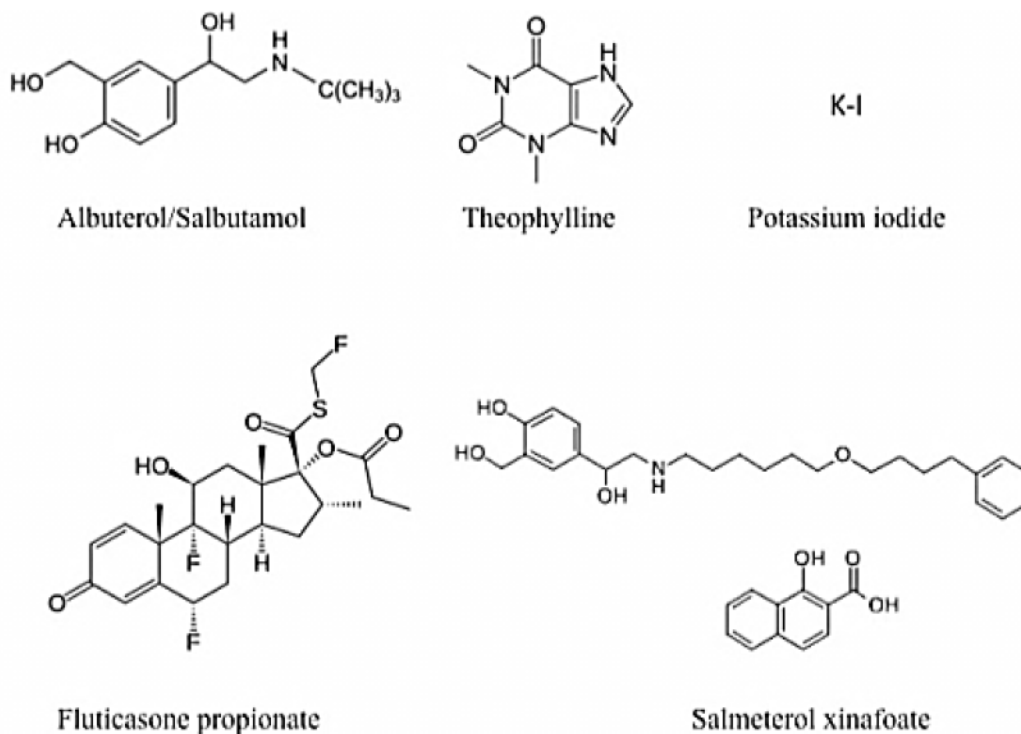


Figure 2.1 Chemical structures of asthma drugs used in this study.

## 2.3 Materials and Methods

### 2.3.1 Drugs

The following drugs were used as the inhalation aerosol treatments in this study: theophylline (>98 %, TCI America, CAS 58-55-9), albuterol sulfate (0.083% albuterol in solution, Nephron Pharmaceutical Corporation, CAS 51022-70-9), salbutamol (MP Biomedicals, CAS 18559-94-9), potassium iodide (99%, Fisher Scientific, CAS 7681-11-0) and fluticasone propionate/salmeterol xinafoate 100mcg/50mcg (commercial name Advair<sup>®</sup>, GlaxoSmithKline).

### 2.3.2 Artificial Saliva Components and Modifying Substances

The chemicals used to make the artificial salivas, as well as the chemicals used to alter the neat solutions, were obtained from Sigma Aldrich (St. Louis, MO, USA), VWR

(West Chester, PA, USA) and Fisher Scientific (Hampton, NH, USA). The artificial saliva components are xanthan gum (90-100%, MP Biomedical, CAS 11138-66-2), calcium chloride (ACS Reagent Grade, 90-100%, MP Biomedical, 10043-52-4), magnesium chloride (MP Biomedical), sodium chloride (<sup>3</sup>99%, Fisher Scientific, CAS 7647-14-5), di-potassium hydrogen orthophosphate (98%, Acros Organics, CAS 7758-11-4), potassium di-hydrogen orthophosphate (<sup>3</sup>99%, Acros Organics, CAS 7778-77-0), D-sorbitol (97%, Acros Organics, CAS 50-70-4), sodium carboxymethylcellulose (99%, TCI America, CAS 9004-32-4), methyl-p-hydroxybenzoate (NF grade, Pfaltz and Bauer, Inc., CAS 99-76-3), sodium fluoride (99%, Alfa Aesar, CAS 7681-49-4), potassium chloride, and food grade spirit of lemon (McCormick brand “pure lemon extract). HPLC grade water (Fisher Scientific, CAS 7732-18-5) was used in the preparation of all aqueous solutions. Some modifications were made to the artificial saliva solutions by adding components, mucin (bovine submaxillary glands Type 1-S, Sigma), and/or phosphatidylserine (PS, >98%, Fluka Biochemika, CAS 51446-62-9).

### **2.3.3 Preparation of Standard Artificial Saliva Solutions**

Three artificial saliva solutions were used for all experimental purposes. Xialine 1 (X1) and xialine 2 (X2) are mainly composed of xanthan gum, while saliveze is based on sodium carboxymethylcellulose and sorbitol. The compositions and concentrations of the components of these saliva solutions were obtained from Preetha and Banerjee [2005] and are shown in Table 2.1.

Table 2.1 Artificial Saliva Compositions [Preetha and Banerjee, 2005].

Artificial Saliva Components	Xialine 1 (g/L)	Xialine 2 (g/L)	Saliveze (g/L)
Xanthan gum	0.92	0.18	-----
Sodium carboxymethylcellulose	-----	-----	10.00
Potassium chloride	1.20	1.20	0.62
Sodium chloride	0.85	0.85	0.87
Magnesium chloride	0.05	0.05	0.06
Calcium chloride	0.13	0.13	0.17
Di-potassium hydrogen orthophosphate	0.13	0.13	0.80
Potassium di-hydrogen orthophosphate	-----	-----	0.30
Sodium fluoride	-----	-----	0.0044
Sorbitol	-----	-----	29.95
Methyl p-hydroxybenzoate	0.35	0.35	1.00
Spirit of lemon	-----	-----	3.785

#### 2.3.4 Preparation of Altered Artificial Saliva Solutions

In an effort to closer resemble natural saliva, components such as mucin (from the bovine submaxillary gland) and phosphatidylserine (PS) were added according to concentrations found in literature. Mucin was added in the concentration 2 mg/mL of saliva solution, a concentration similar to that found in natural saliva [Vissink et al., 1984]. PS was added to the saliva solutions based on the known concentration of the phospholipid phosphatidylethanolamine (PE) present in natural saliva [Levine, 1993]. PS was used instead of PE due to the availability of PS and the higher cost of PE. While the lipid concentration in natural saliva has been found to be 4.4 µg/mL [Preetha and Banerjee, 2005], PS was added to the artificial saliva solutions at 44 µg/mL due to material constraints of other saliva components and to prevent human error with measuring such a small amount of PS.

Other alterations made to the saliva recipes found in the literature included the addition of drugs targeted for the inhalation treatment of bronchial disorders. Albuterol was obtained from the manufacturer pre-mixed at a concentration 0.083% (2.5 mg

albuterol/3 mL isotonic saline). For consistency, this same concentration was used for the addition of theophylline, potassium iodide, salbutamol, and fluticasone propionate/salmeterol to the saliva solutions. It is important to note that salbutamol and albuterol are structurally identical. The reason both materials are included in the study is because the salbutamol was in powder form while albuterol was in solution, and the differences in phase was of interest to examine uniformity between the delivery phases.

### **2.3.5 pH Measurements of Neat and Drug-Doped Artificial Salivas**

pH measurements were collected for the neat saliva solutions (unmodified), as well as the drug doped saliva solutions. The data was collected using an Accumet Basic AB15 pH meter (Fisher Scientific). Prior to data collection, the pH meter was calibrated using buffer solutions of pH 2,4,7,10, and 12. Sample pH values were collected a minimum of three times and averaged.

### **2.3.6 Interfacial Tension Measurements**

Interfacial tension data was collected using a Kruss Easydrop contact angle goniometer with a Teli CCD camera. To contain and dispense the solution droplets, Kendall Monojet tubulin 1 mL syringes with 1.83 mm inner diameter EFD Ultra Dispense needles were used. Kruss' Drop Shape Analysis (DSA) software (version 1.90.0.14) was used to collect and analyze drop images. Pendant drops with 10  $\mu$ L volume were formed at ambient temperature using a dispensing rate of 700  $\mu$ L/min. Images of the pendant drops were then captured and the drop shape evaluated using the DSA software to determine interfacial tension values. For each solution, a minimum of ten interfacial tension points was collected to obtain averages, standard deviation and 95% confidence intervals.



### **2.3.7 Shear Rate and Viscosity Measurements**

Shear rate and viscosity data were collected and analyzed on the saliva solutions using a TA Instruments AR 1500x rheometer with a 60 mm aluminum parallel plate accessory, Rheology Advantage Instrument Control AR software (version V5.7.0), and Rheology Advantage Data Analysis software (version V5.7.0). Step-flow shear data were collected at 37° C (maintained by a Peltier plate) over a shear rate range of 0.1 to 100 s<sup>-1</sup>, with 10 points per decade.

## **2.4 Results**

It is important that these artificial saliva solutions have similar properties to natural saliva so that the effects of drug addition on saliva properties can be understood. Surface coverage and surface wettability are crucial behaviors key to understanding and predicting the path of the particulates in droplet formation and deposition on the lung. The following section discusses the pH, interfacial tension and viscosity of the neat artificial saliva solutions in comparison to natural saliva as well as the interfacial tensions and viscosities of the drug-doped solutions to see the effects of the drug on the viscoelastic properties of saliva.

### **2.4.1 pH of Neat Saliva Solutions and Drug-Doped Saliva Solutions**

pH is one of many factors that affect the diffusion of particles through the pulmonary mucus. It has been reported that an increase in pH produces an increase in diffusion coefficient and a decrease in lag time of the drug particle in the mucus [Shaw et al., 2005]. With this information, the drug-doped saliva solutions, as well as the neat saliva solutions for comparison, were evaluated for pH levels. The effects of drug addition on pH of the neat saliva solutions can be seen in Figure 2.2.

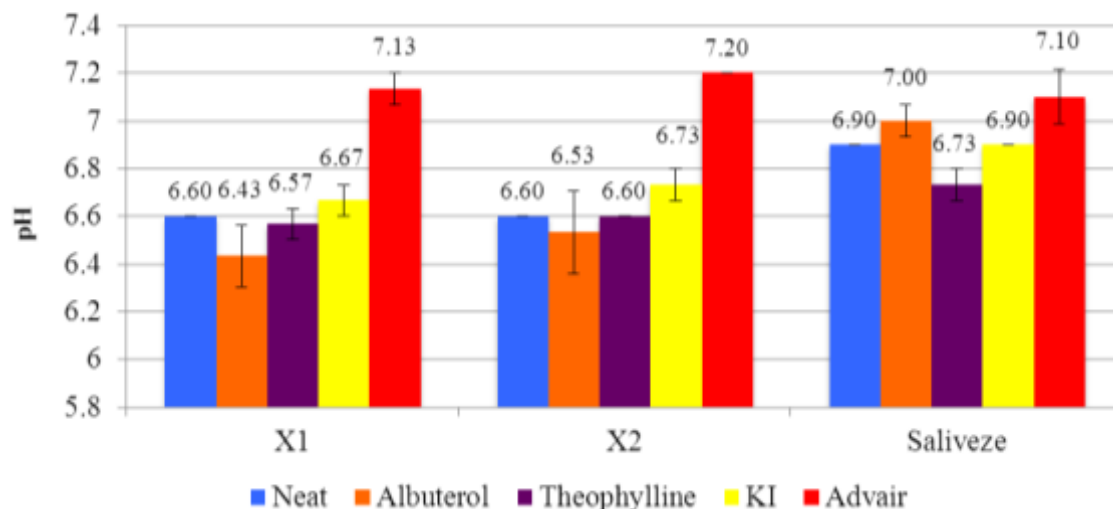


Figure 2.2 pH data for neat and drug-doped artificial saliva solutions.

The addition of drugs produced both increases and decreases in pH of the saliva solutions. Theophylline had the least effect on pH, producing only a 0.46 % decrease in pH for the X1 solution, 0.00% change for X2, and a 2.53% decrease in saliveze. Advair<sup>®</sup> had the greatest effect on pH of the saliva solutions, resulting in 7.43%, 8.33%, and 2.82% increases for X1, X2, and saliveze, respectively. Albuterol produced decreases in pH for X1 (2.64%) and X2 (1.07%), and a slight increase in saliveze (1.43%). KI produced consistent, although slight, increases in pH with all three solutions, resulting in 1.05%, 1.93%, and 0.00% increases for X1, X2, and saliveze, respectively. Of the four drugs, KI and Advair were the only two drugs to produce consistent increases in pH.

The molecular structures of the drugs influenced the effect of the drug addition to the saliva solutions. The molecular structure of Advair<sup>®</sup>, which produced consistent increases in pH in all three solutions, contains several C-F bonds, which are electronegative and the dissociation of the fluorine is the likely cause of the increase in pH. Based on the results of the addition of Advair<sup>®</sup> to the saliva solutions, the fluorine acted as a Lewis acid and accepted a pair of electrons, therefore increasing the pH of the

solution. KI, which also consistently increased the pH of all three solutions, likely dissociated into  $K^+$  and  $I^-$ . The  $I^-$  acted as a Lewis acid, accepting a pair of electrons and increasing the pH of the solution. However, due to the presence of  $K^+$ , which likely acted as a Lewis base and donated a pair of electrons and raising the pH of the solution, the effects of KI on the pH of the solutions are not significant, which is reflected by the very slight solution pH increases. Theophylline also had a minimal effect on pH of the saliva solutions. The structure of theophylline is very stable due to the double ring structure and presence of double bonds. Also, theophylline is a poorly water-soluble molecule [Colinet et al., 2009]. Since theophylline did produce decreases in X1 and saliveze, the dissociation of  $H^+$  from the secondary amine or a breakage of an  $O=C$  double bond were the location(s) of the electron pair donation, therefore acting as a Lewis base and subsequently causing the decrease in pH. Albuterol produced consistent decreases in pH in X1 and X2. Albuterol has several  $-OH$  present that are known Lewis bases, donating a pair of electrons and decreasing the pH of those solutions. Albuterol did produce a slight increase in pH in saliveze, which could be due to the different composition of saliveze compared to X1 and X2. It is important to large range of the 95% confidence interval error bars, which encompass values of neat saliveze and indicate that the slight increase in pH of saliveze with the albuterol addition is not significant.

#### **2.4.2 Interfacial Tension**

The interfacial tension (IFT) of the unmodified saliva solutions was first compared to literature values of similar artificial salivas [Preetha and Banerjee, 2005] for validation purposes. The average xialine 1 (X1) IFT value was 67.59 mN/m, 2.0% higher than the literature value of 66.15 mN/m. xialine 2 (X2) had an average IFT value of 69.31

mN/m, which is 6.8% higher than the 64.89 mN/m literature value. The average saliveze IFT value was 67.05 mN/m, 4.9 % higher than the literature value of 64.17 mN/m. The IFT values for the salivas prepared in this studied varied less than 3.03 % between one another, despite the difference in recipes. They were consistently 2.0 to 6.8 % higher than the literature-reported IFT values for these salivas. This is thought to be due to the differences in collection methods. Pendant drop using a contact angle goniometer was the collection method for this study, while a Langmuir Blodgett instrument was used for the data collection of the literature-reported IFT values [Preetha and Banerjee, 2005].

A comparison of interfacial tension for artificial and natural saliva solutions is presented in Figure 2.3. The artificial salivas varied only minimally from interfacial tensions of natural saliva [Preetha and Banerjee, 2005; Kasakov, 2009]. The IFTs of the artificial salivas varied 1.62-4.57% from natural saliva A [Preetha and Banerjee, 2005] and 5.63-8.46% from natural saliva B [Kasakov, 2009]. The IFT data support the use of these solutions as valid model substitutes for natural saliva.

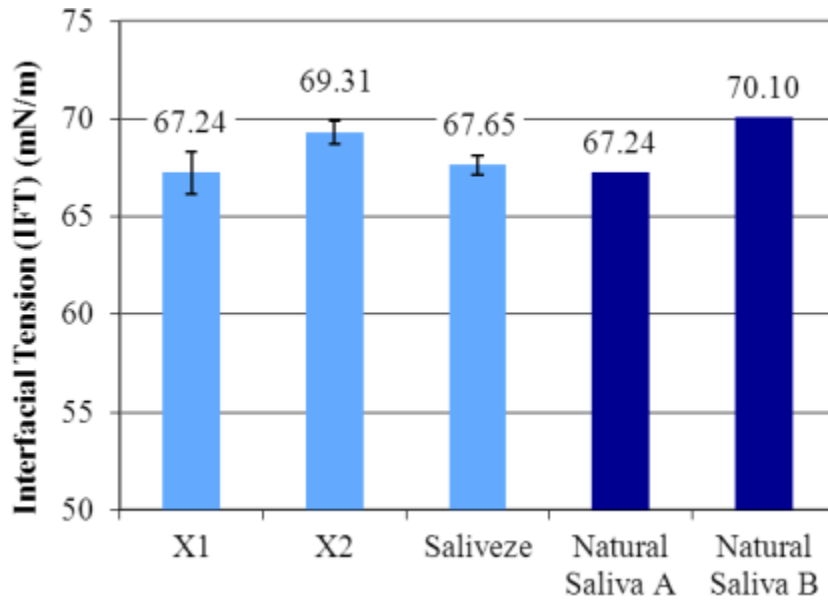


Figure 2.3 Average interfacial tension values for three artificial salivas (X1, X2, and Saliveze) and natural saliva [A: Preetha and Banerjee, 2005; B: Kasakov, 2009]. Error bars represent 95% confidence intervals.

In an effort to make the saliva solutions closer resemble the properties of natural saliva, two types of additives found in natural saliva were added—either separately or in combination—at concentrations found in natural saliva: phosphatidylserine (PS), a phospholipid representative of those found in natural saliva; and mucin, a glycoprotein [Preetha and Banerjee, 2005; Vissink et al., 1984]. PS was added at a concentration of 44  $\mu\text{g}/100\text{ mL}$  [Preetha and Banerjee, 2005] and mucin was added at a concentration of 2% w/v [Vissink et al., 1984]. Interfacial tension data for these modified artificial saliva solutions can be seen in Figure 2.4.

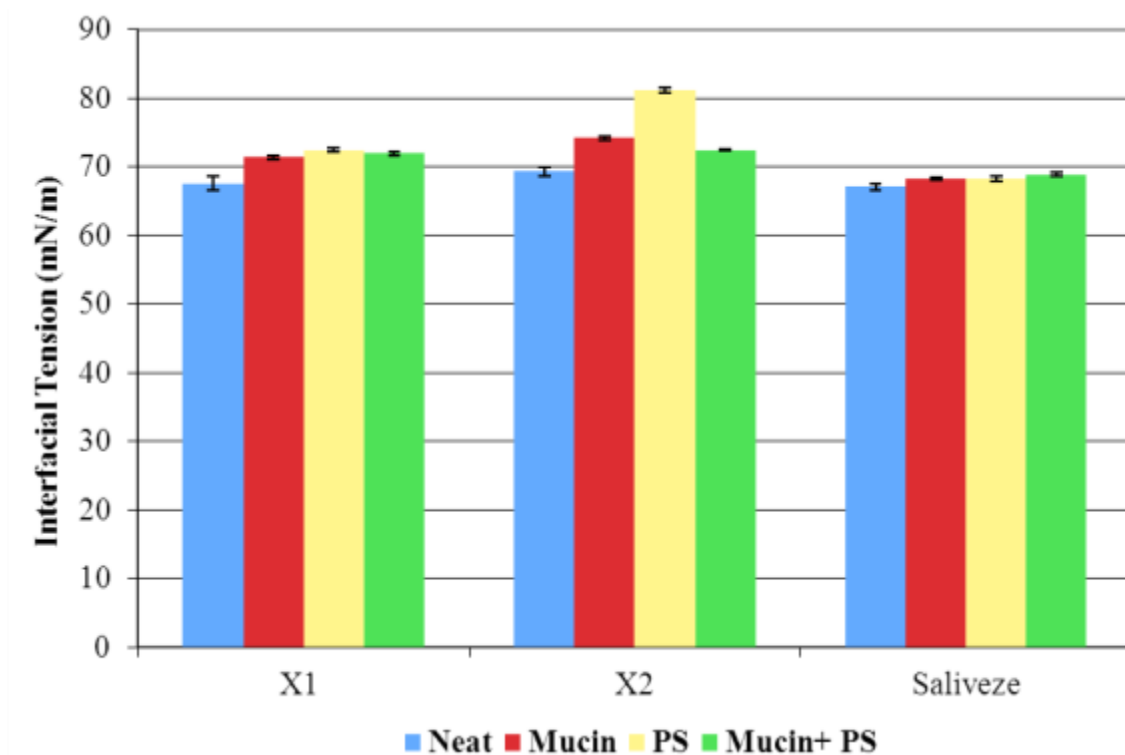


Figure 2.4 Comparison of IFT for artificial saliva solutions with and without the addition of mucus and/or phosphatidylserine (PS), compounds representative of those found in natural saliva.

Preetha and Banerjee (2005) found that the addition of a phospholipid (phosphatidylethanolamine, PE) and mucin caused an increase in IFT in all three of the saliva solutions (X1, X2 and saliveze). Although PS was used in our formulations instead of PE, the addition of mucin and/or PS to the saliva solutions in this study, X1, X2 and saliveze, increased the IFT (Figure 2.3). For X1, the addition of mucin, PS, and mucin+PS resulted 5.61%, 6.64%, and 7.22% increases in IFT, respectively. For X2, which has an identical composition to X1 with the exception of a less amount of xanthan gum, the addition of mucin, PS, and mucin+PS resulted in 6.50%, 16.90%, and 4.43% increases in interfacial tension values, respectively. Lastly, the addition of mucin, PS, and mucin + PS to saliveze resulted in 1.70%, 1.85%, and 2.75% increases in interfacial tension values, respectively. Due to the significant variations in the interfacial tension

property within the artificial salivas (large range of variation from 1.70-16.90%), any further experiments were conducted using only neat saliva solutions without PS or mucin.

IFT was then measured for the three saliva solutions, X1, X2, and saliveze, with and without the addition of the four bronchial drugs (albuterol/salbutamol, theophylline [theo], potassium iodide [KI], and Advair<sup>®</sup>). IFT data for these neat and doped saliva solutions are shown in Figures 2.5-2.7. For these figures, the blue dashed line represents the average IFT for the corresponding neat saliva solution.

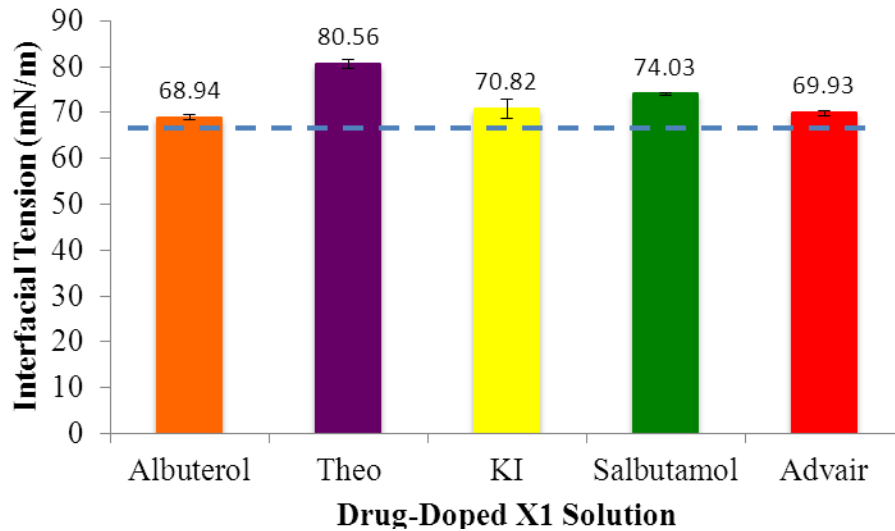


Figure 2.5 Interfacial tension of drug-doped X1 saliva solution. IFT of neat X1 (67.24 mN/m) indicated by blue dashed line.

Figure 2.5 contains the IFT data for X1 saliva solution containing 0.083% w/v of four asthma drugs showing that drug addition resulted in elevated IFT values for X1. The IFT increase ranged from 2.05% (albuterol) to 19.26% (theophylline). The IFT values of albuterol and salbutamol varied a higher than expected amount. Despite the shared structure and equivalent concentration levels in the saliva solutions, the form of the drug (solution versus powder) seems to affect the surface tension in X1.

The other two saliva solutions did not show the same general trend for all of the drugs. KI, salbutamol, and Advair<sup>®</sup> increased the IFT for X2 (Figure 2.6), and these same three—plus albuterol—resulted in increased IFT for saliveze (Figure 2.7). For X2, albuterol caused a 10.17% decrease and theophylline produced a 6.78% decrease in average IFT. KI, salbutamol, and Advair<sup>®</sup> raised the IFT of X1 from 0.51% (KI) to 8.15% (salbutamol). Of the four drugs tested, saliveze showed a decreased IFT (1.2%) only with the addition of theophylline. The other four drugs caused increased IFT ranging from 2.0 % (Advair<sup>®</sup>) to 5.9 % (salbutamol).

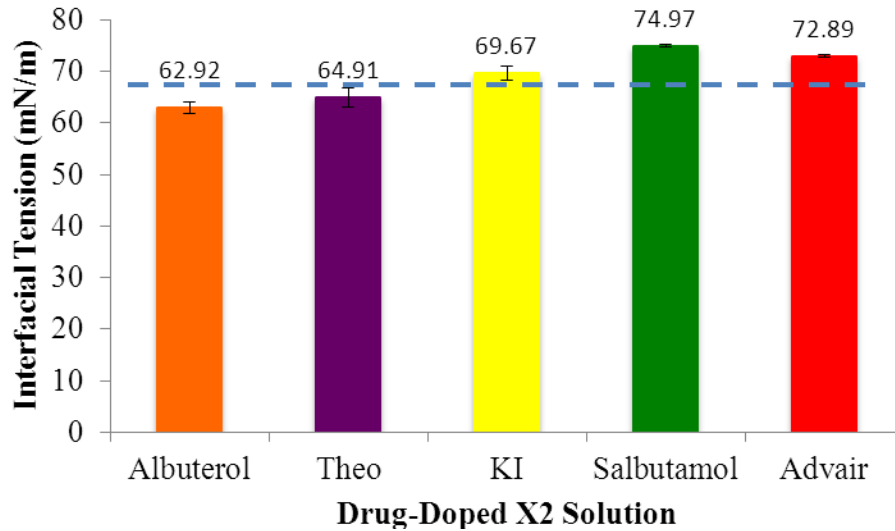


Figure 2.6 Interfacial tension of drug-doped X2 saliva solution. IFT of neat X2 (69.31 mN/m) indicated by blue dashed line.

It is uncertain the exact reasons for the inconsistency regarding the impact of drug addition on the IFT of the artificial saliva solutions. It was expected that the addition of a given drug would result in similar IFT deviation trends, particularly with X1 and X2 since the two solutions have only small differences in composition. Regardless of the lack of general trends, drug addition to the artificial saliva solutions, even at a low



concentration (0.083% w/v), resulted in marked deviations in IFT, a key parameter in aerosol droplet formation and deposition in the lung. To improve deposition performance, the addition of these drugs would ideally result in decreased IFT. Surface tension affects wettability of the fluid, which impact surface coverage and therefore diffusion and ultimate fate of the fluid and the particulates in the fluid. Drug additions resulting in lower surface tensions increase wettability and therefore increase surface coverage. A larger surface coverage would allow a larger amount of drug arriving on the lung surface to diffuse through the pulmonary mucus layer and into the tissue for the fastest possible drug efficiency.

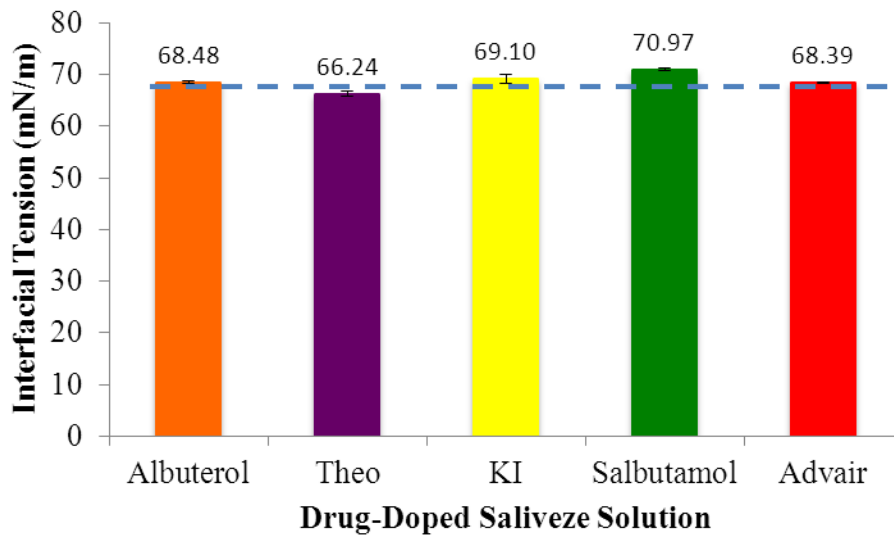


Figure 2.7 Interfacial tension of drug-doped saliveze saliva solution. IFT of neat saliveze (IFT 67.05 mN/m) indicated by blue dashed line.

The range of changes in IFT with the addition of drugs can be better explained with understanding of the hydrophobicity of the drugs. An increase in IFT indicates the drop of the solution (referring to the drop suspended from the needle in pendant drop goniometry) is becoming more hydrophilic. Theophylline is a poorly water-soluble drug

[Colinet et al., 2009], so the increase in IFT of the theophylline-doped X1 solution can be justified with that information. The slight decreases in IFT of theophylline-doped X2 and saliveze may be due to theophylline not dissolving fully in that solution. The other drugs produced consistent IFT increases in all other solutions, with the exception of the decrease in albuterol-doped X2. Advair<sup>®</sup> contains several CF bonds, which are hydrophobic and the likely cause for the increase in IFT of the saliva solutions. Albuterol/salbutamol is water soluble, and it was expected that both solutes would produce decreases in IFT. KI produced consistent increases, indicating the solubility in saliva was minimal. The solubility of KI is affected by solvent temperature in pure water. Since the saliva solutions are very concentrated with materials other than water, KI had limited solubility.

It is also important to refer to the error bars as well as the values of the average IFT values for each drug addition for each solution. The changes in IFT with the addition of drugs are very slight at the low drug concentration. Analysis of a stronger concentration of drug on the changes in IFT with the drug addition would be required to fully determine the effect the drugs have on IFT of saliva.

### **2.4.3 Rheology**

The viscoelastic properties of the artificial saliva solutions were also examined using rheology. Viscosity data was collected as a function of shear rate to identify any shear thinning or shear thickening behaviors. All samples were run in triplicate. Figure 2.8 displays shear rate versus viscosity data for the neat (unmodified) saliva solutions and natural saliva [Preetha and Banerjee, 2005]. All three of the artificial solutions were found to be more viscous than natural saliva over the shear rate range tested. This higher

viscosity may be due to the relative low number of components in the artificial solutions (13) versus natural saliva and/or it could be a result of the limited data for natural saliva viscosity found in the literature. Another issue may lie with the variation in the measured values for natural saliva, which is not unexpected considering the inherent variation in samples collected from human donors [Preetha and Banerjee, 2005; Vissink, et al. 1984].

All three neat artificial saliva solutions were found to be non-Newtonian and exhibited shear thinning behavior, similar to the viscoelastic behavior observed for natural saliva. Visually saliveze appeared to be much thicker and viscous than either xialine solution. The rheology data collected on these samples confirms this observation. Xialine 1 and xialine 2 are both less viscous than saliveze over the entire shear rate range tested (Fig. 2.8). Due to the only slight differences in composition between xialine 1 and xialine 2, it was expected that the two solutions would not exhibit significantly different rheological properties. However, the one difference in composition between xialine 1 and xialine 2, the concentration of xanthan gum, is the likely reason for this variation. Xanthan gum is a well-known and commonly used thickening agent. A slightly more viscous xialine 1 would result in a higher viscosity at lower shear rates, but this slight variation in composition is less notable at higher shear rates.

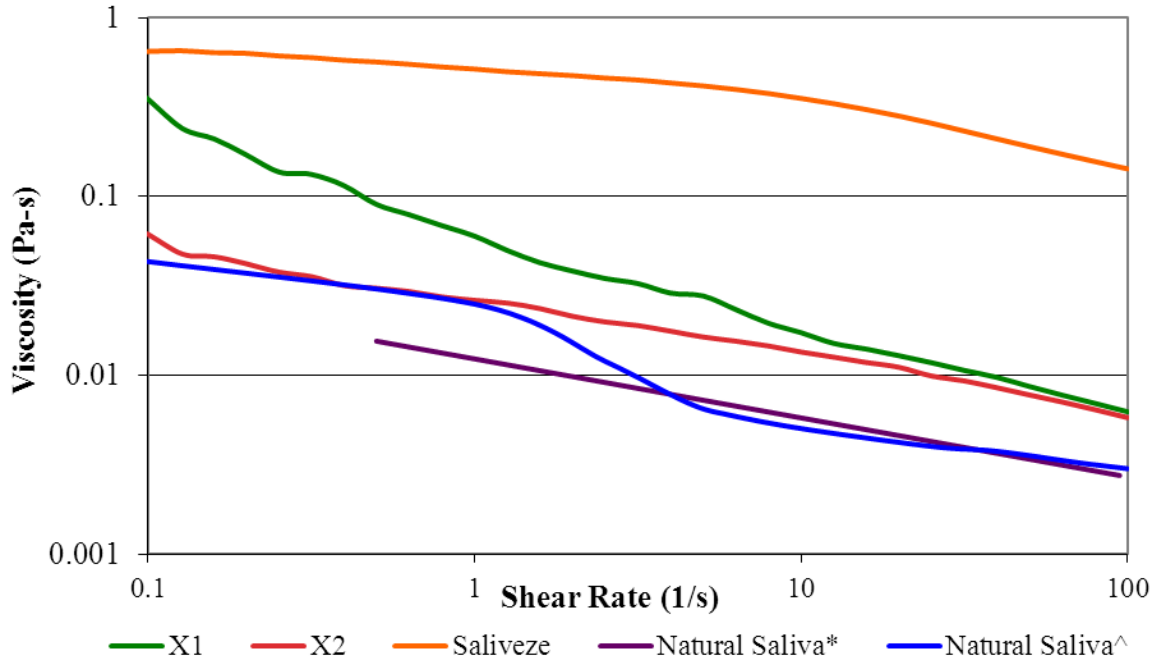


Figure 2.8 Viscosity versus shear rate for neat artificial saliva solutions and natural saliva [\*Preetha and Banerjee, 2005, ^Vissink et al., 1984].

Rheological characterization was also performed on the saliva solutions doped with Advair<sup>®</sup>, KI, salbutamol, or theophylline. Due to material constraints, rheology data was not collected for albuterol-doped solutions. Figures 2.9, 2.10, and 2.11 display the rheological data for drug doped xialine 1, xialine 2, and saliveze, respectively.

Figure 2.9 shows a plot of shear rate versus viscosity for neat xialine 1 and its drug-doped derivatives. The solutions tested all exhibited shear thinning, non-Newtonian viscoelastic behavior. All five solutions show decreased viscosity as shear rate increased and appeared to approach common viscosity levels at the highest shear rates tested (100 s<sup>-1</sup>). Neat xialine 1 had the highest viscosity values at low shear rates.

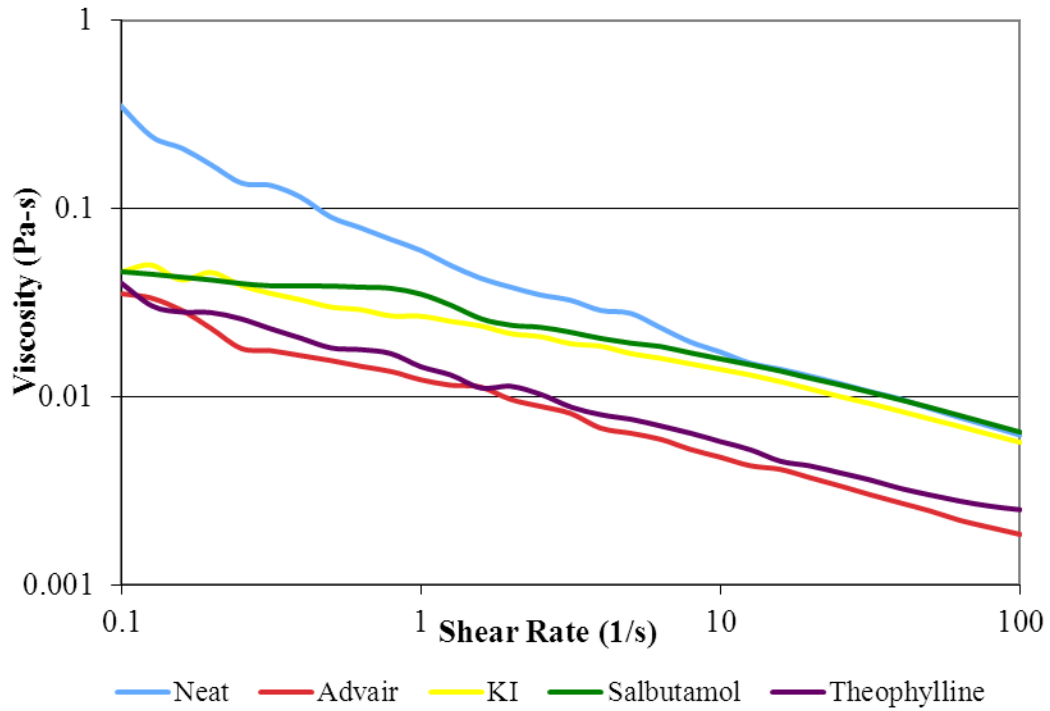


Figure 2.9 Plot of viscosity versus shear rate for comparison of neat xialine 1 to drug-doped xialine 1.

A plot of rheological data for neat and drug-doped xialine 2 is shown in Figure 2.10. Neat and drug-doped xialine 2 solutions exhibited non-Newtonian, shear thinning behavior. The KI-doped solution had the highest viscosity at the lower shear rates, even higher than the neat solution.

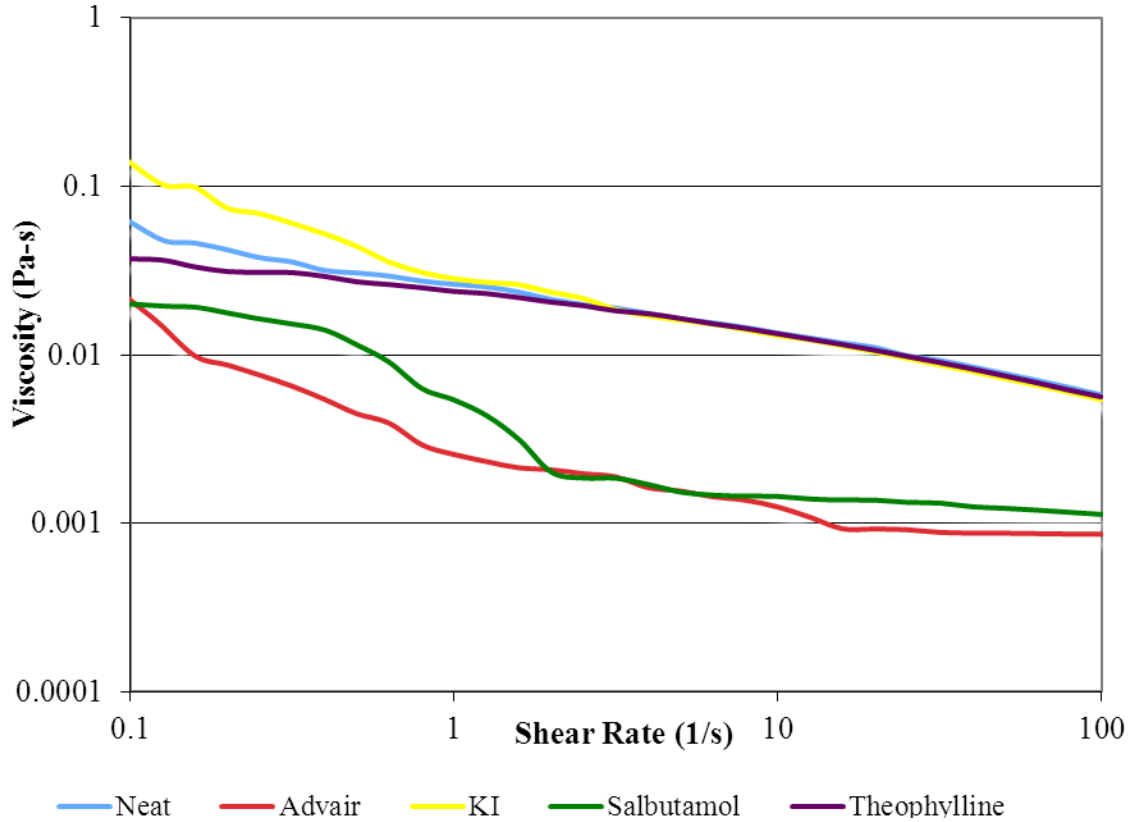


Figure 2.10 Plot of viscosity versus shear rate for comparison of neat xialine 2 to drug-doped xialine 2.

Each of the saliveze solutions, neat and doped (Fig. 2.11), showed non-Newtonian, shear thinning behavior, similar to xialine 1, xialine 2 and natural saliva. Saliveze doped with KI was the only solution to show higher viscosities than the neat solution over the entire shear rate range tested. Theophylline-doped saliveze also had a higher viscosity than the neat saliveze at lower shear rates, but then its viscosity decreased slightly below that of the neat saliveze as the shear rate was increased. Salbutamol and Advair<sup>®</sup> doped solutions followed the same trends observed for the xialine solutions and were less viscous than the neat solution over all the shear rate range tested.

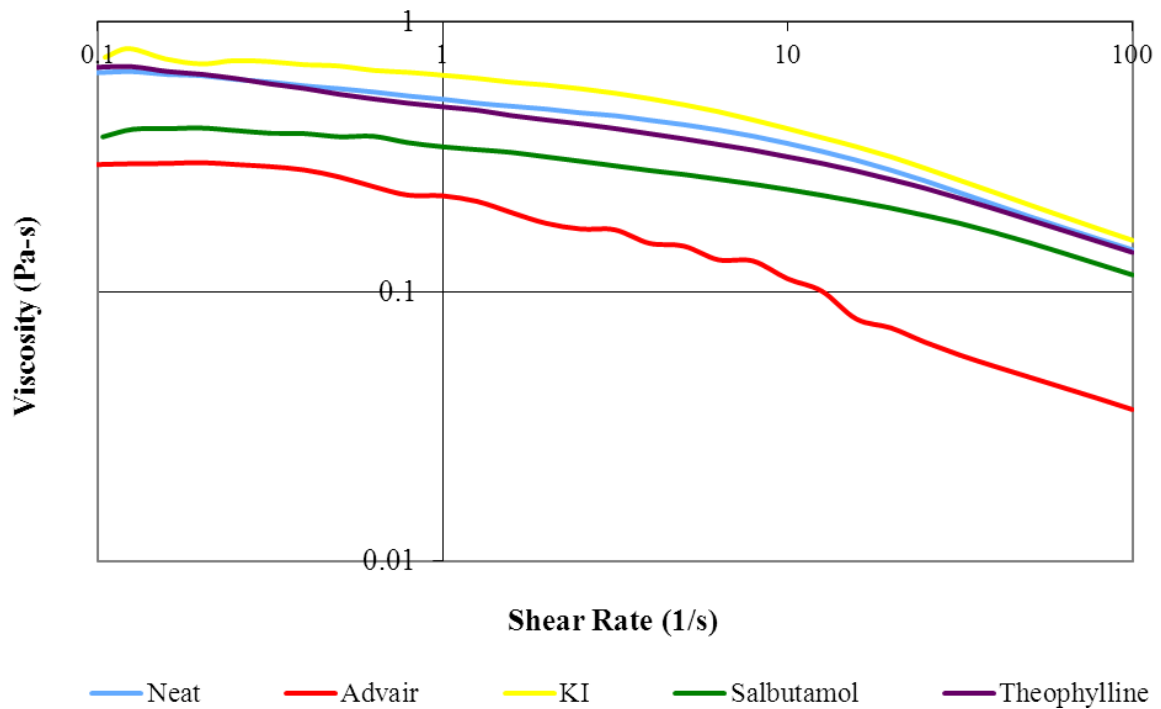


Figure 2.11 Plot of viscosity versus shear rate comparing neat (unmodified) saliveze to drug doped saliveze.

## 2.5 Conclusions

The neat artificial saliva solutions generated as part of this study varied minimally from literature interfacial tension values for natural saliva, thus supporting the use of these artificial solutions as valid substitutes for natural saliva. The artificial salivas were more viscous than natural saliva at all shear rates; this could be due to the extreme range of possible properties of natural saliva, which vary between specimens and are affected by factors such as age of the patient, diet of the patient, general health, and natural composition that are never identical between specimens.

Drug addition to the artificial saliva solutions at a relatively low concentration resulted in measurable deviations in the interfacial tension, a key parameter in aerosol droplet formation and deposition in the lung. KI, salbutamol, and Advair<sup>®</sup> consistently produced increases in the average interfacial tension measurements that were collected.

Albuterol and theophylline were inconsistent with both increases and decreases in average interfacial tension measurements observed depending on the specific drug. Ideal results would have shown consistent decreases in interfacial tension with the drug additions. Lower surface tensions would result in increased wettability and subsequently increased surface coverage. A larger surface coverage would allow a larger amount of drug arriving on the lung surface to permeate through the mucus layer present on the lung and into the tissue for the quickest possible effectiveness of the drug. The impact of drug addition on droplet formation, deposition, and wettability are important factors in predicting the behavior of aerosol drugs on the lung surface.

Salbutamol and Advair<sup>®</sup> consistently showed lower viscosities over all shear rate ranges when compared to the neat saliva for all saliva types. Since salbutamol and albuterol are structurally identical, it can be reasonably assumed that albuterol would have produced similar data to salbutamol and also result in lower viscosity trends. Theophylline had minimal effect on the viscosity of the saliva solutions, and has little to no variations from the neat solutions. KI appeared to have higher viscosities at lower shear rates than the neat solutions, but varied minimally from the neat solutions at higher shear rates. Decreases in viscosity with the addition of drugs were the desired result. Less viscous fluids have increased surface wettability and coverage and therefore would allow a larger area of drug-doped saliva to deposit on the lung with a greater amount of drug available to treat the applicable condition.

Additionally, pH data was collected for the neat and drug doped saliva solutions. Albuterol and theophylline produced minimal changes in the saliva solutions, as well as producing both increases and decreases in pH levels. KI and Advair<sup>®</sup> produced consistent increases in pH levels for all three saliva solutions.



## 2.6 References

Chan, Hak-Kim. Dry Powder Aerosol Delivery Systems: Current and Future Research. *Journal of Aerosol Medicine*, 2006, 19(1), 21-27.

Colinet, I.; Dulong, V.; Mocanu, G.; Picton, L.; Le Cerf, D. New amphiphilic and pH-sensitive hydrogel for controlled release of a poorly water-soluble drug. *European Journal of Pharmaceutics and Biopharmaceutics*, 2009, 73, 345-350.

Donnelly, Ryan F.; McCarron, Paul A.; Cassidy, Corona M.; Elborn, J. Stuart; Tunney, Michael M. Delivery of photosensitisers and light through mucus: Investigations into the potential use of photodynamic therapy for treatment of *Pseudomonas aeruginosa* cystic fibrosis pulmonary infection. *Journal of Controlled Release*, 2007, 117, 217-226.

GlaxoSmithKline. Advair<sup>®</sup>, Highlights of Prescribing Information. [http://us.gsk.com/products/assets/us\\_advair.pdf](http://us.gsk.com/products/assets/us_advair.pdf) (accessed June 19, 2010).

Hendel, L.; Weinberger, M. Theophylline: A State of the Art Review. *Pharmacotherapy*, 1983, 3(1), 2-44.

Juniper, E.F.; Johnston, P.R.; Borkhoff, C.M.; Guyatt, G.H.; Boulet, L.P.; Haukioja, A. Quality of life in asthma clinical trials: comparison of salmeterol and salbutamol. *American Journal of Critical Care Medicine*, 1995, 151(1), 66-70.

Kazakov, V.N.; Udod, A.A.; Zinkovvch, Iryna, I.; Fainerman, V.B.; Miller, R. Dynamic surface tension of saliva: General relationships and application in medical diagnostics. *Colloids and Surfaces B: Biointerfaces*, 2009, 74, 457-461

Keal, E.E. Biochemistry and rheology of sputum in asthma. *Postgraduate Medical Journal*, 1971, 47, 171-177.

Khanvilkar, Kavita; Donovan, Maureen D.; Flanagan, Douglas R. Drug transfer through mucus. *Advanced Drug Delivery Reviews*, 2001, 48, 173-193.

Levine, Michael J. Development of Artificial Salivas. *Critical Reviews in Oral Biology and Medicine*, 1993, 4, 279-286.

Modi, P. "The evolving role of Oralin (Oral Spray Insulin) in the treatment of diabetes using a Novel RapidMist Diabetes Management System" *Modern biopharmaceutics; design, development and optimization*. 2005, 4, 1445-1461.

Preetha, A.; Banerjee, R. Comparison of Artificial Saliva Substitutes. *Trends Biomater. Artif. Organs*, 2005, 18(2), 178-186.

Modi, P. "The evolving role of Oralin (Oral Spray Insulin) in the treatment of diabetes using a Novel RapidMist Diabetes Management System" *Modern biopharmaceutics; design, development and optimization*. 2005, 4, 1445-1461.

Rossetti, D.; Yakybov, G.E.; Stokes, J.R.; Williamson, A.M.; Fuller, G.G. Interaction of human whole saliva and astringent dietary compounds investigated by interfacial shear rheology. *Food Hydrocolloids*, 2008, 22, 1068-1078.

Schipper, Raymond G.; Silletti, E.; Vingerhoeds, Monique H. Saliva as research material: Biochemical, physiochemical, and practical aspects. *Archives of Oral Biology*, 2007, 52, 1114-1135.

Shaw, Lance R.; Irwin, William J.; Grattan, Tim J.; Conway, Barbara R. The influence of excipients on the diffusion of ibuprofen and paracetamol in gastric mucus. *International Journal of Pharmaceutics*, 2005, 290, 145-154.

Shimura M.D., Sanae; Sasaki, M.D., Tsukasa; Sasaki, M.D., F.C.C.P., Hidetada; Takishima, M.D., F.C.C.P., Tamatsu. Chemical Properties of Bronchorrhea Sputum in Bronchial Asthma. *Chest*, 1988, 94(6), 1211-1215.

Ullman, A.; Svedmyr, N. Salmeterol, a new long acting inhaled  $\beta_2$  adrenoceptor agonist: comparison with salbutamol in adult asthmatic patients. *Thorax*, 1988, 43, 674-678.

Vissink, A.; Waterman, H.A.; 's-Gravenmade, E.J.; Panders, A.K.; Vermey, A. Rheological properties of saliva substitutes containing mucin, carboxymethylcellulose, or polyethylenoxide. *Journal of Oral Pathology*, 1984, 13, 22-28.

Volsko, Teresa; Reed, Michael D., Pharm D.; Drugs used in the treatment of asthma: A review of clinical pharmacology and aerosol drug delivery. *Respiratory Care Clinics of North America*, 2000, 6(1).

## CHAPTER III

### DIFFUSION OF THEOPHYLLINE AND ALBUTEROL THROUGH ARTIFICIAL MUCUS

#### 3.1 Abstract

Two drugs used in the treatment of asthma, theophylline and albuterol, were diffused through an artificial mucus layer for the purpose of evaluating their diffusion coefficients. To monitor the diffusion process, one side of the mucus layer was placed in contact with the drug-doped isopropanol solution and the other side of the layer was in contact with a zinc selenide crystal to allow for time-resolved attenuated total reflectance Fourier transform infrared spectroscopy (ATR-FTIR) measurements. Spectra were collected at constant time intervals and monitored for quantitative changes in spectral peaks corresponding to the functional groups of the drugs. Analysis of the data resulted in diffusivity coefficients of  $5.5\text{-}7.0 \times 10^{-6} \text{ cm}^2/\text{s}$  for theophylline (as dissolved in isopropanol [IPA]) through artificial mucus and  $4.9\text{-}9.6 \times 10^{-6} \text{ cm}^2/\text{s}$  for albuterol (dissolved in IPA) through artificial mucus.

#### 3.2 Introduction

Significant advancements in delivery method and drug efficiency have been made in the treatment of respiratory illnesses such as asthma. Treatments are most commonly aerosol inhalation pharmaceuticals that range from fast-acting rescue drugs to long-term medications that prevent lung inflammation and allow for control of the disease [Volsko and Reed, 2000]. Inhalation drugs have many characteristics that make them worth

further investigation and development, including good patient compliance, chemical stability, small dosages, and bypassing the digestive system [Chan, 2006].

It is important to understand the path of particulates—including inhalation drugs—through the respiratory tract, deposition patterns, and the ultimate bioavailability of these medications. Upon inhalation, drug particles travel through the bronchiole lung generations and ultimately land on the mucus layer that coats the alveolar pulmonary membrane. Inhaled drugs must then diffuse through the mucus layer in order to reach the lung surface and treat the inflammation.

The complexity of the mucus is a major contributing factor to the path of the drug particulates and the composition of the pulmonary mucus layer. Mucus is hydrophobic [Khanvilkar et al., 2001], exists in two layers, and is arranged in crosslinked and entangled mucin fiber networks [Lai et al., 2009]. The gel, which is the upper more viscous phase, is composed of 95% water, 2% mucus and 3% salts, proteins and lipids [Todoroff and Vanbever, 2011; Khanvilkar et al., 2001]. The sol is the bottom, less viscous layer that sits atop the pulmonary epithelial cells and beating cilia. The primary function of pulmonary mucus is to protect the lung surface and trap foreign matter that enters the lungs. Figure 3.1 illustrates the structure of the gel-sol mucus layer on top of the pulmonary epithelial cells and beating cilia.

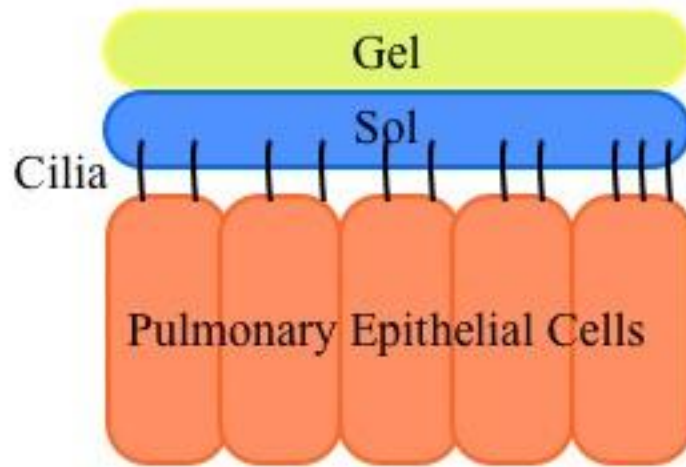


Figure 3.1 Illustration of gel-sol mucus structure above the pulmonary epithelial cells with beating cilia penetrating the sol layer.

The trapped particles are swept away by beating cilia or exhalation unless they are able to transport through the mucus faster than the effective velocity transport of the upper layer. The gel layer of the mucus is replenished approximately every twenty minutes due to the mucus flow rate of about 5 mm per minute [Lai et al., 2009]. This rapid transformation is responsible for the effective clearance of any trapped particles. The sol layer is renewed much slower. Aside from mucociliary clearance, particles may also become trapped in the dense fiber mesh of the mucus layer formed by the mucin macromolecules [Khanvilkar et al., 2001], further obstructing the permeability of the particle [Lai et al., 2009]. In order for particles to diffuse through the complex mucus network, the drugs must penetrate the mucus layer faster than the rate of mucus renewal and clearance [Lai et al., 2009].

Aerosol drugs are designed to retain medicinal properties while diffusing through the mucus. It is possible to design particles to overcome the obstruction of the mucus layer. Mucus-inert polymers or hydrophilic coatings can be used to increase the rate of

particle diffusion as well as further customize the drug release and improve drug effectiveness [Lai et al., 2009]. Another technique being researched is mucoadhesion, where particles are coated with a polymeric material designed to cling to the mucus layer, slowing the particle transfer time and improving drug absorption [Lai et al., 2009].

One of the most influential characteristics of a material to diffuse is size.

Nanoparticles (>100 nm) can remain in the lungs for weeks due to their small size, while larger particles of ideal aerodynamic diameter for treating airways (1-5  $\mu\text{m}$ ) [El-Gendy et al., 2011] are cleared from the lung within 24 h [Todoroff and Vanbever, 2011]. Particles that are small enough to be diffused are cleared through the mucus layer and into the pulmonary membrane, eventually becoming systemic. Larger particles are swept away by cilia or exhaled. By using representative drug-doped solutions and an artificial mucus layer, materials and transport parameters can be measured for modeling the behavior of drug particles in the human lung.

Drug diffusion is also affected by other drug characteristics such as surface charge [Khanvilkar et al., 2001, Larhed et al., 1997], molecular weight, and lipophilicity [Larhed et al., 1997]. It has also been found that hydrophobic particles have lower permeabilities due to the hydrophobic nature of the mucus [Khanvilkar et al., 2001; Norris and Sinko, 1997]. Strong lipophilic particles have lower diffusion coefficients than less lipophilic particles [Larhed et al., 1997]. Molecular weights have been investigated for their influence on particle diffusion. Larhed et al. found that drugs with higher molecular weights had lower diffusion coefficients than the particles with lower molecular weights [Larhed et al., 1997], and this inverse relationship between molecular weight and diffusion coefficient has been regularly reported [Khanvilkar et al., 2001]. Additionally,

particle charge has been found to influence drug diffusion since mucus components are negatively charged. Khanvilkar et al. reported that positively charged low-molecular weight drugs bind to the mucus electrostatically [Khanvilkar et al., 2001]. It has also been reported that particles with a negative charge is not affected by the mucus barrier [Khanvilkar et al., 2001; Norris and Sinko, 1997]. It has also been reported that hydrogen bonding and hydrophobic interactions bind polar and non-polar drugs to mucus [Khanvilkar et al., 2001]. Additionally, pH was found to influence the diffusion of drugs across the membrane. An increase in pH produced an increase in diffusion coefficient and a decrease in lag time [Shaw et al., 2005].

### **3.2.1 Mucus Diffusion using ATR-FTIR**

Typically, more conventional methods of transport experiments such as permeation cells or dynamic gravimetric sorption have been used to measure diffusion [Hallinan et al., 2007; Hallinan et al., 2010]. However, ATR-FTIR as a method for measuring diffusion has been used with increasing frequency over the past two decades [Elabd et al., 2003]. ATR-FTIR allows for time-resolved analysis of diffusion systems on a molecular level during the diffusion process, as well as quantification of molecular interactions between the diffusants and diffusing medium through shifts in IR spectra [Hallinan et al., 2007; Hallinan et al., 2010]. Several systems have obtained successful results using time-solved ATR-FTIR spectra for measuring diffusion. Hallinan et al. measured diffusion of methanol and water in nafion using the ATR-FTIR method, as well as relating the spectral information to concentration and subsequently Fick's second law, similar to the method used in this study. The results of the methanol and water diffusion in nafion matched results determined from a permeation cell, validating this technique for

that system [Hallinan et al., 2007; Hallinan et al., 2010]. Additionally, systems such as water in polymers like poly(vinyl chloride) or poly(ethylene terephthalate) [Elabd et al., 2003] and even biological systems such as the permeation of acetonitrile and p-cyanophenol in polyethylene glycol through silastic membranes representative of skin [Watkinson et al., 1994] have been successfully evaluated using the ATR-FTIR method of data collection and Fickian diffusion model. Elabd et al. highlights several more systems for which this technique has worked, primarily diffusants/solutes through polymers [Elabd et al., 2003]. Each of the systems he mentions have many references, signifying the abundant amounts of data to validate this method in over fifty diffusing systems [Elabd et al., 2003].

Despite the success of using ATR-FTIR as a method for characterizing diffusion coefficients, this technique has scarcely been used for analyzing mucosal diffusion systems. Larhed et al. determined the diffusion coefficients of lipophilic drugs mannitol, metoprolol, propranolol, hydrocortisone, and testosterone through native pig intestinal mucus, but did so using a radiolabeled drug tracer technique. Plastic syringes (1 mL) with the tips cut off were used as diffusion chambers. The syringes were filled with a mucus gel solution stabilized with glass bead packing, and the radiolabeled drug solution is added over the gel and allowed to diffuse through the gel [Khanvilkar et al., 2001; Larhed et al., 1998; Larhed et al., 1997]. The gel is then pushed out of the tube and cut into pieces, and the radioactivity in each piece of gel is determined. Using the syringe tube geometry, weighted least square fits of normalized theoretically determined radioactivity values and normalized experimental radioactivity values, the diffusion coefficients are obtained [Khanvilkar et al., 2001; Larhed et al., 1998; Larhed et al., 1997]. Owen et al. used a UV spectrophotometric technique where two quartz capillary cells, one loaded



with Nonoxynol-9-doped alginate delivery gel and the other with bovine cervical mucus, are brought in contact with one another and a quantifiable concentration profile is achieved [Khanvilkar et al., 2001; Owen et al.,1999]. The cell holder is then scanned using the sample transport drive of a UV spectrophotometer [Khanvilkar et al., 2001; Owen et al., 1999].

Despite the developments that have been made in the efficiency of inhalation drugs and the improvements in the drug delivery systems, little research has been done on following the path of the drug particles from inhalation through the diffusion of the mucus layer to the lung epithelium. The work presented here involves the development of methods for measuring the diffusion coefficients in artificial mucus, and is part of a larger project that involves modeling transport within the lung airways, deposition, and then fate within the lung. While particulate removal from the lung can occur via exhalation and/or ciliary movement into the gastrointestinal tract, these drugs can also diffuse across the mucus layers and be taken up by the macrophages and epithelial cells lining the lung alveoli. The specific objectives of this effort are to (1) compare the composition and the physicochemical properties of artificial mucus with native mucus, (2) develop a method to measure diffusivities using FTIR, and (3) measure the diffusion coefficients of solvent and drug-doped solutions through artificial mucus layers.

An artificial mucus, representative of human pulmonary mucus, was prepared to act as a surrogate for the native mucus layer present on the lung surface. The composition of this artificial mucus solution is available in Section 3.3.1. Due to variations between specimens and properties that change with time since harvesting, artificial mucus was used for a more well-controlled system. Two commonly used drugs in asthma treatments, theophylline and albuterol, were dissolved in isopropanol and the solutions served as a

model for drug-solvent mixture that would be deposited on the mucus surface after inhalation treatments (e.g. nebulized drug solutions) are administered. Drugs are typically delivered to the in either dry powder form or dissolved in saline solution. Due to the lack of spectral variation between water-based mucus and water-based saline, isopropanol was used as the solvent for ease of tracing the progress of the diffusion.

### 3.3 Materials and Methods

#### 3.3.1 Materials

##### 3.3.1.1 Diffusants

Theophylline (>98 %, TCI America, CAS 58-55-9, M.W. 180.17 g/mol) and albuterol (Spectrum, CAS 18559-94-9, M.W. 239.31 g/mol) solutions were prepared at various concentrations using isopropanol (IPA, Ricca Chemical, 70 % v/v aqueous solution, CAS 67-63-0). The chemical structures of theophylline and albuterol are shown in Figure 3.2. Each solution was sonicated using a Branson 3510 sonicator with heat until completely dissolved. Solutions with concentrations higher than 50-mg/mL experienced dissolution when cooled at ambient temperature for times greater than thirty minutes.

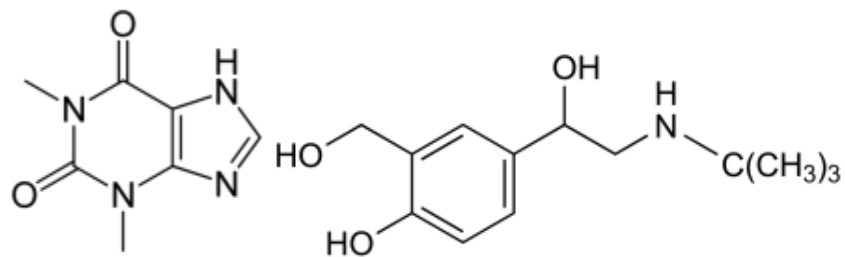


Figure 3.2 Chemical Structures of theophylline (left) and albuterol (right).

### 3.3.1.2 Preparation of Artificial Mucus

The artificial mucus was made by heating HPLC water (HPLC grade, CAS 7732-18-5, Fisher Scientific) on a hot plate to 80 °C while stirring with a magnetic stir bar. An isotonic saline solution was prepared by adding 1.57 g NaCl/NaHCO<sub>3</sub> mixture (Minimum of 70% NaCl, Ayr<sup>®</sup> saline nasal rinse packet; B.F. Ascher and Co., Inc.; Lenexa, KS) to 177 mL 80 °C HPLC water. To increase the surface tension, sodium dodecyl sulfate surfactant (BioXtra, >99.0 %, CAS 151-21-3, Sigma Aldrich) was added to the saline solution in the amount of 5 mM and mixed thoroughly. Next, 1 wt.% locust bean gum (LBG, from *Ceratonia siliqua* seeds, CAS 9000-40-2, Sigma Aldrich) was added drop by drop to the saline solution until the LBG was fully dissolved [Anwarul Hasan et al., 2010]. The artificial mucus gel became more viscous with cooling, ultimately solidifying into a semi-solid gel.

### 3.3.2 Methods: FTIR Spectroscopy

Fourier transform infrared spectroscopy was performed using a Nicolet 6700 spectrometer (Thermo Electron Corporation) and Omnic software (version 8.1.10, Thermo Fisher Scientific). Attenuated total reflectance (ATR-FTIR) spectra were collected with a 60° zinc selenide crystal with a liquid nitrogen cooled MCT-A\* (mercury-cadmium-telluride) detector and a Pike Technologies Veemax II accessory, with the angle of incidence set to 60°. Pike Technologies also produced the liquid retainer, used to contain liquid samples on top of the ATR crystal.

### 3.4 Results and Discussion

#### 3.4.1 Data Collection

Drug solution diffusion in mucus was collected and evaluated using FTIR spectroscopy. The artificial mucus layer was placed in a reservoir and a spectrum was collected to serve as a baseline standard for comparison to time-resolved spectra. Then a layer of drug-doped IPA is placed on top of the mucus layer. A schematic of this setup can be seen in Figure 3.3.

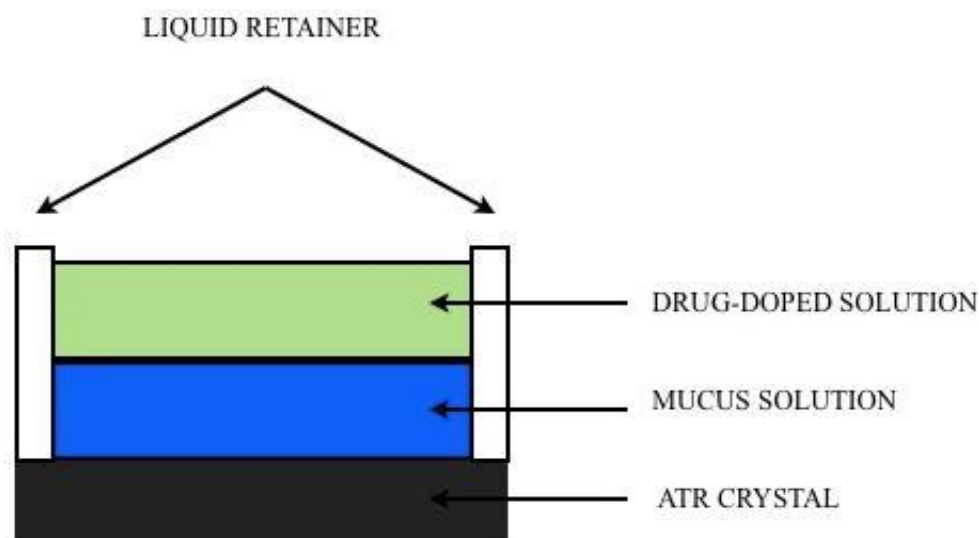


Figure 3.3 Schematic of the experimental FTIR diffusion set-up. The artificial mucus layer is sandwiched between a layer of the drug-doped solution and the ATR-FTIR crystal. Not to scale.

Figure 3.4 shows a comparison of neat IPA with the drug-doped IPA solution to show the peaks specific to theophylline. Several peaks are clearly seen in the 1750-1500  $\text{cm}^{-1}$  range for the theophylline-doped IPA solutions that are not present in neat IPA. Data collection concentrations ranged from 5-25 mg/mL.

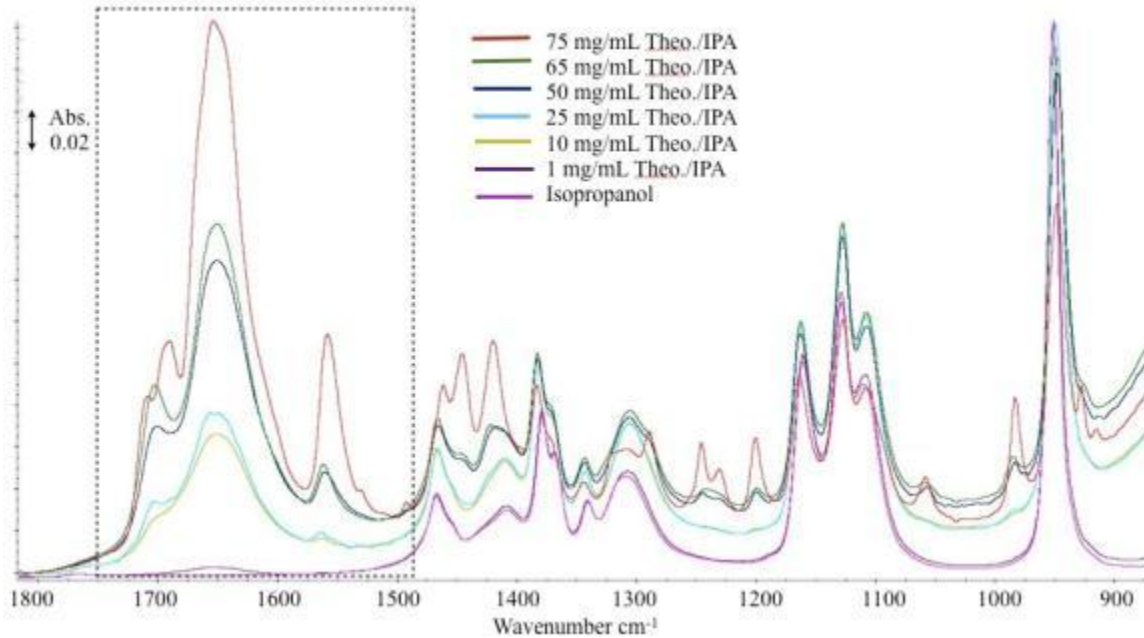


Figure 3.4 ATR-FTIR spectra for a concentration series of theophylline in IPA.

Spectra were collected at constant time intervals of sixty seconds and monitored for changes in spectral peaks corresponding to the functional groups of the drugs. With time, peaks corresponding to the drug-doped solution appeared and increased in absorbance as the concentration increased at the crystal surface. Eventually the peak heights for the solvent and drug became constant indicating an equilibrium state was achieved. An example of these time-resolved ATR-FTIR spectra for a 25 mg/mL theophylline/IPA solution diffusing through mucus is provided in Figure 3.5. The baseline spectrum ( $t = 0$  min) is a scan of the neat mucus.

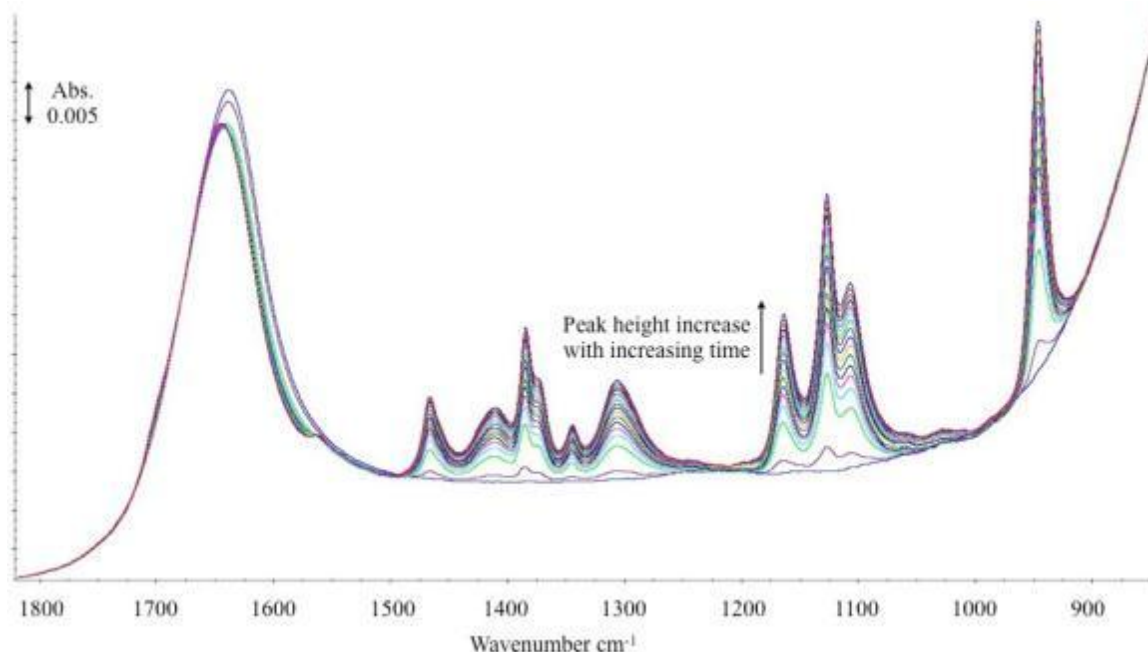


Figure 3.5 Time-resolved ATR-FTIR spectra collected over 600 sec for the diffusion of a 25 mg/mL theophylline/IPA solution through a 3.5 mm artificial mucus layer.

Examining Figure 3.5, the peaks that appear and subsequently increase in height with time correspond to the solvent (IPA) and to the drug (theophylline), with the majority of these peaks corresponding to IPA. While theophylline is present in the solution, the concentration and relatively low absorption make it difficult to differentiate from the IPA peaks. In addition, the peak at  $\sim 1645\text{ cm}^{-1}$  corresponding to the secondary amines in theophylline [Pretsch et al., 2000] is overshadowed by the large peak at  $\sim 1640\text{ cm}^{-1}$  corresponding to ring stretching of galactose and mannose [Wang and Somasundaran, 2007] in the LBG-based mucus. Stacked ATR-FTIR spectra of the mucus components can be seen in Figure 3.6.

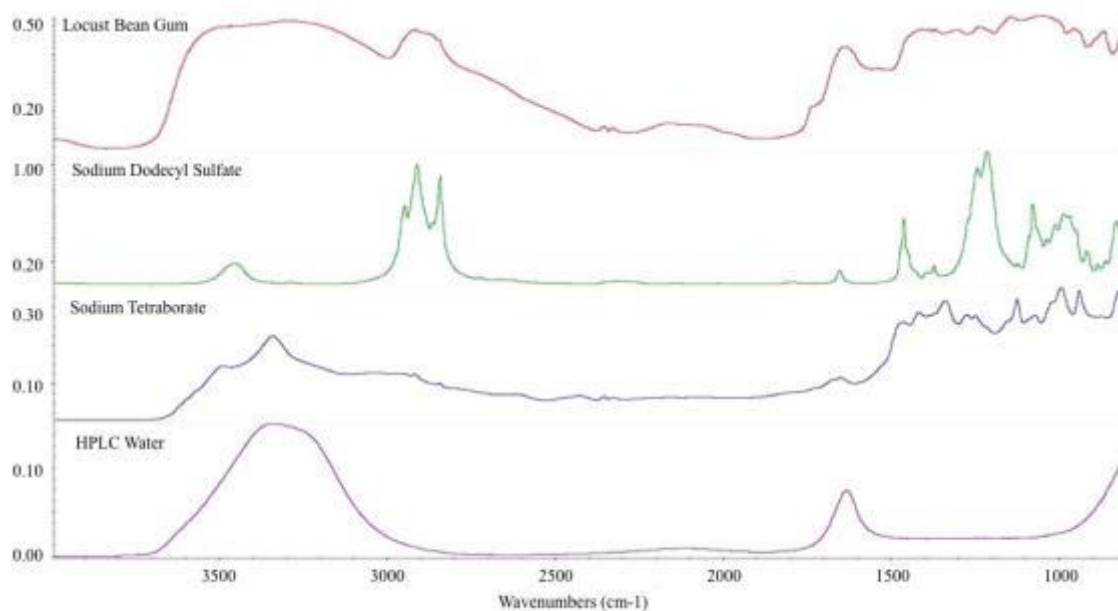


Figure 3.6 Stacked spectra of the artificial mucus components. Boxed peaks around  $\sim 1640\text{ cm}^{-1}$  are of interest due to the overshadowing the peaks have on secondary amine peaks in the drugs.

Albuterol-doped IPA solutions also contained the  $\sim 1645\text{ cm}^{-1}$  peak. Peaks in this wavenumber range correspond to secondary amines [Bruno and Svoronos, 2006; Silverstein and Webster, 1998] that are present in both chemical structures. Theophylline contains primary, secondary and tertiary amines and albuterol contains secondary amines. (Refer to the structures in Figure 3.2). The peak height tool was then used to calculate the peak height of the drug peaks at  $\sim 1645\text{ cm}^{-1}$ . These peak heights were then converted to concentration using a calibration curve, and these concentrations could be used to determine an average diffusivity coefficient, which is explained in further detail in section 3.4.2

### 3.4.2 Data Analysis

To prepare a peak height-concentration calibration curves for the drug-doped IPA solutions, first the height of the  $1645\text{ cm}^{-1}$  peak was found for each solution ranging in

from concentration from 0 to 75 mg/mL. Measured peak heights for the drug were plotted versus the corresponding concentration, and the data set was fitted to a linear function, as predicted by Beer's Law [Hallinan et al., 2010]. An example of a fitted concentration profile can be seen in Figure 3.7.

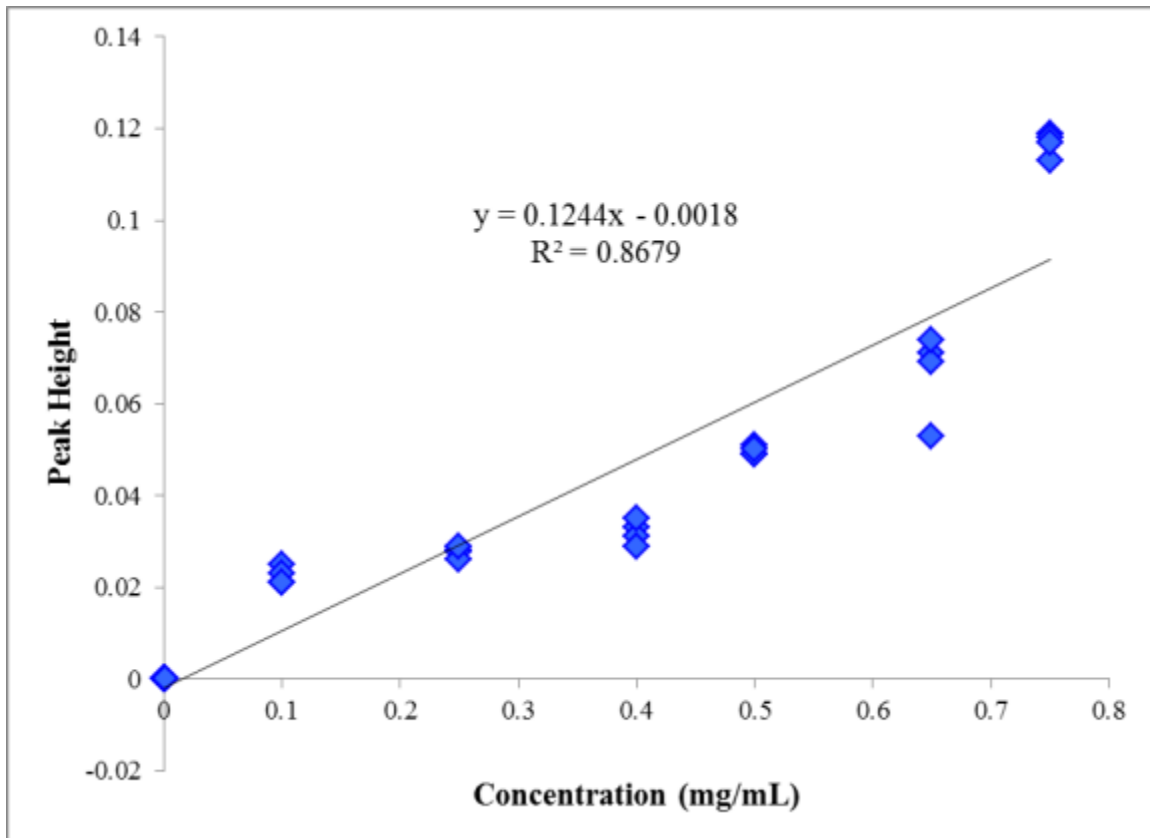


Figure 3.7 Theophylline concentration profile based on measured FTIR peak height fitted to a linear function.

Next, the peak heights of the drugs were measured for each of the time-resolved spectra. In order to evaluate the time-resolved spectra for increasing concentrations of drug-doped solutions, the neat mucus solution was subtracted from the time-resolved spectra. Using the subtraction processing method available within the Omnic software, one spectrum can be subtracted from another to more clearly identify differences; the



drug-doped IPA solution concentration could be clearly seen in the subtraction spectra. For example, a spectrum for theophylline-IPA solution through mucus at a time of 4000 seconds would look like the neat mucus solution with several IPA peaks appearing. Since it is known that theophylline is in the IPA solution and that a strong peak of mucus overshadows the traceable peak for theophylline that is present, it is necessary to remove any peaks corresponding to mucus in order to see the theophylline peak. The subtraction tool uses the neat mucus spectrum to identify the peaks corresponding to mucus and remove them from the time resolved spectrum, resulting in a spectrum that corresponds to the theophylline-IPA solution that has presently diffused through the mucus to the surface of the ATR crystal. From here, the peak height of the theophylline peak can be evaluated and subsequently used for further calculations. This evaluation method was used to find the peak height of the drug at each time interval, and the data was organized as peak height versus time. Then, using the function found by fitting the concentration profile data, the peak height versus time data was converted to concentration versus time by solving for the “x” variable of the fitted calibration curve function.

Fick’s second law of diffusion, a one-dimensional continuity equation [Hallinan et al., 2007; Elabd et al., 2003], was used to analyze the effective diffusivity (neglecting multicomponent effects) of the drugs through the mucus layer. The equation for Fick’s second law of diffusion in terms of concentration can be seen in Equation 3.1 [Hallinan et al., 2007].

$$\frac{\partial C}{\partial t} = D \frac{\partial^2 C}{\partial x^2} \quad \text{Eq. 3.1}$$

where  $C$  is concentration per unit volume of the diffusant,  $t$  is time,  $x$  is position, and  $D$  is the effective diffusion coefficient. Crank's solution of Fick’s second law differential

equation [Crank, 1975; Watkinson et al., 1994] was used to make solving for the diffusion coefficient using experimental data easier. Assuming a planar geometry with a fixed thickness,  $h$ , for the mucus layer on the lung and the two boundary conditions shown in Eqns. 3.2 and 3.3, a simplified, quantitatively solvable version of the equation is obtained (Eqn. 3.4). A schematic representation of the boundary conditions can be seen in Figure 3.8. Crank, using a Laplace Transform method, determined an approximation using trigonometric series, which was used to solve the differential equation [Crank, 1975; Hallinan et al, 2007; Elabd et al., 2003].

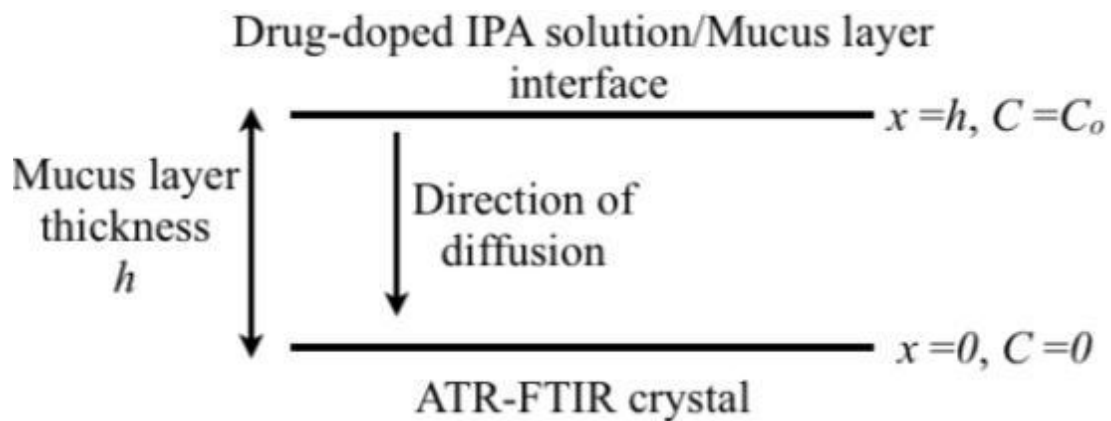


Figure 3.8 Schematic representation of boundary conditions applied to the mucus-drug diffusion system.

Boundary Condition 1:

$$(1) \quad \frac{\partial C}{\partial x} = 0 \text{ at } x = h, t \geq 0 \quad \text{Eq. 3.2}$$

Boundary Condition 2:

$$\frac{\partial C}{\partial x} = 0 \text{ at } x = 0, t \geq 0 \quad \text{Eq. 3.3}$$

$$C = C_0 - \sum_{n=1}^{\infty} \frac{4C_0}{\pi n} \exp\left(-\frac{Dn^2 t}{z^2}\right) \quad \text{Eq. 3.4}$$

Using  $C_0$ , the known reservoir concentration,  $C$ , a concentration measured at the mucus-drug solution interface,  $n$ , the series solution to the equation (number of iterations), and  $z$  as the depth of penetration of the IR source beam into the mucus layer, a solution to Equation 3.5 can be found. Excel was used to solve for  $D$ , using  $n$  values  $>500$ . Since all of the variables were known values with the exception of  $D$ , a value of  $D$  was chosen as the initial guess and then the equation is regressed until a best fit of the experimental data was achieved. In this manner, diffusivities were found for each diffusant through an artificial mucus layer. Plotting  $C/C_0$  versus time for both experimental and calculated time-resolved concentration data served as a visual tool for comparing the calculated and experimental values and therefore was used to guide and assess the direction and progress of the regression in approaching the correct diffusion coefficient for the experimental data. It should be noted that the diffusion process will have reached equilibrium when  $C/C_0 = 1$ .

Figure 3.9 illustrates the accuracy of Crank's solution using the calculated diffusivity as compared to the experimental data for drug diffusion through the mucus layer. Overall the experimental data follows the shape of the modeled curve and the values agree well at  $t < 500$  sec and  $3000 \text{ sec} < t < 9000$  sec. Deviations consistently occur between the model and experimental data between 500 and 3000 sec.

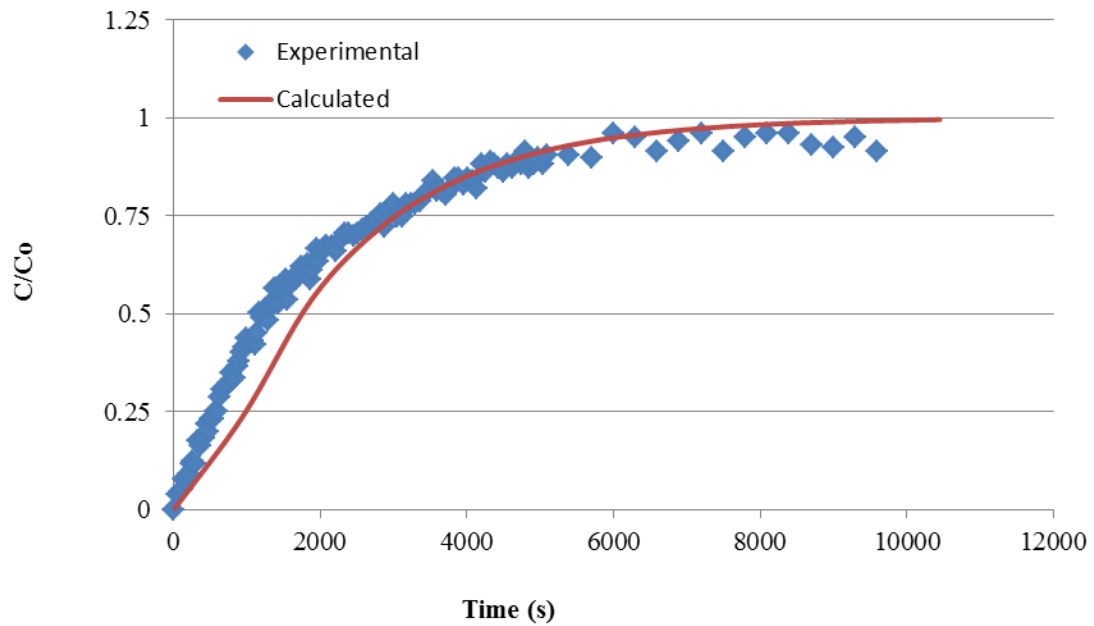


Figure 3.9 Comparison of experimental and calculated concentrations for a 10-mg/mL theophylline-IPA solution diffusing through an artificial mucus layer.

Evaluation of experimental data determined the diffusivity of theophylline (in IPA) through the mucus ranged from  $5.5\text{-}7.0 \times 10^{-6} \text{ cm}^2/\text{s}$ . Albuterol resulted in a more rapid diffusion and produced diffusion coefficients ranging from  $7.2\text{-}9.6 \times 10^{-6} \text{ cm}^2/\text{s}$ . The single-ring structure of albuterol may contribute to the faster diffusion as opposed to the two-ring structure of theophylline due to steric hindrance. Molecular weight is also a contributing factor in the diffusion; albuterol MW is 239.31 g/mol and theophylline MW is 180.17 g/mol. This matches the trend seen in the literature; higher molecular weight drugs have been found to diffuse more rapidly through the mucus layer [Larhed et al., 1997; Khanvilkar et al, 2001]. Albuterol was found to diffuse faster through the mucus layer in the experimental system used in this research, which supports the reported correlation of higher molecular weight particles and rate of diffusion presented in

literature. Table 3.1 summarizes the range of diffusion coefficients measured using the FTIR diffusion method for theophylline and albuterol.

Table 3.1 Summary of measured diffusivity coefficients for theophylline and albuterol in artificial mucus.

Drug	Solution Concentration (mg/mL)	Total Data Collection Time (s)	Mucus Layer Thickness (cm)	Diffusivity ( $10^{-6} \text{ cm}^2/\text{s}$ )	95% Confidence Interval
Theophylline	5-25	6,900-10,800	0.15-0.35	5.5-7.0	$\pm 0.12$
Albuterol	5-30	1,500-5,100	0.15-0.40	4.9-9.6	$\pm 0.59$

The diffusion coefficient values for aerosol drugs through mucus ranged from 4.9-9.6 x  $10^{-6} \text{ cm}^2/\text{s}$ , and specific examples are given below. In the literature, homologous carbohydrates glucuronic acid, glucosmine, and mannitol diffused through native porcine mucus produced diffusivity values ranging from 7-9 x  $10^{-6} \text{ cm}^2/\text{s}$ , while the lipophilic molecule testosterone produced a diffusivity of 3 x  $10^{-6} \text{ cm}^2/\text{s}$  [Larhed et.al., 1997]. Drugs such as isonicotinic acid hydrazide, sodium *p*-aminosalicylate, pentamidine, pyrazinamide, and rifampicin produced diffusivity values ranging from 5.07-7.62 x  $10^{-6} \text{ cm}^2/\text{s}$  when diffused through reconstituted mucus [Bhat et al., 1995]. Theophylline diffusion coefficients have been reported as 2 x  $10^{-6} \text{ cm}^2/\text{s}$  [Grassi et al., 2003] and 1.83 x  $10^{-5}$ -5.83 x  $10^{-9} \text{ cm}^2/\text{s}$  [Alvarez-Lorenzo et al., 1999]. Based on literature findings, the range of experimental diffusivity values measured in this work appears to be appropriate for the materials tested thereby validating the FTIR- based data collection and analysis methods.

### 3.5 Conclusions

Based on the data that was collected and analyzed for the diffusion of theophylline and albuterol through artificial mucus, the average diffusivity coefficients that were calculated are accurate representations of how the drugs behave in human pulmonary mucus. The methods of analysis employed in the evaluation of the data resulted in expected increases in peak heights of the drug-specific peak, and followed the expected pattern of a period of steady peak height increase with increasing time followed by a period of unchanging peak heights, indicating equilibrium. While the diffusivities were expected to be slightly lower, the data was consistent in the diffusivity coefficient values that were found regardless of mucus layer thickness or the length of time data was collected. The consistency of the data reiterates the validity of this experimental setup and method of spectral peak and resulting quantitative data analysis.

### 3.6 References

- Alvarez-Lorenzo, C.; Gomez-Amoza, J.L.; Martinez-Pacheco, R.; Souto, C.; Concheiro, A. Microviscosity of hydroxypropylcellulose gels as a basis for prediction of drug diffusion rates. *Internal Journal of Pharmaceutics*, 1999, 180 (1), 91-103.
- Anwarul Hasan, M.D.; Lange, Carlos F.; King, Malcolm L. Effect of artificial mucus properties on the characteristics of airborne bioaerosol droplets generated during simulated coughing. *Journal of Non-Newtonian Fluid Mechanics*, 2010, 165, 1431-1441.
- Bhat, Pavan G.; Flanagan, Douglas R.; Donovan, Maureen D. The limiting role of mucus in drug absorption: drug permeation through mucus solution. *International Journal of Pharmaceutics*, 1995, 126, 179-187.
- Bruno, Thomas J.; Svoronos, Paris D.N. CRC Handbook of Fundamental Spectroscopic Correlation Charts. Taylor and Francis: Boca Raton, FL, 2006.
- Chan, Hak-Kim. Dry Powder Aerosol Delivery Systems: Current and Future Research. *Journal of Aerosol Medicine*. 2006, 19.1, 21-27.
- Crank, J. The Mathematics of Diffusion. New York: Oxford University Press, 1975, 21-24.
- Elabd, Yossef A.; Baschetti, Marco Giacinti; Barbari, Timothy A. Time-resolved Fourier transform infrared/attenuated total reflection spectroscopy for the measurement of a molecular diffusion in polymers. *Journal of Polymer Science Part B: Polymer Physics*, 2003, 41, 2794-2807.
- El-Gendy, Nashwa; Pornputtapitak, Warangkana; Berkland, Cory. Nanoparticle agglomerates of fluticasone propionate in combination with albuterol sulfate as dry powder aerosols. *European Journal of Pharmaceutical Sciences*, 2011.
- Grassi, Mario; Voinovich, Dario; Franceschinis, Erica; Perissutti, Beatrice; Filipovic-Grcic, Jelena. Theoretical and experimental study on theophylline release from stearic acid cylindrical systems. *Journal of Controlled Release*, 2003, 92 (3), 275-289.
- Hallinan, Jr., Daniel T.; Elabd, Yossef A. Diffusion and sorption of methanol and water in nafion using time-resolved Fourier transform infrared – attenuated total reflectance spectroscopy. *Journal Physical Chemistry Volume B*, 2007, 111, 13221-13230.
- Hallinan Jr., Daniel T.; De Angelis, Maria Grazia; Baschetti, Marco Giacinti; Sarti, Giulio C.; Elabd, Yossef A. Non-Fickian diffusion of water in nafion. *Macromolecules*, 2010, 43, 4667-4678.
- Khanvilkar, Kavita; Donovan, Maureen D.; Flanagan, Douglas R. Drug transfer through mucus. *Advanced Drug Delivery Reviews*, 2001, 48, 173-198.

Lai, Samuel K.; Wang, Ying-Ying; Hanes, Justin. Mucus-penetrating nanoparticles for drug and gene delivery to mucosal tissues. *Advanced Drug Delivery Reviews*, 2009, 61, 158-171.

Larhed, Agneta Wikman; Artursson, Per; Grasjo, Johan; Bjork, Erik. Diffusion of Drugs in Native and Purified Gastrointestinal Mucus. *Journal of Pharmaceutical Sciences*, 1997, 86 (6), 660-665.

Larhed, Agneta Wikman; Artursson, Per; Bjork, Erik. The influence of intestinal mucus components on the diffusion of drugs. *Pharmaceutical Research*, 1998, 15, 66-71.

Norris, D.A.; Sinko, P.J. Effect of size, surface charge, and hydrophobicity on the translocation of polystyrene microspheres through gastrointestinal mucin. *Journal of Applied Polymer Science*, 1997, 63, 1481-1492.

Owen, D.H.; Dunmire, E.N.; Plenys, A.M.; Katz, D.F. Factors influencing nonoxynol-9 permeation and bioactivity in cervical mucus. *Journal of Controlled Release*, 1999, 60, 23-24.

Pretsch, E.; Buhlmann, P.; Affolter, C. Structure of Determination of Organic Compounds, Tables of Spectral Data; Springer: New York, 2000; p. 269.

Shaw, Lance R.; Irwin, William J.; Grattan, Tim J.; Conway, Barbara R. The influence of excipients on the diffusion of ibuprofen and paracetamol in gastric mucus. *International Journal of Pharmaceutics*, 2005, 290, 145-154.

Silverstein, R.M.; Webster, F.X. Spectrometric Identification of Organic Compounds; John Wiley & Sons Inc.: New Jersey, 1998.

Todoroff, Julie; Vanbever, Rita. Fate of nanomedicines in the lungs. *Current Opinion in Colloid and Interface Science*, 2011, 16(3), 246-254.

Volsko, Teresa; Reed, Michael D. "Drugs used in the treatment of asthma". *Respiratory care clinics of North America*, 2000, 6(1), 41-55.

Wang, Jing; Somasundaran, Ponisseril. Study of galactomannose interaction with solids using AFM, IR and allied techniques. *Journal of Colloid and Interface Science*, 2007, 309, 373-383.

Watkinson, A.C.; Hadgraft, J.; Walters, K.A.; Brain, K.R. Measurement of diffusional parameters in membranes using ATR-FTIR spectroscopy. *International Journal of Cosmetic Science*, 1994, 16, 199-210.



CHAPTER IV  
INTRODUCTION TO POLYMER SURFACE MODIFICATION USING LIGHT-  
EMITTING POLYMERS

**4.1 Background: Polymer Surface Modification**

Polymers are one of the most versatile and widely used materials in modern society. They are inexpensive and have a multitude of applications from food packaging to biomedical containment to automotive parts [Unver et al., 2011]. Polymer films are of particular interest due to their desirable characteristics that contribute to their successful applications. In addition to excellent bulk properties, such as high temperature stability and strong chemical resistivity, polymer films can be processed by several different methods and are available in a wide range of thicknesses.

For many applications, one of the most important characteristics of polymers is the surface chemical composition. Surface composition affects the interactions of the polymer with its surroundings and consequently the applications. Polymers can be easily modified into a customized product for a specific use [Unver et al., 2011]. Surface modified polymers can be designed and tailored for specific applications without altering the bulk material. Surface modified polymers can be found in a range of products from coatings, composites, adhesive tape, textiles [Scaffaro et al., 2011], and biomaterials [Pasparakis et al., 2010].

Polymer surface modification can be achieved through several commonly used techniques. Methods such as dip coating and spin coating are empirical methods of

surface modification that are regularly employed [Tighilt et al., 2008]. Plasma treatment is a technique used for polymeric surface modification where several activated species (electrons, ions, free radicals, and some neutral species) [Ma et al., 2012] are used to expose a surface of the polymer to a non-polymerizing plasma or by depositing a thin layer of plasma polymer on the surface of the polymer [Yasuda, 1977]. Properties such as adhesion, friction coefficient, optical reflection, surface energy, permeability, and biocompatibility of several polymers can be controlled [Castro Vidaurre et al., 2002]. Plasma treatment alters the surface characteristics of the polymer but does not affect the bulk properties due to the low depth of penetration [Castro Vidaurre et al., 2002]. Surface modification via the covalent reaction of small molecules is another method used with increasing frequency. By either creating or utilizing existing surface functionality of the polymer, the surface functional groups can be covalently altered. By modifying the surface only, the resultant material's surface chemistry is often achieved with increased control over the final product as well as a more stable and permanent product compared to those resulting from other surface modification methods [Zhang et al., 2006].

There has been extensive research into the grafting of materials onto and from polymer surface substrates. However, only a limited amount of research has investigated the grafting of end-functionalized polymers from a solid polymer surface [Walters and Hirt, 2006]. Polymer films can support the grafting of a range of molecules due to their versatile physical and chemical properties. Using covalent bonding surface modification, very unique polymer films can result with specific properties, making them a material of high interest due to this “custom-made” functionality [Luo et al.; 2004].

Conceptual understanding of polymer chemistry at the molecular level allows for the development of desired functional materials. Designing functional polymer films

requires the knowledge not only of molecular interactions, but also the chemical reactions the film will have with its environment. Implementing the design requires careful control. It is also important to recognize that while some materials respond to a particular stimulus, orientation on the grafting substrate will affect how the response will progress. Functional groups that are present on the reacting substrate react with the responsive functional groups. Occasionally, the spacing of the reactive functional groups on the polymer film backbone may be too large or small and affect the degree of the response [Scaffaro et al., 2011]. Additionally, the designer needs to choose the polymer substrate wisely and take into account the affect some environmental factors will have on some polymers. Exposure to high temperatures, extensive light, acids or other chemicals that can negatively impact many properties of the polymer can cause adverse effects, such as polymer degradation. Despite these negative performance characteristics of polymers, the benefits of their versatility and ability to handle most extreme environments compensates for the challenges that are encountered [Lawandy, 1982]. With this understanding, polymer films can be designed to have a specific response to particular external stimuli. Grafting stimuli-responsive molecules, monomers, or polymers to the polymer films will result in a stimuli responsive polymer film, which can be affected by pH, temperature, radiation, magnetic field, or light, among others. The responses of polymers exist in a wide range such as a change in color, transparency, conductivity, shape (shape memory polymers), size, refractive index, crosslinking, and chain recombination, among other events [Lawandy, 1982]. Stimuli-responsive polymers are also referred to as “smart polymers” and are found in everyday products as well as specialty applications [Thomson, 2005; Luo et al., 2004].

Light-sensitive polymer films are the application of interest in this study. Light-sensitive polymer films fluoresce a color in the visible spectrum and can be used in a multitude of applications [Perepichka et al., 2006]. Light bulbs, computers, radiation dosimeters, and light emitting diodes (LEDs) televisions are only a few of these commercial uses. The concentration of this research is in light-sensitive polymer films that change color in response to irradiation.

#### **4.2 Uses of Light-Emitting Polymers**

LEDs are one of the most common uses for light-emitting polymers since the 1990s. Some LEDs are capable of emitting light across the visible, ultraviolet and infrared wavelengths. In the application of electroluminescence, light emission is observed when a voltage is applied through a conductive polymer. This technique is used in liquid crystal display (LCD) televisions as well as quantum dots, computers, and light bulbs, among others [Perepichka et al., 2006]. LEDs are also being investigated for prospective use in ink-jet printers due to their potential in development of the desired primary color emissions of red-green-blue on a single substrate [Deng and Wong, 2009].

Photopolymers change properties typically in response to ultraviolet light. These polymers have been used in fillings in dentistry as well as etching [Danesh et al., 2004]. The polymer is soft initially, formed into the desired shape, then cured with UV light. Shape-memory plastics are a type of photopolymer that change shape in response to temperature increase and as recently found, light [Thomson, 2005]. Researcher Robert Langer at the Massachusetts Institute of Technology developed, with German colleagues, programmable plastics that change shape in response to specific wavelengths of light [Thomson, 2005]. Photosensitive groups are grafted onto a polymer film and stretched

with an external stress. Once illuminated with specific wavelength of UV light, crosslinking occurs within the molecular network, changing the shape of the polymer film. When illuminated with UV light at a different wavelength, the cross-linked molecules cleave and the polymer film reverts back to its original shape. These researchers are hoping to use this technology for applications such as minimally invasive surgery. For example, a polymer string could be threaded into the body through a small incision and when activated by light would alter its physical characteristics, becoming a corkscrew shaped stent for keeping blood vessels open [Thomson, 2005]. There could also be possible office supply applications, such as quick release staples or paper clips that relax when not in use [Thomson, 2005].

Another highly investigated and successful use for light emitting polymers is radiation detection. Countless studies have been performed on light-emitting polymers and the effects that various types of irradiation have on these materials. Polymer-based dosimeter systems have been in use for over 60 years [Liz et al., 2011]. Self-indicating instant radiation alert dosimeter (SIRAD) badges, developed by JPLabs Inc., are widely used as X-ray radiation exposure prevention tools in industry. These badges contain a diacetylene compound that is colorless until irradiated with X-ray radiation [Buston et al., 2006]. Increasing levels of radiation result in a stronger blue color emission from the badge [Cheung et al., 2007]. For other types of radiation, surface-modified polystyrene films have been studied for use as reusable gamma radiation detectors. Depending on the specific light-emitting chemicals grafted to the surface of the polystyrene film, exposure brings a blue or red color change [Irie and Irie, 2000]. The absorption intensities of both blue and red film types increased linearly with the absorbed dose [Irie and Irie, 2000]. Various metal-substituted phthalocyanines, such as copper phthalocyanine (CuPc), have

also been investigated as potential gamma radiation detectors [Arshak, A. et al., 2004]. These polymers were blended into a 92% CuPc 8% poly with diethylenglycolmonobutylether as the solvent [Arshak, K. et al., 2004] have been spin coated onto metal oxide substrates with varying thicknesses and evaluated for their response with gamma irradiation, with  $^{60}\text{Co}$  and  $^{137}\text{Cs}$  sources used to irradiate the samples. It has been reported that the CuPc coated metal film emitted at ~600-690 nm range, which is in the orange-red range of the visible spectrum [Arshak, A. et al., 2004]. In addition to diacetylene- and phthalocyanine-based dosimeters, polyester, fluoropolymer, vinyl, and acrylate polymers have also been investigated for use in gamma ray dosimeters [Liz et al., 2011].

### 4.3 Classes of Light-Emitting Polymers

Conjugated polymers are organic semiconductors [Lambeth, 2004] and have strong fluorescent properties. These molecules, when irradiated, emit light in the visible UV range. When the absorption maximum in the spectrum is in the UV visible range, the polymer will fluoresce [Perepichka et al., 2006]. Several conjugated aromatic polymers will be discussed in terms of their structure, light emitting properties, and applications. These materials also have excellent film forming characteristics and have the ability to be easily applied to large surfaces using simple and cost-effective techniques such as spin coating or ink jet printing [Lambeth, 2004].

Poly(*p*-phenylene vinylene) (PPV) is a very commonly used green-yellow-emitting conductive polymer [Wu and Chen, 2011], and its chemical structure is shown in Figure 4.1. PPV was the first polymer to show electroluminescence [Ruddy, 2006; Perepichka et al.; 2006]. PPVs are useful for red and green emission, but lack the ability

to emit blue light due to the large band gap required for blue emission [Lambeth, 2004]. PPV does have the ability to crosslink the main chains by simultaneous UV irradiation and annealing, and this technique has been investigated to achieve blue emission with PPV [Deng and Wong, 2009]. While crosslinking can result in color variations, further processing is required to achieve simultaneous multiple colors from a PPV derivative on a single device. Photo-lithographical patterning through multi-step solution processing to remove unwanted polymers or photochemical reactions of particular conjugated vinyl-containing polymers was needed to achieve multiple-color PPV products [Deng and Wong, 2009].

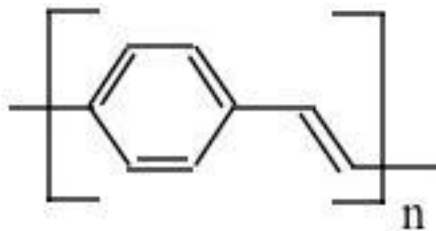


Figure 4.1 Chemical structure of poly(*p*-phenylenevinylene) (PPV).

A second benefit of PPV is that it can be easily modified with functional side groups. Most research has been done on modifying the benzene ring [Perepichka et al., 2006]. The addition of these groups often changes the color the chemical fluoresces. One example is MEH-PPV (poly [2-methoxy-5-(2'-ethylhexyloxy)-*p*-phenylene vinylene]). MEH-PPV is one of the most frequently used polymers in the PPV class of light-emitting polymers and upon excitation emits in the red-orange (590 nm) range of the visible spectrum [Zhao et al., 2007; Deng and Wong, 2009]. Other examples of functional groups altering color emitting properties are blue-emitting diphenyl substituted structures and green-emitted diphenylamino-substituted structures [Perepichka et al., 2006].

PPVs were used in the first polymer based LEDs [Perepichka et al, 2006], and continue to be used in a wide range of LED applications. Additionally, PPV derivatives are also used as an electron-donating material in organic solar cells, despite their tendency to photodegrade.

Polyacetylene (PA) was the first reported class of conducting polymer [Ruddy, 2006]. While not aromatic, PA does contain alternating single and double bond carbon chain and therefore is still a conjugated system. Figure 4.2 shows the chemical structure of polyacetylene.

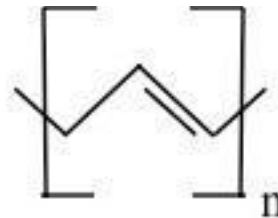


Figure 4.2 Chemical structure of polyacetylene (PA).

Since PA was discovered to be electrically conductive in 1977 [Ruddy, 2006], it has been well classified and its material characteristics thoroughly investigated. While unsubstituted PA is non-emissive [Perepichka et al., 2006], PA has undergone successful experimentation with disubstitution including biphenyls, which produced a violet fluorescence (350-370 nm) [Perepichka et al., 2006]. Polyacetylenes have also been the basis of liquid crystal applications. Neat polyacetylene is insoluble in organic solvents, so introducing liquid crystalline substituents into the main polyacetylene chain or by disubstitution attached to the main polymer chain using alkyl spacers results in a soluble, fluorescing liquid [San Jose et al., 2011]. Depending on the substituents of the side chains, the polymers exhibit blue or green photoluminescence [San Jose et al., 2011].



Polyfluorene (PF) is another frequently used class of light emitting polymers. PFs are a blue-emitting class of light emitting polymers and exhibit high photoluminescence quantum yields [Zhao et al., 2009; Jhaveri et al., 2009], good solubility in common organic solvents [Zhao et al., 2009; Perepichka et al., 2006], and thermal stability [Perepichka et al., 2006]. The chemical structure of polyfluorene is shown in Figure 4.3.

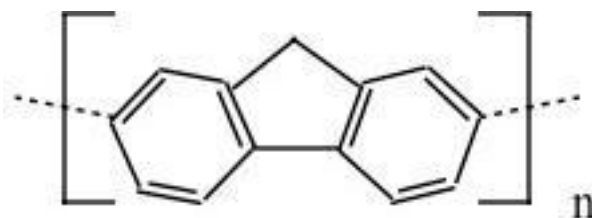


Figure 4.3 Chemical structure of polyfluorene (PF).

PFs are most often used in light-emitting diodes (LEDs) [Zhao et al., 2009] and photovoltaic cells [Goktas et al., 2012]. PFs are easily modified by functional group attachment into the C-2, C-7, or C-9 positions of the fluorenes [Zhao et al., 2009; Jhaveri et al., 2009], by copolymerization, and by functionalizing the methylene bridge for the fine-tuning of emissive properties [Perepichka et al., 2006; Ruddy, 2006].

Yet another type of light-emitting polymer is polydiacetylene (PD). The structure of PD is shown in Figure 4.4. These polymers emit red, blue (the most common colors of PD crystals and films [Filhol, 2009]), or purple, depending on the delocalization of  $\pi$ -electrons on the conjugated backbone. The variations in color emission indicate the possibility of more than two electronic structures of PD chains [Filhol, 2009]. The emitted color from PDs is dependent on the environmental temperature, solvent polarity, electromagnetic field [Araya, 1991], applied stress, light exposure, and changes in chemical environment [Filhol, 2009].

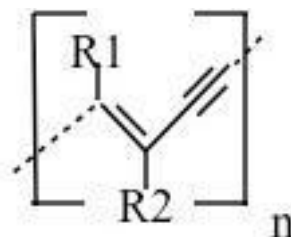


Figure 4.4 Chemical structure of the repeat unit for polydiacetylene (PD).

#### 4.4 Research Objectives

The primary objective is to covalently graft light-sensitive polymers to polymer films substrate in order to create light-sensitive films. (Note: This effort is a first step into generating beta- and gamma-radiation sensitive polymers.) In order to graft light-sensitive chemicals onto the polymer film substrate, the film surface chemistry must be modified. A survey was made of light-sensitive chemicals and their chemical structures in order to decide on which functional groups would likely allow for facile grafting to the surface-modified polymer films. The reaction steps were monitored using Attenuated Total Reflectance Fourier Transform Infrared (ATR-FTIR) spectroscopy, and the resultant light-sensitive modified films were characterized using UV-Vis spectroscopy and fluorescence spectroscopy.

While the development and existence of radiation-responsive polymer films are not novel, most light-sensitive polymer films are not achieved through surface grafting. The techniques of spin coating and dip coating are more frequently used, as observed through extensive literature research. Employing surface grafting techniques to attain light-sensitive polymer films further develops the field and brings forth future opportunities to develop other films sensitive to different types of radiation.

## 4.5 Approach

Two light-sensitive chemicals were selected based on the interest in investigating different classes of light-sensitive chemicals (polyphenylenes and polyfluorenes) and the expected ease of grafting these chemicals to the selected polymer film, poly(ethylene-co-acrylic acid) (EAA). The free carboxyl groups on the polymer backbone [Scaffaro, 2011] make EAA an ideal substrate for surface modifications. Both light-emitting chemicals contain functional groups that will allow them to be grafted to the surface-modified polymer film structure. One of the light-sensitive chemicals investigated, 4'-(octyloxy)-4-biphenyl carboxylic acid (OBC), is a polyphenylene class chemical and contains a terminal carboxylic acid group that can be used to attach it to the polymer film (Figure 4.5). OBC is expected to fluoresce in the blue-green range due to the polyphenylene and biphenyl structure [San Jose 2011].



Figure 4.5 Chemical structure of 4'-(octyloxy)-4-biphenyl carboxylic acid (OBC).

Figure 4.6 shows the structure of the other light-sensitive chemical investigated, 2,7-bis (bromomethyl)-9,9-dihexyl-9H-fluorene (BDMF), a polyfluorene class chemical. BDMF is expected to fluoresce in the blue range of the emission spectra, since polyfluorenes typically fluoresce blue [Zhao et al., 2009].

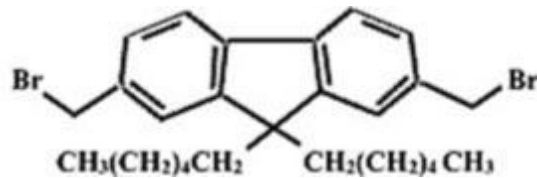


Figure 4.6 Chemical structure of 2,7-bis (bromomethyl)-9,9-dihexyl-9H-fluorene (BDMF).

## 4.6 References

- Araya, K. Reversible Color Changes of Polydiacetylene Induced by Monomer Solid Phase Transition. *Bulletin of the Chemical Society of Japan*, 1991, 64, 730-731.
- Arshak, A.; Arshak, K.; Korostynska, O.; Zleetni, S. Review of Various Gamma Radiation Dosimeters Based on Thin and Thick Films of Metal Oxides and Polymer Materials. *IEEE*, 2004, 78-82.
- Arshak, K.; Arshak, A.; Zleetni, S.; Korostynska, O. Thin and thick films of metal oxides and metal phthalocyanines as gamma radiation dosimeters. *IEEE Transactions on Nuclear Science*, 2004, 51, 2250-2255.
- Buston, Martin J.; Cheung, Tsang; Yu, Peter K.N. Visible Absorption Spectra of Radiation Exposed SIRAD Dosimeters. *Physical Medicine and Biology*, 2006, 51, N417-N421.
- Castro Vidaurre, E.F.; Achete, C.A.; Gallo, F.; Garcia, D.; Simao, R.; Habert, A.C. Surface Modification of Polymeric Materials by RF-Plasma Treatment. *Materials Research*, 2002, 5, 37-41.
- Cheung, T. et al. "X-Ray energy dependence of the dose response of SIRAD radiation dosimeters". *Applied Radiation and Isotopes*, 2007, 65, (814-817).
- Danesh, Gholamreza; Davids, Hendrick; Reinhardt, Klaus-Jurgen; Ott, Klaus; Schafer, Edgar. Polymerisation characteristics of resin composites polymerized with different curing units. *Journal of Dentistry*, 2004, 32, 479-488.
- Deng, X.; Wong, K.Y. Cross-Linked Conjugated Polymers for Achieving Patterned Three-Color and Blue Polymer Light-Emitting Diodes with Multi-Layer Structures. *Macromolecular Rapid Communications*, 2009, 30, 1570-1576.
- Filhol, Jean-Sebastien; Deschamps, Jerome; Dutremez, Sylvain G.; Boury, Bruno; Barisien, Thierry; Legrand, Laurent; Schott, Michel. Polymorphs and colors of polydiacetylenes: A first principles study. *Journal of the American Chemical Society*, 2009, 131, 6976-6988.
- Goktas, Hilal; Mansuroglu, Dogan; Atalay, Betul; Bilikmen, Sinan; Kaya, Ismet. Polyfluorene thin films synthesized by a novel plasma polymerization method. *Plasma Chemistry and Plasma Processing*, 2012, 32, 35-44.
- Irie, S.; Irie, M. "Radiation-Induced Coloration of Photochromic Dithienylethene Derivatives in Polymer Matrices". *Bull. Chem. Soc. Jpn.*, 2000, 73, 2385-2388.

Jhaveri, Sarav B.; Peterson, Joseph J.; Carter, Kenneth R. Poly(9,9-Dihexylfluorene) layers grown via surface-directed Ni(0) condensation polymerization. *Langmuir*, 2009, 25, 9552-9556.

Lambeth III, Robert H. Electroluminescence of conjugated aromatic polymers in organic light emitting diodes. 2004.  
[http://www.chemistry.illinois.edu/research/organic/seminar\\_extracts/2004\\_2005/2\\_Lambeth\\_Abstract\\_SP05.pdf](http://www.chemistry.illinois.edu/research/organic/seminar_extracts/2004_2005/2_Lambeth_Abstract_SP05.pdf) (Accessed Feb 25, 2012).

Lawandy, S.N. Color Measurements for Detection of Radiation Damage in Polymers. *Elastomerics*, 1982, 33-35.

Liz, O.S.R.; Medeiros, A.S.; Faria, L.O. FTIR and DSC studies on gamma irradiated P(VdF-HFP) fluoropolymers applied to dosimetry. *Nuclear Instruments and Methods in Physics Research B*, 2011, 269, 2819-2823.

Luo, Ning; Husson, Scott M.; Hirt, Douglas E.; Schwark, Dwight W. Surface Grafting of Polyacrylamide from Polyethylene-Based Copolymer Film. *Journal of Applied Polymer Science*, 2004, 92, 1589-1595.

Ma, Gui-qui; Liu, Ben; Li, Chen; Huang, Dinghai; Sheng, Jing. Plasma modification of polypropylene surfaces and its alloying with styrene *in situ*. *Applied Surface Science*, 2012, 258, 2424-2432.

Pasparakis, George; Krasnogor, Natalio; Cronin, Leroy; Davis, Benjamin; Alexander, Cameron. Controlled polymer synthesis – from biomimicry towards synthetic biology. *Chemical Society Reviews*, 2010, 39, 286-300.

Perepichka, Dmitrii F.; Perepichka, Igor F.; Meng Hong; Wudl, Fred. Light Emitting Polymers, *Organic Light-emitting Materials and Devices*, Marcel-Dekker Inc., CRC Press, 2006.

Ruddy, Bryan P. Conducting Polymer Wires for Intravascular Neural Recording. Master of Science Thesis, Massachusetts Institute of Technology, Cambridge, MA, 2006. p. 15.  
Zhao, Qiang; Huang, Zonghao; Wang, Cheng; Zhao, Qidong; Sun, Haizhu; Wang, Dejun. Preparation of PVP/MEH-PPV composite polymer fibers by electrospinning and study of their photoelectronic character. *Materials Letters*, 2007, 61, 2159-2163.

San Jose, Benedict A.; Matsushita, S.; Moroishi, Y.; Akagi, K. Disubstituted Liquid Crystalline Polyacetylene Derivatives That Exhibit Linearly Polarized Blue and Green Emissions. *Macromolecules*, 2011, 44, 6288-6302.

Scaffaro, Robert; Botta, Luigi; Lo Re, Giada; Bertani, Roberta; Milani, Roberto.; Sassi, Alessandro. Surface modification of poly (ethylene-co-acrylic acid) with amino-functionalized silica nanoparticles. *Journals of Materials Chemistry*, 2011, 21, 3849.

Thomson, Elizabeth A. Intelligent Plastics Change Shape with Light. MIT News April 13, 2005. <http://web.mit.edu/newsoffice/2005/smart-plastics> (Accessed October 25, 2011).

Tighilt, F.Z.; Belhaneche, N.; Gabouze, N. Study of polystyrene film coating on the surface of porous silicon. *Physica Status Solidi (C) Current Topics in Solid State Physics*, 2008, 5, 3698-3700.

Unver, Elif Kose; Tarkuc, Simge; Udum, Yasemin Arslan; Tanyeli, Cihangir; Toppare, Levent. The Effect of the Donor Unit on the Optical Properties of Polymers. *Organic Electronics* 2011, 12, 1625-1631.

Walters, Keisha B.; Hirt, Douglas E. Grafting of End-Functionalized Poly(*tert*-butyl acrylate) to Poly (ethylene-*co*-acrylic acid) film. *Polymer* 2006, 47, 6567-6574.

Wu, Chia-Shing; Chen, Yun. Copolyfluorenes Containing Pendant Bipolar Carbazole and 1,2,4-Triazole Groups: Synthesis, Characterization, and Optoelectronic Applications. *Journal of Polymer Science Part A*, 2011, 49, 3928-3938.

Yasuda, H. Modification of polymers by plasma treatment and by plasma polymerization. *Radiation Physics and Chemistry*, 1977, 9, 805-817.

Zhang, Chun; Luo, Ning; Hirt, Douglas E. Surface grafting polyethylene glycol (PEG) onto poly(ethylene-*co*-acrylic acid) films. *Langmuir*, 2006, 22, 6851-6857.

Zhao, Qiang; Liu, Shu-Juan; Huang, Wei. Polyfluorene-Based Blue-Emitting Materials. *Macromolecular Chemistry and Physics*, 2009, 210, 1580-1590.

CHAPTER V  
MODIFICATION AND CHEMICAL GRAFTING OF POLY(ETHYLENE-CO-  
ACRYLIC ACID) FILMS

**5.1 Abstract**

Two molecules, 4'-(octyloxy)-4-biphenyl carboxylic acid (OBC) and 2,7-bis(bromomethyl)-9,9-dihexyl-9H-fluorene (BDMF), were grafted to the surface of poly(ethylene-co-acrylic acid) (EAA) films. OBC and BDMF were selected due to their light sensitivity and potential for applications utilizing light-sensitive polymer films. Carboxylic acid groups on the surface of the EAA films were converted to acid chloride groups and then reacted with ethylene diamine to provide primary amines. The primary amine groups served as the reactive sites to graft the OCB and BDMF molecules onto the EAA films. The progression of each reaction was confirmed using attenuated total reflectance Fourier transform infrared (ATR-FTIR) spectroscopy and static contact angle. Based on the results from these analysis techniques, each reaction step can be confirmed as well as the successful grafting of OBC and BDMF to the EAA films.

**5.2 Introduction**

There has been extensive research into the grafting of materials to polymer substrates. Researchers have investigated the grafting of a range of constituents such as acryloyl chloride to obtain liquid crystalline polymer films [Burillo et al., 1997], proteins onto crosslinked polymer hydrogel membranes, and ethylene vinyl alcohol copolymer films [Ikada et al., 1979]. Despite the substantial research into polymers grafted to a

substrate, only a limited amount of research has investigated the grafting of materials from a solid polymer film [Walters and Hirt, 2006].

The versatility of polymers films makes them a practical choice for many applications. The bulk properties of polymers are ideal for supporting the grafting of a range of molecules resulting in a wide variety of films. Polymer films have strong chemical resistivity, high temperature stability, and can be processed using several different methods such as extrusion molding or compression molding, which result in a wide range of film thicknesses. There are numerous types of polymer films that are available with different properties that support many types of grafted materials.

Surface modification is a method frequently employed to create polymer products designed for specific applications without altering the bulk material and can be achieved through several techniques. Dip coating and spin coating are frequently used empirical methods of surface modification, as well as plasma treatment where several activated species (electrons, ions, free radicals, and some neutral species) [Ma et al., 2012] are used to expose a surface of the polymer to a non-polymerizing plasma or by depositing a thin layer of plasma polymer on the surface of the polymer [Yasuda, 1977]. Surface modification via the covalent reaction of small molecules is another method used with increasing frequency. By either creating or utilizing existing surface functionality of the polymer, the surface functional groups can be covalently altered [Zhang et al., 2006]. Using surface modification techniques results in customized surface chemistry tailored for specific applications. The surface composition of the polymer affects the interactions the polymer has with its environment and subsequently, the suitable applications which are unique to each surface modified polymer. Surface modified polymers can be found in



a range of products from coatings, composites, adhesive tape, textiles [Scaffaro et al., 2011], and biomaterials [Pasparakis et al., 2010].

There has been extensive research into the grafting of materials onto and from polymer surface substrates. However, only a limited amount of research has investigated the grafting of end-functionalized polymers from a solid polymer surface [Walters and Hirt, 2006]. Polymer films can support the grafting of a range of molecules due to their versatile physical and chemical properties. Designing functional polymer films requires knowledge not only of molecular and chemical interactions of the film with the reacting substrates, but knowledge of the interactions the film will have with its environment. Factors such as functional group spacing, orientation, and reactivity with environmental factors are important factors to consider when designing a surface modified polymer film. With this understanding, polymer films can be designed to have a specific response to particular external stimuli. Grafting stimuli-responsive molecules, monomers, or polymers to the polymer films will result in a stimuli responsive polymer film, which can be affected by pH, temperature, radiation, magnetic field, or light, among others. The responses of polymers exist in a wide range such as a change in color, transparency, conductivity, shape (shape memory polymers), size, refractive index, crosslinking, and chain recombination, among other events [Lawandy, 1982]. Conjugated polymers are organic semiconductors [Lambeth, 2004] and have strong fluorescent properties, fluoresce a color in the visible spectrum, and can be used in a multitude of applications [Perepichka et al., 2006]. Light-sensitive polymer films that change color in response to irradiation are the application of interest in this study

The polymer film selected for this study was poly(ethylene-co-acrylic acid) (EAA), which contains carboxylic acid groups that can serve as reactive functional group

for grafting. EAA is a commonly used polymer film and available commercially. It is resistant to many organic solvents and is stable in most environmental conditions. After modification of the EAA films, 4'-(octyloxy)-4-biphenyl carboxylic acid (OBC), a polyphenylene class light-emitting chemical and 2,7-bis (bromomethyl)-9,9-dihexyl-9H-fluorene (BDMF), a polyfluorene class light-emitting chemical, are grafted onto the surface of the EAA film.

In order to graft OBC and BDMF onto the surface of the EAA film, the carboxylic acid groups of the neat EAA film will first undergo chemical modification. First, accessible carboxylic acid groups ( $-C=OOH$ ) on the film surface will be converted to acid chlorides ( $-C=OCl$ ) in order to allow for the quick and facile reaction of ethylene diamine which will form an amide ( $-C=ON-$ ) and leave a terminal primary amine ( $-NH_2$ ) group. The primary amines are stable and suitable for grafting OBC and BDMF. The end result is EAA film with the surface decorated with light-sensitive molecules that fluoresce in the visible spectrum. Figure 5.1 shows the chemical structures of OBC and BDMF. Prior to grafting, the carboxylic acid ( $-C=OOH$ ) group of OBC will be converted to acid chloride ( $-C=OCl$ ), similar to the first EAA film reaction step. The acid chloride of OBC and the bromine in BDMF can react with the primary amine available on the EAA film surface resulting is OBC and BDMF chemisorbed to the EAA file surface.

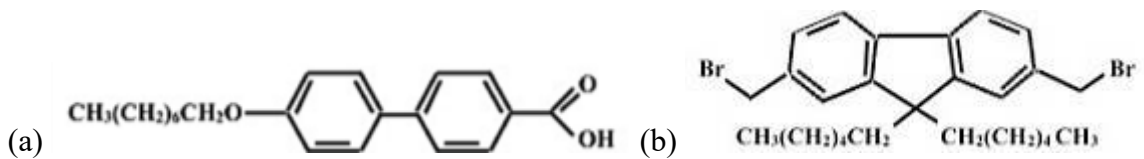


Figure 5.1 Chemical structures of OBC (a) and BDMF (b).

## 5.3 Materials and Methods

### 5.3.1 Materials

Poly(ethylene-co-acrylic) acid (EAA) film was extruded to an approximate thickness of 75  $\mu\text{m}$  from EAA Primacor 1410 (Dow Chemical Company, 9.5 wt% acrylic acid) by Sealed Air Corporation in Duncan, SC. Phosphorus pentachloride ( $\text{PCl}_5$ , 95%, CAS 10026-13-8), ethylenediamine ( $\text{CH}_2\text{Cl}_2$ , 99%, CAS 107-15-3), chlorobenzene (99%, CAS 108-90-7), and 2,7-bis (bromomethyl)-9,9-dihexyl-9H-fluorene (BDMF, 97%, CAS 187148-75-0) were purchased from Sigma Aldrich (St. Louis, MO, USA). Dichloromethane (99.9%, CAS 75-09-2) and 4'-(octyloxy)-4-biphenyl carboxylic acid (OBC, 99%, CAS 59748-18-4) were purchased from VWR (West Chester, PA, USA). HPLC grade water (Fisher Scientific, CAS 7732-18-5) and tetrahydrofuran (THF, Optima grade, 99.9%, CAS 109-99-9) were purchased from Fisher Scientific (Hampton, NH, USA). All chemicals were used as received.

### 5.3.2 FTIR Spectroscopy

Fourier Transform infrared spectroscopy was used to analyze the surface chemistry of the films. Spectra were collected using a Nicolet 6700 spectrometer (Thermo Electron Corporation) using Omnic software version 8.1.10 (Thermo Fisher Scientific 1992-2009). Attenuated Total Reflectance (ATR-FTIR) spectra were collected using a Pike Technologies Veemax II accessory with a 60° zinc selenide ( $\text{ZnSe}$ ) crystal and either a liquid nitrogen cooled MCT-A\* (mercury-cadmium-telluride) detector or a DTGS (deuterated triglycine sulfate) detector. A second method of ATR characterization was conducted using a MIRacle-ATR (Pike Technologies) with a  $\text{ZnSe}$ /diamond crystal. Films were also evaluated using transmission FTIR (T-FTIR) with a Thermo Electron

universal sample holder. Spectra of the light-sensitive chemicals were collected using the MIRacle-ATR.

### 5.3.3 Contact Angle Goniometry

Contact angle measurements were made using a Kruss Easydrop contact angle goniometer with a Teli CCD camera. Drops were 10  $\mu\text{L}$  in volume and dispensed using a 1 mL syringe with 1.85 mm inner diameter needles. The drops were formed at ambient temperature. A minimum of ten drops per sample was collected and analyzed using Drop Shape Analysis software (version 1.90.0.14). Contact angles were measured using the 'Tangent 2' method; the ten data points were averaged and 95% confidence intervals calculated.

## 5.4 Results and Discussion

The following section will illustrate the results and analysis of the methods used to confirm the reaction steps from the neat (unreacted) EAA film all the way through the final reaction steps of attaching the light-sensitive chemicals to the EAA films. The methods of analysis to be discussed include FTIR and contact angle goniometry.

### 5.4.1 Preliminary Reactions of EAA Film

In order to graft the light-sensitive chemicals onto the EAA film surface, the neat EAA film underwent two preliminary reactions (Figure 5.2). The first reaction is the conversion of the C=OOH in EAA to C=OCl groups [EAA-Cl]. EAA films ( $\sim 0.5\text{-}1\text{ in}^2$ ) were placed in a 0.03 g/mL  $\text{PCl}_5/\text{CH}_2\text{Cl}_2$  solution for 45 min at room temperature. The films were rinsed three times in clean  $\text{CH}_2\text{Cl}_2$  and vacuum dried before proceeding to the next step. After rinsing and drying, the films were then converted to EAA-NH<sub>2</sub> (-C=OCl  $\rightarrow$  -C=ONHCH<sub>2</sub>CH<sub>2</sub>NH<sub>2</sub>) by sonication for 24 h in a 0.0025-g/mL

ethylenediamine/HPLC water solution [Walters and Hirt, 2006]. The films were rinsed in clean HPLC water three times and vacuum dried before proceeding any further. The completion of the reactions was confirmed using ATR-FTIR.

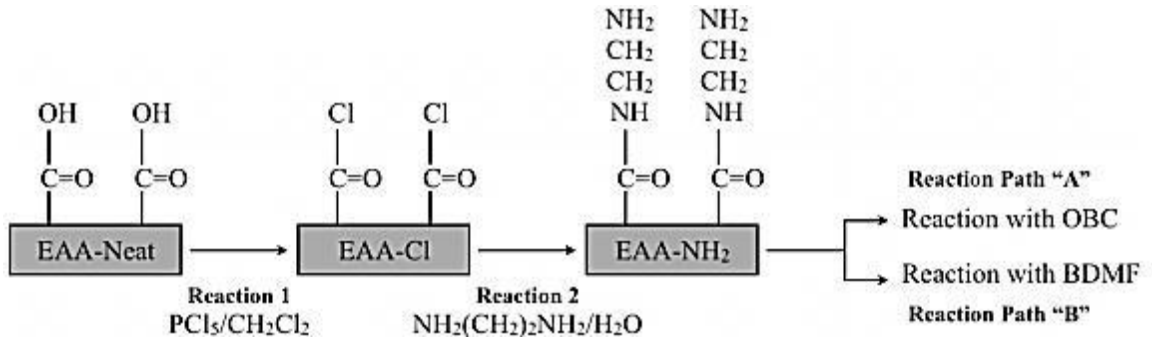


Figure 5.2 Reaction schematic of the preliminary reaction steps of EAA prior to reactions with light-sensitive chemicals.

Spectra were collected for neat (unreacted) EAA, EAA-Cl, and EAA-NH<sub>2</sub> (Figure 5.3).

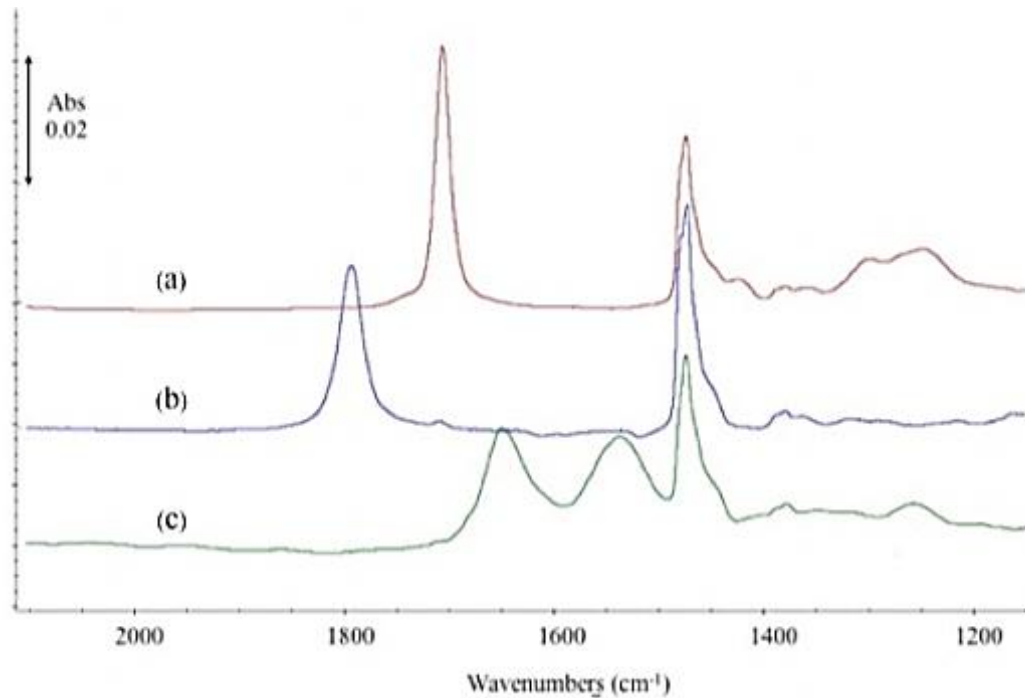


Figure 5.3 ATR-FTIR spectra of preliminary film reactions steps: (a) EAA-Neat, (b) EAA-Cl, (c) and EAA-NH<sub>2</sub>.

The ATR-FTIR spectrum for neat EAA film is shown in Figure 5.3a. The peak at  $\sim 1700\text{ cm}^{-1}$  corresponds to the carbonyl stretch of carboxylic acid. In the spectrum for EAA-Cl (Figure 5.3b) the carbonyl peak has shifted to  $\sim 1795\text{ cm}^{-1}$  demonstrating that the carboxylic acid was converted to acid chloride [Bruno and Svoronos, 2006; Silverstein and Webster, 1998]. Once EAA-Cl is reacted with ethylenediamine to form EAA-NH<sub>2</sub>, the acid chloride is converted to an amide. As can be seen in Figure 5.3c, the spectrum for EAA-NH<sub>2</sub> does not contain peaks corresponding to the carbonyl of the carboxylic acid or acid chloride. Instead, two peaks can be easily identified at  $\sim 1640\text{ cm}^{-1}$  and  $\sim 1530\text{ cm}^{-1}$  that are associated with amide II bonds [Bruno and Svoronos, 2006; Silverstein and Webster, 1998; Pretsch et al., 2000] indicating the successful conversion of the acid chloride groups to the amide groups.

It is important to note the presence of a peak common to all spectra, regardless of the reaction step of the film. The peak occurs at  $\sim 1465\text{ cm}^{-1}$  and corresponds to the -C-C- scissor bond of the polyethylene repeat unit [Pretsch et al., 2000].

## 5.4.2 Primary Reactions of EAA Films

### 5.4.2.1 Reaction Path “A”: Grafting of OBC

EAA-NH<sub>2</sub> film was reacted in a solution of 4'-(octyloxy)-4-biphenyl carboxylic acid (OBC) in a 2:1 molar ratio with PCl<sub>5</sub> (both in stoichiometric excess) in THF for 72 h at 60 °C. PCl<sub>5</sub> was present in the solution to convert the carboxylic acid of the end-functionalized OBC chemical to an acid chloride to aid in the grafting of OBC to the EAA-NH<sub>2</sub> film (Figure 5.4). After completion of the reaction, the films were rinsed in clean THF three times and vacuum dried. Figure 5.5 illustrates the grafting of OBC onto the EAA-NH<sub>2</sub> film surface.

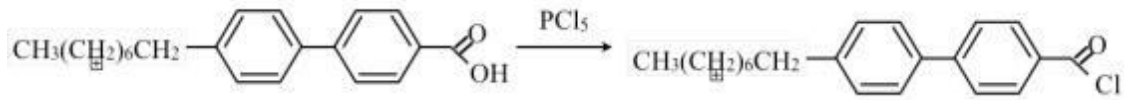


Figure 5.4 Conversion of carboxylic acid of OBC chemical to acid chloride

After completion of the reaction, the films were rinsed in clean THF three times and vacuum dried. Figure 5.5 illustrates the grafting of OBC onto the EAA-NH<sub>2</sub> film surface.

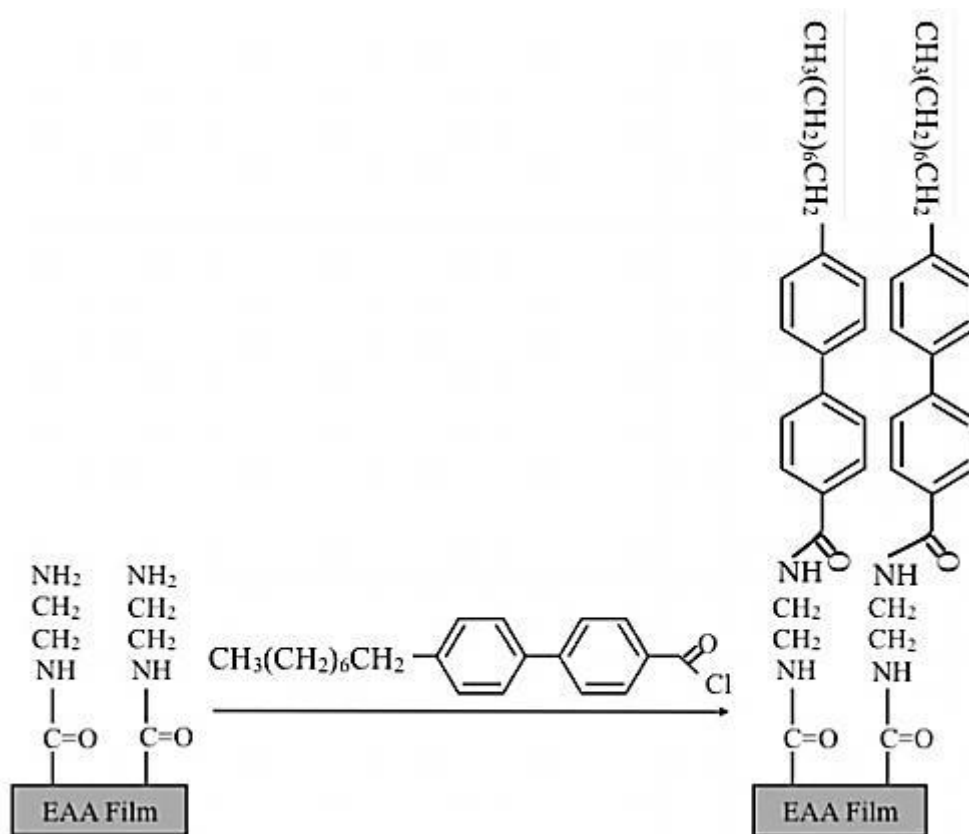


Figure 5.5 Reaction schematic of the reaction steps of EAA-NH<sub>2</sub> with acid chloride converted OBC chemical to EAA-OBC.

The grafting reaction of OBC onto the EAA film was confirmed using ATR-FTIR and contact angle. Figure 5.6 shows the ATR-FTIR spectra for the complete reaction process: EAA-Neat, EAA-Cl, EAA-NH<sub>2</sub> and EAA-OBC.

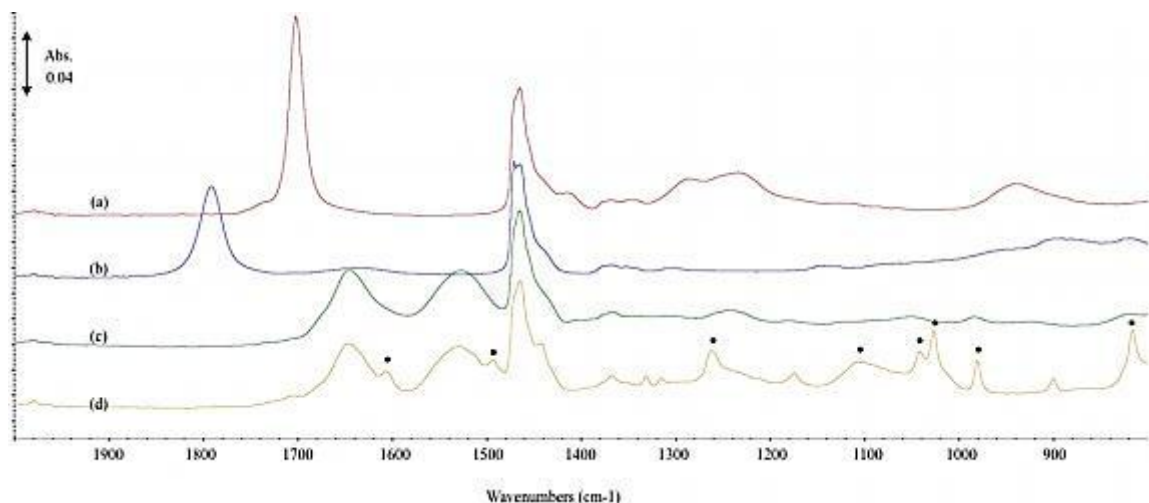


Figure 5.6 ATR-FTIR spectra of preliminary film reactions steps: EAA-Neat (a), EAA-Cl (b), EAA-NH<sub>2</sub> (c), and EAA-OBC (d).

Comparing the spectra for EAA-NH<sub>2</sub> (Fig. 5.6c) and EAA-OBC (Fig. 5.6d), it is easily seen that there are several notable differences in the spectra for these samples indicating that OBC grafted onto the film surface. From the EAA-OBC spectrum, there are three peaks of interest that can be used to validate the presence of OBC on the surface of the film. From left, a peak at  $\sim 1263\text{ cm}^{-1}$  indicates the C-N in plane bending of a secondary amide [Bruno and Svoronos, 2006] that is present at the end of the molecule that bonds to the -NH<sub>2</sub> of EAA-NH<sub>2</sub>. The two peaks to the right at  $\sim 1100\text{ cm}^{-1}$  and  $\sim 1025\text{ cm}^{-1}$  are indicative of the 1-4 disubstituted benzene ring [Silverstein and Webster, 1998]. Having two peaks in this region confirms this. Also, in the region of  $1300\text{--}1100\text{ cm}^{-1}$ , where two peaks are present, peaks corresponding to in-plane aromatic bending occur [Silverstein and Webster, 1998].

Figure 5.7 depicts a comparison of the spectrum of EAA-OBC with the spectrum of the OBC chemical. The peaks of interest are boxed around both spectra, demonstrating the peaks used to confirm the OBC presence on the surface of EAA-OBC correspond to the OBC chemical.



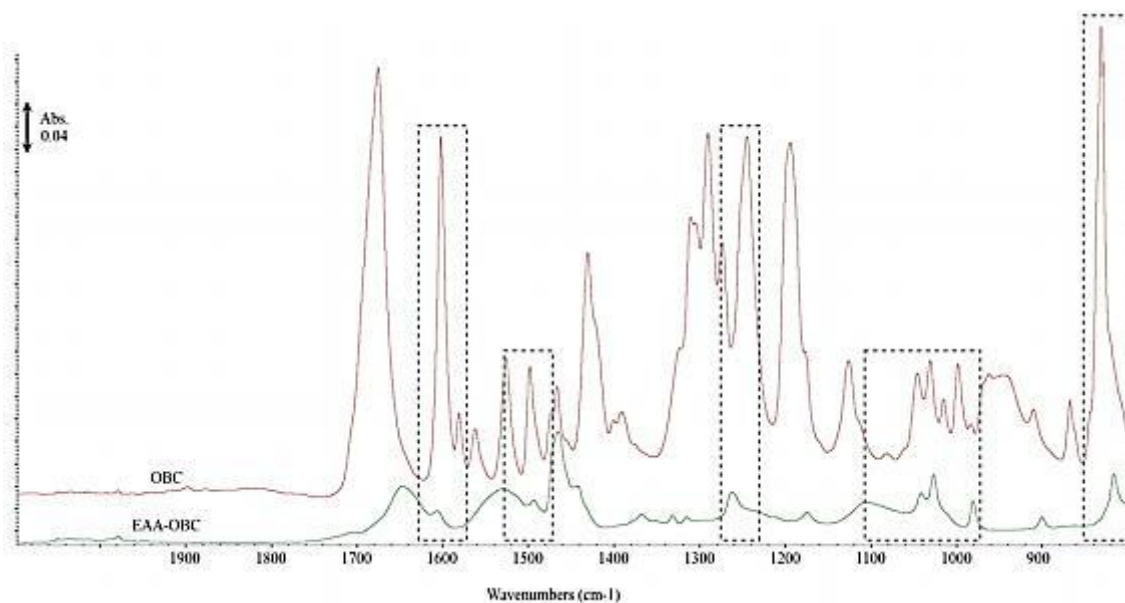


Figure 5.7 FTIR spectral comparison of OBC chemical and EAA-OBC reacted film. The peaks used to identify OBC on the surface of EAA-OBC are boxed around both spectra.

#### 5.4.2.2 Reaction Path “B”: Grafting of BDMF

EAA-NH<sub>2</sub> film was reacted in a 5 mM solution of 2,7-bis (bromomethyl)-9,9-dihexyl-9H-fluorene (BDMF) in chlorobenzene at 60 °C for 48 h. After the reaction was complete, the films were rinsed three times in clean chlorobenzene and vacuum dried.

Figure 5.8 illustrates the grafting of BDMF onto the EAA-NH<sub>2</sub> film. The steps to convert EAA film to EAA-NH<sub>2</sub> are the same as discussed previously.

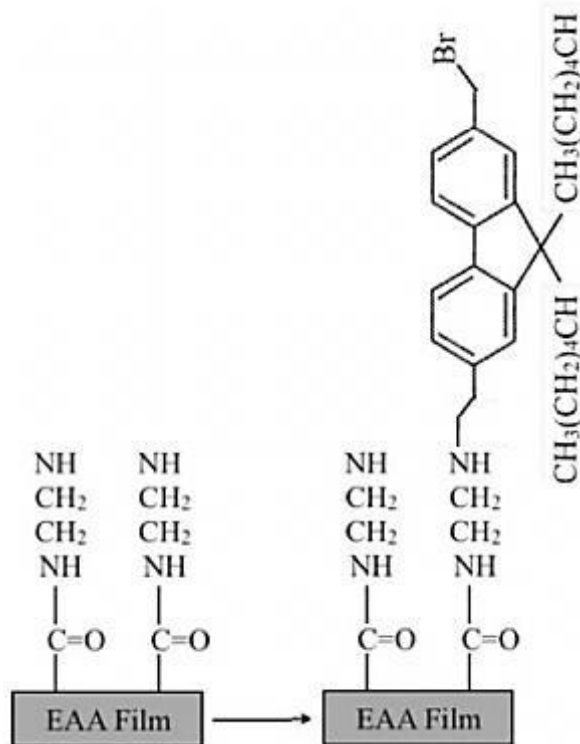


Figure 5.8 Reaction schematic of the reaction steps of EAA-NH<sub>2</sub> with BDMF chemical to form EAA-BDMF.

In comparing the spectra of EAA-NH<sub>2</sub> and EAA-BDMF (Figure 5.9), BDMF was grafted onto the film surface. The peak shoulder at  $\sim 1604\text{ cm}^{-1}$  corresponds to a conjugated C=C bond, as is present in the benzene ring of BDMF [Bruno and Svoronos, 2006; Silverstein and Webster, 1998; Kuptsov and Zhizhin, 1988]. Two peaks in the  $\sim 1025\text{-}1050\text{ cm}^{-1}$  range at  $1041\text{ cm}^{-1}$  and  $1027\text{ cm}^{-1}$  (peak maxima 0.026 and 0.022, respectively) correspond to C-H bending of a secondary amine and a 1-4 disubstituted benzene ring, respectively [Bruno and Svoronos, 2006; Silverstein and Webster, 1998]. The peak at  $\sim 975\text{ cm}^{-1}$  (peak maxima 0.0207) corresponds to C-H aromatic in-plane bending [Kuptsov and Zhizhin, 1988; Silverstein and Webster, 1998]. The peak at  $\sim 818\text{ cm}^{-1}$  (peak maxima 0.0253) corresponds to a 1,2,4-trisubstituted benzene ring, which is the exact substitution of the rings in the BDMF structure [Bruno and Svoronos, 2006].

The peaks at  $551\text{ cm}^{-1}$  and  $539\text{ cm}^{-1}$  (peak maxima 0.021 and 0.0166, respectively) correspond to C-Br stretch [Bruno and Svoronos, 2006; Silverstein and Webster, 1998; Kuptsov and Zhizhin, 1988; Pretsch et al., 2000]].

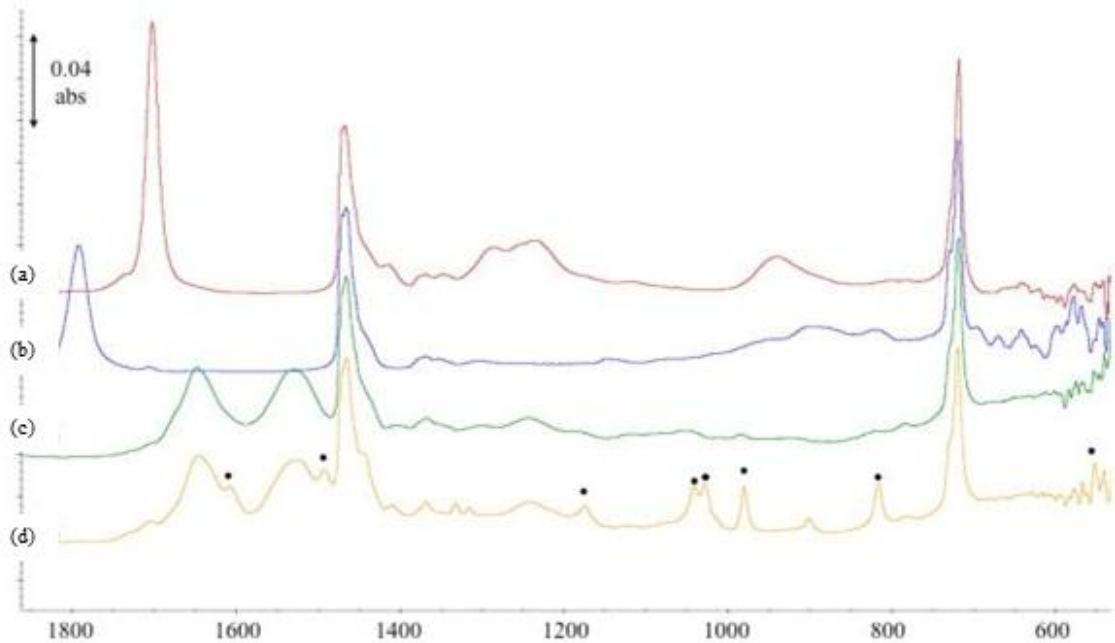


Figure 5.9 ATR-FTIR spectra of preliminary film reactions steps: EAA-Neat (a), EAA-Cl (b), EAA-NH<sub>2</sub> (c), and EAA-BDMF (d).

For comparison purposes, the spectrum of EAA-BDMF is compared to the spectrum of the BDMF chemical in Figure 5.10. The peaks of interest are boxed around both spectra, demonstrating the peaks used to confirm the BDMF presence on the surface of EAA-BDMF do correspond to the BDMF chemical.

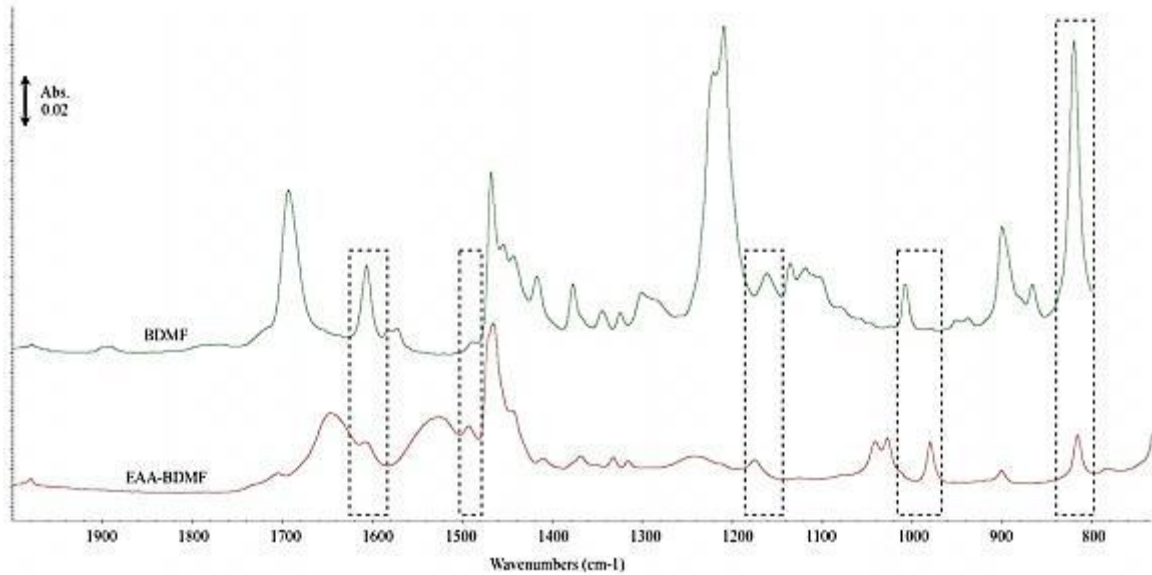


Figure 5.10 FTIR spectral comparison of BDMF chemical and EAA-BDMF reacted film. The peaks used to identify BDMF on the surface of EAA-BDMF are boxed around both spectra.

Another important feature of the films is seen using Transmission FTIR. Figure 5.11 shows a side-by-side comparison of the transmission spectra for EAA-Neat, EAA-Cl, EAA-NH<sub>2</sub>, EAA-OBC (on the left) and the preliminary spectra again on the right, this time with EAA-BDMF.

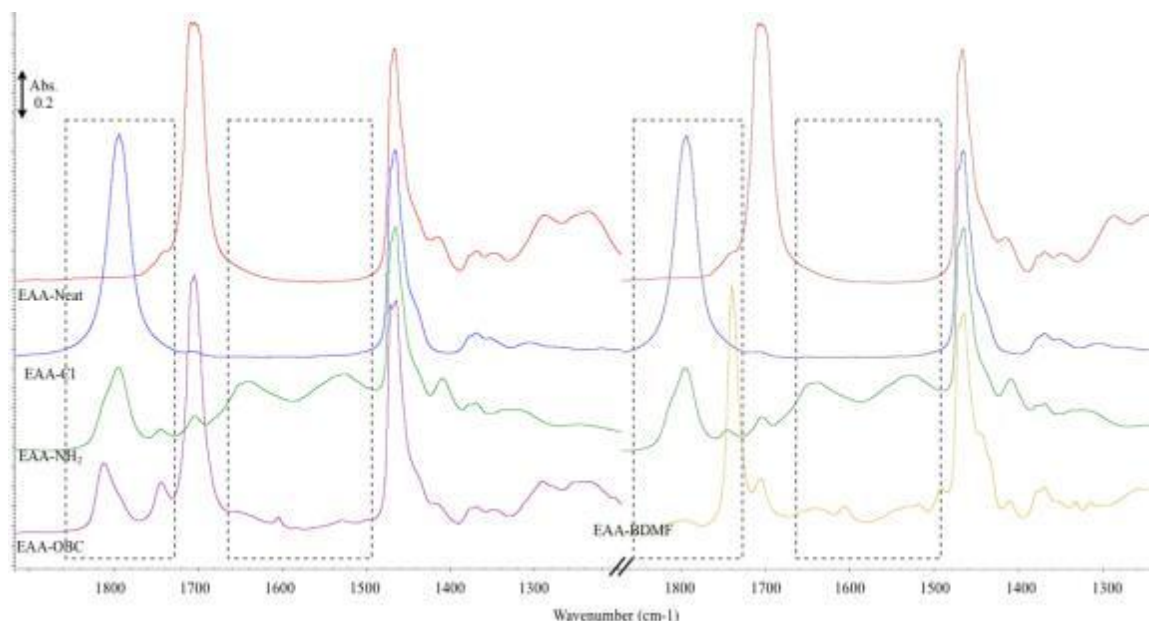


Figure 5.11 Transmission FTIR spectra of the preliminary step reaction films, as well as the final reaction products, EAA-OBC and EAA-BDMF.

Evaluating the transmission spectra for EAA-Neat, EAA-Cl, EAA-NH<sub>2</sub>, and EAA-OBC (on the left), particularly the peak at  $\sim 1795 \text{ cm}^{-1}$  (the peak associated with the conversion of the terminal  $\text{-OH}$  group to the acid chloride [EAA-Neat to EAA-Cl]), the appearance of this peak is first seen with the EAA-Cl spectrum, but unlike ATR-FTIR, this peak exists in the subsequent reaction step spectra as well. This is due to the penetration of the  $\text{-Cl}$  into the bulk of the film and reacting with interior  $\text{-OH}$  groups as well as the  $\text{-OH}$  groups present on the surface. With the ethylenediamine reaction, used to produce EAA-NH<sub>2</sub>, the peak lowers in intensity because the surface  $\text{-Cl}$  are converted to the terminal  $\text{-NH}_2$  group, but the peak is still present because the interior  $\text{-Cl}$  groups are still present. Comparing the EAA-NH<sub>2</sub> and the EAA-OBC film, the acid chloride peak is again still present because of the interior  $\text{-Cl}$  groups, while the peaks at  $\sim 1640 \text{ cm}^{-1}$  and  $\sim 1530 \text{ cm}^{-1}$  that are associated with amide II bonds of the EAA-NH<sub>2</sub> films are no longer present since the OBC chemical is grafted in place of the terminal  $\text{-NH}_2$ . This

sequence is also true for the BDMF reaction series, with the acid chloride peak appearing with the EAA-Cl film and remaining for the duration of the reaction series, as well as the appearance of the EAA-NH<sub>2</sub> amide II peaks and then the BDMF associated peaks replacing the terminal -NH<sub>2</sub> peaks.

### 5.4.3 Static Contact Angle Results

Static contact angle measurements were measured for the film samples after each reaction step. Since contact angle is sensitive to the outermost surface chemistry, it can be used to probe the efficacy of the reactions. Contact angle was determined using the Young Equation and uses a representative photo of a sessile drop is shown in Figure 5.12, which depicts the forces shown on a static contact angle drop. The gas (ambient air), liquid (HPLC water) and solid (EAA film) phases are in thermodynamic equilibrium. The parameters that relate to the balance of these forces are the interfacial tension between these three phases ( $\gamma_{SG}$  [solid-gas],  $\gamma_{SL}$  [solid-liquid],  $\gamma_{LG}$  [liquid-gas]) and the equilibrium contact angle,  $\theta$ .

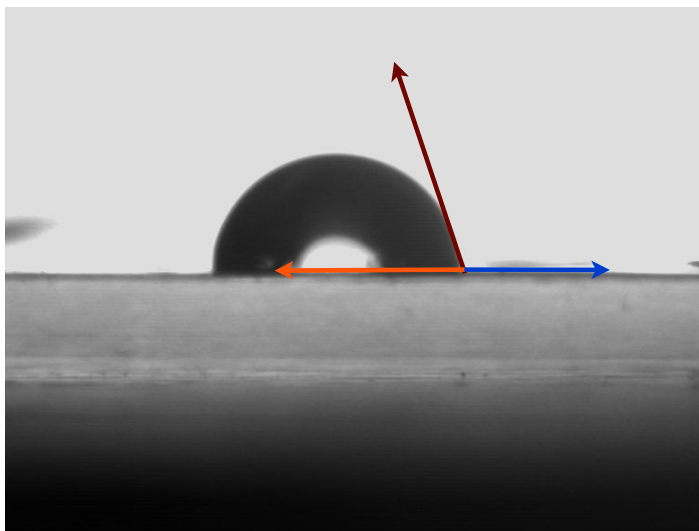


Figure 5.12 Representative image of a sessile droplet showing the intermolecular forces used to calculate the static contact angle.

Average static contact angles for each EAA film reaction step are given in Table 5.1. The measured water contact angle of neat EAA film was  $\sim 95.63^\circ \pm 1.05$ , which matches the range of contact angle values ( $87\text{-}99^\circ$ ) found in literature for EAA [Scaffaro et al., 2011; Janorkar et al., 2004]. The contact angle of EAA-Cl lowered only slightly to  $91.44^\circ \pm 1.98$ , similar to the findings of Scaffaro et al. [Scaffaro et al., 2011]. EAA-NH<sub>2</sub> had an average contact angle of  $72.47^\circ \pm 1.01$ , which is also in the range of observed static contact angle value of  $77^\circ$  [Luo et al., 2004].

Table 5.1 Summary of average contact angle values for surface-modified EAA films at each reaction step.

	Average CA	Std. Dev.	95% CI	Reference CA	Source of Reference CA
<b>EAA-Neat</b>	95.63	1.70	1.05	87-99	Scaffaro et al., 2011; Janorkar et al., 2004
<b>EAA-Cl</b>	91.44	2.02	1.98	Slightly lower value than EAA-Neat	Scaffaro et al., 2011
<b>EAA-NH<sub>2</sub></b>	72.47	1.55	1.01	77	Luo et al., 2004
<b>EAA-OBC</b>	80.50	2.40	1.49	77-85	Li and Marks, 2008
<b>EAA-BDMF</b>	85.17	0.50	0.56	82	Jhaveri et al., 2009

No known contact angle ranges were known for OBC or BDMF grafted films however, similar chemicals were found to have contact angle ranges close to those of the contact angle averages found in this study. EAA-OBC produced an average contact angle value of 80.25°, which is in the range of similar biphenyl-based molecules that had been grafted to siloxane functionalized quartz and had a contact angle range of 77-85° [Li and Marks, 2008]. EAA-BDMF had an average contact angle of 85.17°, which is close to 82°, the average contact angle value of another brominated fluorene molecule [Jhaveri et al., 2009].

Neat EAA was a hydrophobic solid, as was EAA-Cl. With the transition to EAA-NH<sub>2</sub>, the film became slightly hydrophilic (< 90°). The addition of either OBC or BDMF resulted in a slightly more hydrophobic film with the increased contact angles, even though the films were still considered in the hydrophilic range. Figures 5.13 and 5.14 illustrate the progression of contact angles between the reaction steps.





Figure 5.13 From left, EAA-Neat, EAA-Cl, EAA-NH<sub>2</sub>, and EAA-OBC static contact angle images.

It can be visually observed that the drop shape changes as the film becomes hydrophilic (EAA-NH<sub>2</sub>) and slightly more hydrophobic with either EAA-OBC or EAA-BDMF.



Figure 5.14 From left, EAA-Neat, EAA-Cl, EAA-NH<sub>2</sub>, and EAA-BDMF static contact angle images.

## 5.5 Conclusions

Based on the ATR-FTIR and static contact angle results, EAA films were modified to provide a terminal primary amine group that was then used to graft OBC and BDMF. FTIR analysis confirms the presence of the expected functional groups and also gives some indication to how the molecules may have reacted onto with films, such as the subsurface penetration of the -Cl molecule present for all subsequent reaction spectra. Contact angle measurements matched literature values and confirmed the preliminary reaction steps as well as supported that OBC and BDMF were successfully grafted to the EAA film surface.

## 5.6 References

- Bruno, Thomas J.; Svoronos, Paris D.N. CRC Handbook of Fundamental Spectroscopic Correlation Charts. Taylor and Francis: Boca Raton, FL, 2006, Figures 2.2, 2.4, and 2.7.
- Burillo, G.; Mendoza, R.; Fomine, S.; Ogawa, T. Grafting of Side Chain Liquid Crystal Monomers onto Polyethylene Film. *Polymer Bulletin*, 1997, 39, 489-494.
- Ma, Gui-qui; Liu, Ben; Li, Chen; Huang, Dinghai; Sheng, Jing. Plasma modification of polypropylene surfaces and its alloying with styrene *in situ*. *Applied Surface Science*, 2012, 258, 2424-2432.
- Ikada, Y.; Iwata, H. Mita, T.; Nagaoka, S. Grafting of Proteins onto Polymer Surfaces with the Use of Oxidized Starch. *Journal of Biomedical Materials Research* 1979, 13(3), 607-622.
- Janorkar, Amol V.; Luo, Ning.; Hirt, Douglas E. Surface Modification of an Ethylene-Acrylic Acid Copolymer Film: Grafting Amine Terminated Linear and Branched Architectures." *Langmuir* 2004, 20, 7151-7158.
- Jhaveri, S.; Peterson, J.; Carter, K. Poly (9,9-Dihexylfluorene) Layers Grown via Surface-Directed Ni(0) Condensation Polymerization. *Langmuir*, 2009, 25 (16), 9552-9556.
- Kupstov, A.H.; Zhizhin, G.N. Handbook of Fourier Transform Raman and Infrared Spectra of Polymers. Elsevier: New York, 1988, p. 7,11.
- Lambeth III, Robert H. Electroluminescence of conjugated aromatic polymers in organic light emitting diodes. 2004.  
[http://www.chemistry.illinois.edu/research/organic/seminar\\_extracts/2004\\_2005/2\\_Lambeth\\_Abstract\\_SP05.pdf](http://www.chemistry.illinois.edu/research/organic/seminar_extracts/2004_2005/2_Lambeth_Abstract_SP05.pdf) (Accessed Feb 25, 2012).
- Lawandy, S.N. Color Measurements for Detection of Radiation Damage in Polymers. *Elastomerics*, 1982, 33-35.
- Li, J.; Marks, T. Air-Stable, Cross-Linkable, Hole-Injecting/Transporting Interlayers for Improved Charge Injection in Organic Light-Emitting Diodes. *Chem. Mater.* 2008, 20, 4873-4882.
- Luo, Ning; Stewart, Michael J.; Hirt, Douglas E.; Husson, Scott M.; Schwark, Dwight W. Surface Modification of Ethylene-co-Acrylic Acid Copolymer Films: Addition of Amine Groups by Covalently Bonded Amino Acid Intermediates. *Journal of Applied Polymer Science*, 2004, 92 (3), 1688-1694.
- Pasparakis, George; Krasnogor, Natalio; Cronin, Leroy; Davis, Benjamin; Alexander, Cameron. Controlled polymer synthesis – from biomimicry towards synthetic biology. *Chemical Society Reviews*, 2010, 39, 286-300.

Perepitchka, Dmitrii F.; Perepichka, Igor F.; Meng Hong; Wudl, Fred. Light Emitting Polymers, *Organic Light-emitting Materials and Devices*, Marcel-Dekker Inc., CRC Press, 2006.

Pretsch, E.; Buhlmann, P.; Affolter, C. Structure of Determination of Organic Compounds, Tables of Spectral Data; Springer: New York, 2000; p. 246, 249, 262, 295-296.

Scaffaro, Robert.; Botta, Luigi.; Lo Re, Giada.; Bertani, Roberta.; Milani, Roberto.; Sassi, Alessandro. Surface modification of poly (ethylene-co-acrylic acid) with amino-functionalized silica nanoparticles. *Journals of Materials Chemistry*, 2011, 21, 3849.

Silverstein, R.M.; Webster, F.X. Spectrometric Identification of Organic Compounds; John Wiley & Sons Inc.: New Jersey, 1998, p. 84, 86, 90, 91, 99-102, 136.

Walters, Keisha B.; Hirt, Douglas E. Grafting of End-Functionalized Poly(*tert*-butyl acrylate) to Poly (ethylene-co-acrylic acid) film. *Polymer*, 2006, 47, 6567-6574.

Yasuda, H. Modification of polymers by plasma treatment and by plasma polymerization. *Radiation Physics and Chemistry*, 1977, 9, 805-817.

Zhang, Chun; Luo, Ning; Hirt, Douglas E. Surface grafting polyethylene glycol (PEG) onto poly(ethylene-co-acrylic acid) films. *Langmuir*, 2006, 22, 6851-6857.

CHAPTER VI  
OPTICAL PROPERTY CHARACTERIZATION OF EAA-OBC AND EAA-BDMF  
POLYMER FILMS

**6.1 Abstract**

Two light-emitting molecules, 4'-(octyloxy)-4-biphenyl carboxylic acid (OBC) and 2,7-bis (bromomethyl)-9,9-dihexyl-9H-fluorene (BDMF), were grafted to the surface of surface modified poly (ethylene co-acrylic acid) (EAA) films. Each reaction step was confirmed previously using attenuated total reflectance Fourier transform infrared spectroscopy (ATR-FTIR), X-ray photoelectron spectroscopy (XPS) and static contact angle. This data is available in Chapter 5. OBC and BDMF were chosen as the grafted molecules for their light sensitivity and use in further development of light-sensitive polymer films. These LEP surface grafted films were evaluated using UV-Vis spectrophotometry to determine the maximum UV absorption wavelengths. The films were then irradiated at the maximum absorption wavelengths in a fluorescence spectrophotometer and the emission wavelengths were found to be in the violet-blue and/or red regions of visible light. The films were then irradiated at 254 nm with a UV lamp to view the fluorescence of the films at all reaction stages. Both EAA-OBC and EAA-BDMF fluoresced in the blue region of visible light. The films were reevaluated after six months using MIRacle-ATR FTIR and fluorescence spectrophotometry. The FTIR results confirmed that the LBC and BDMF chemicals were still in tact on the

surface of the film, and fluorescence spectrophotometry confirmed the films still fluoresced in the blue and red regions of visible light.

## 6.2 Introduction

Light-sensitive polymers (LSPs) have experienced significant commercial success due to their wide range of applications. LSPs can be found in light-emitting diodes (LEDs) since they are capable of emitting light across the visible, ultraviolet and infrared wavelengths. They can also be seen in quantum dots, liquid crystal display televisions, and light bulbs, among many more applications [Perepichka et al., 2006].

LSPs are also frequently used in the detection of radiation. They are widely adaptable to various phases used in radiation detection dosimeters, including films [Cheung et al., 2007] or polymer gels [Mori et al., 2005]. Typically, radiation detectors have the light-emitting chemical grafted onto the surface for films [Cheung et al., 2007; Walters and Hirt, 2006; Zhao et al., 2009] or are contained within the gel [Mori et al., 2005] and change color or another property that is easily monitored for changes with radiation exposure.

The method of grafting light-emitting chemicals to a polymer substrate to act as a detection device has limited investigative studies. Due to the accessibility of commercially manufactured polymers, poly(ethylene-co-acrylic acid) (EAA) was chosen as the polymer substrate. EAA has bulk properties that make it useful for a wide range of applications and contains reactive acid groups that can serve as the grafting sites for the light-emitting chemicals.

Light-emitting polymers can fall into a wide variety of classifications.

Polyphenylenes and polyfluorenes are two classes of light-emitting polymers (LEPs)

selected for use in this research. Polyphenylenes exhibit strong fluorescence in either the blue or red visible light regions, depending on the dendrimer orientation [Liu et al., 2003] or functional groups [Imai et al., 2003] that are attached to the main structure.

Polyfluorenes typically exhibit fluorescence in the blue visible light region [Perepichka et al., 2006; Zhao et al., 2009; Yu et al., 2001]. The chemical structures of the two light-emitting polymers selected for use in this research, 4'-(octyloxy)-4-biphenyl carboxylic acid (OBC), which is a polyphenylene, and 2,7-bis (bromomethyl)-9,9-dihexyl-9H-fluorene (BDMF), a polyfluorene, are shown in Figure 6.1.

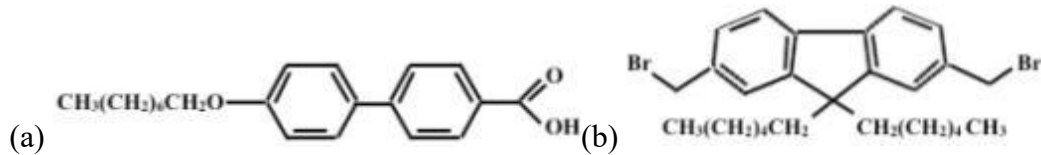


Figure 6.1 Chemical structures of OBC (a) and BDMF (b).

When evaluating light-emitting materials for their fluorescence properties, the emission wavelengths are compared to the visible spectrum to determine the color of fluorescence in the region of visible light. Figure 6.2 shows the wavelength range of visible light in the visible spectrum. Based on what can be seen in the visible spectrum, for EAA film grafted with OBC or BDMF to emit in the blue visible light range, the emission wavelength must fall in the 450-475 nm range. To fluoresce red, the films must emit in the range of 620-750 nm [Madigan 2011].

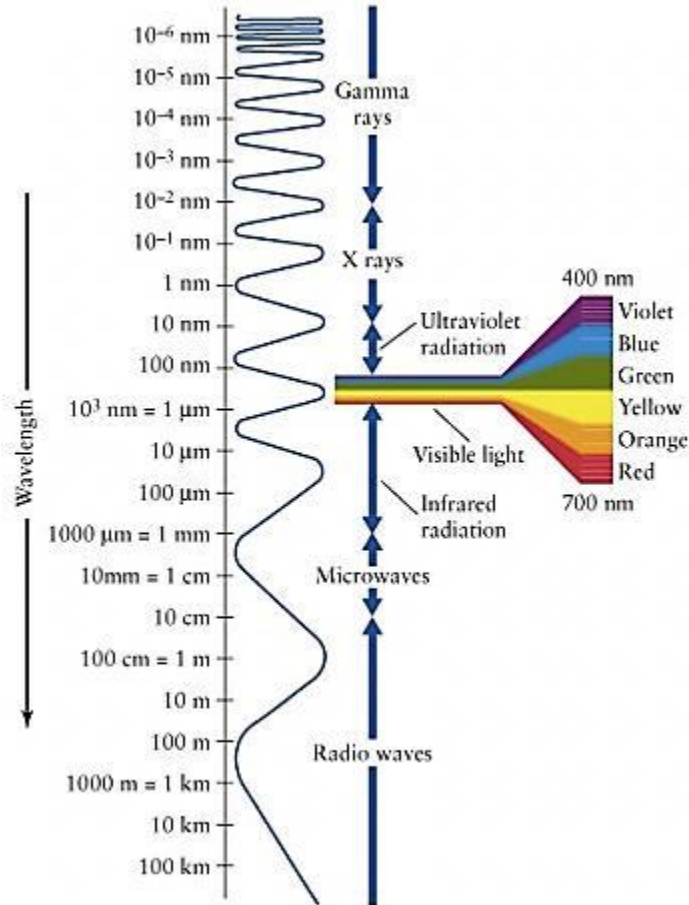


Figure 6.2 Visible spectrum with wavelengths for each color range [Madigan, 2011].

## 6.3 Materials and Methods

### 6.3.1 Materials

The poly(ethylene co-acrylic) acid (EAA) film had an approximate thickness of 75  $\mu$ m and was extruded from EAA Primacor 1410 (9.5 wt% acrylic acid) pellets (Dow Chemical Company) by Sealed Air Corporation in Duncan, SC. Phosphorus pentachloride ( $\text{PCl}_5$ , 95%, CAS 10026-13-8), ethylenediamine ( $\text{CH}_2\text{Cl}_2$ , 99%, CAS 107-15-3), chlorobenzene (99%, CAS 108-90-7), and 2,7-bis(bromomethyl)-9,9-dihexyl-9H-fluorene (BDMF, 97%, CAS 187148-75-0) were purchased from Sigma Aldrich (St. Louis, MO, USA). Dichloromethane (99.9%, CAS 75-09-2) and 4'-(octyloxy)-4-biphenyl

carboxylic acid (OBC, 97%, CAS 59748-18-4) were purchased from VWR (West Chester, PA, USA). HPLC water (HPLC grade, Fisher Scientific, CAS 7732-18-5) and tetrahydrofuran (THF, Optima grade, 99.9%, CAS 109-99-9) were purchased from Fisher Scientific (Hampton, NH, USA). All chemicals were used as received.

## **6.3.2 Methods**

### **6.3.2.1 UV-Vis Spectroscopy**

UV-Vis spectroscopy was collected using a Shimadzu UV-2550 V2.33 UV-Vis spectrophotometer. The software used to collect and analyze data was UV Probe (Shimadzu, version 2.33). The sample cell temperature was maintained at 25° C and the data collection range was 900-200 nm, to cover the near infrared and ultraviolet wavelength range.

### **6.3.2.2 Fluorescence Spectroscopy**

Fluorescence spectroscopy data was collected using a Horiba Jobin Yvon Fluoromax-4 spectrofluorometer. Samples were irradiated at wavelengths of 264 nm and 290 nm. Data was collected and analyzed using FluorEssence software (Horiba Jobin Yvon, version 3.5.1.20).

### **6.3.2.3 UV Lamp Illumination**

The films were irradiated using a 6-Watt UltraViolet Products handheld UV lamp with wavelength options of 254 nm or 365 nm.

### **6.3.2.4 FTIR Spectroscopy**

Fourier Transform infrared spectroscopy was used to analyze the surface chemistry of the films. Spectra were collected using a Nicolet 6700 spectrometer



(Thermo Electron Corporation) using Omnic software version 8.1.10 (Thermo Fisher Scientific 1992-2009). A MIRacle-ATR (Pike Technologies) with a ZnSe/diamond crystal and a liquid nitrogen cooled MCT-A\* (mercury-cadmium-telluride) detector.

## 6.4 Results and Discussion

### 6.4.1 UV-Vis Spectroscopy

Once the grafting of LEPs onto the EAA film surface was confirmed [see Chapter 5], these LSP-modified films can be evaluated for their fluorescent properties. The first step was to determine at what wavelengths the films absorbed UV light. Using the UV-Vis spectrophotometer, samples were irradiated and data evaluated for peaks in the absorption spectra. Figure 6.3 shows the UV-Vis spectrum for EAA-Neat, EAA-Cl, EAA-NH<sub>2</sub>, and EAA-OBC films. It can be seen in the spectra that EAA-OBC contains a peak that none of the other films possess. This peak is at a maximum at  $\lambda_{MAX} \sim 290$  nm.

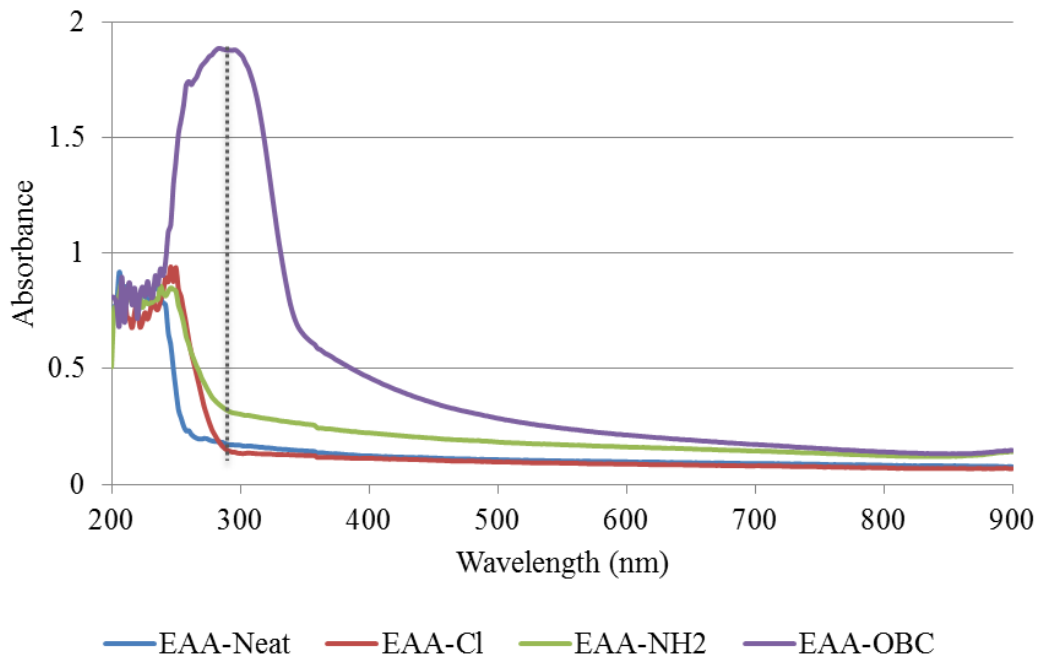


Figure 6.3 UV-Vis spectra for EAA-Neat, EAA-Cl, EAA-NH<sub>2</sub>, and EAA-OBC.

The UV-Vis spectra for EAA-Neat, EAA-Cl, EAA-NH<sub>2</sub>, and EAA-BDMF are shown in Figure 6.4. Similar to EAA-OBC, a peak unique to EAA-BDMF can clearly be seen in the UV-Vis spectrum. The peak for the EAA-BDMF film reaches a maximum absorbance at  $\lambda_{MAX} \sim 264$  nm with a shoulder at  $\lambda \sim 320$  nm.

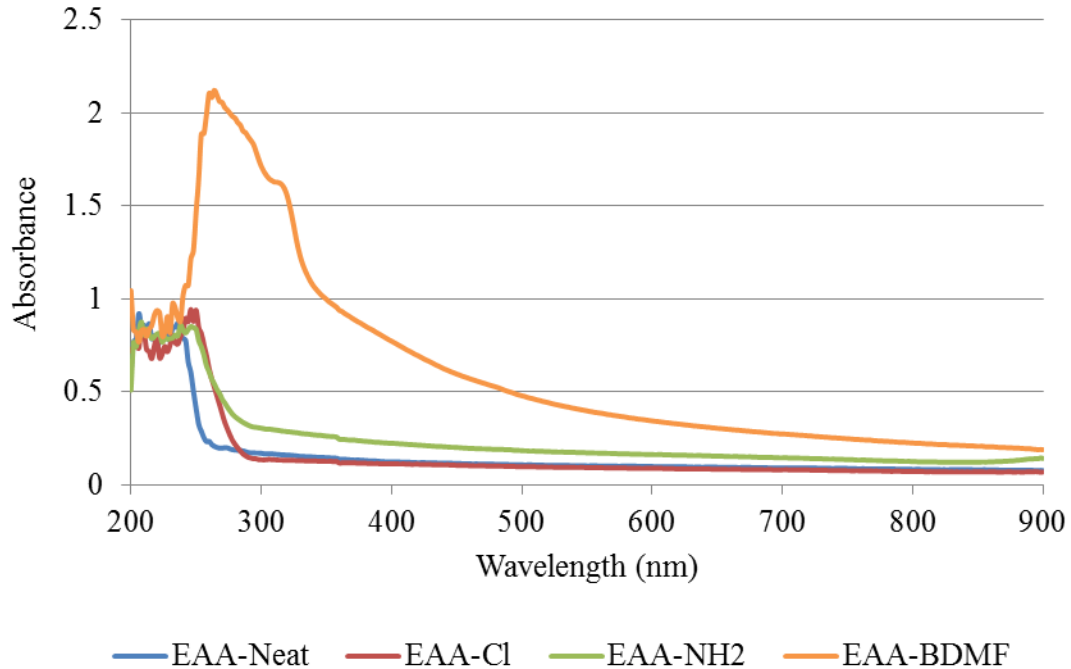


Figure 6.4 UV-Vis spectra for EAA-Neat, EAA-Cl, EAA-NH<sub>2</sub>, and EAA-BDMF.

### 6.4.2 Fluorescence Spectroscopy

Using the absorbance maxima wavelengths seen in the UV-Vis spectrophotometry spectra, the films were next irradiated with UV light in a fluorescence spectrophotometer to determine the wavelengths at which the films fluoresce. Since the films had absorbance maxima values of  $\sim 264$  nm and  $\sim 290$  nm, all the films were irradiated at both wavelengths. Figure 6.5 shows the fluorescence spectrophotometry (FS) spectra of EAA-Neat, EAA-Cl, EAA-NH<sub>2</sub> and EAA-OBC. The EAA-Neat, EAA-Cl, EAA-NH<sub>2</sub> spectra are shown for  $\sim 290$  nm, since that wavelength corresponded to the

absorbance maximum seen for EAA-OBC. The spectra of both 264 nm and 290 nm are shown for EAA-OBC.

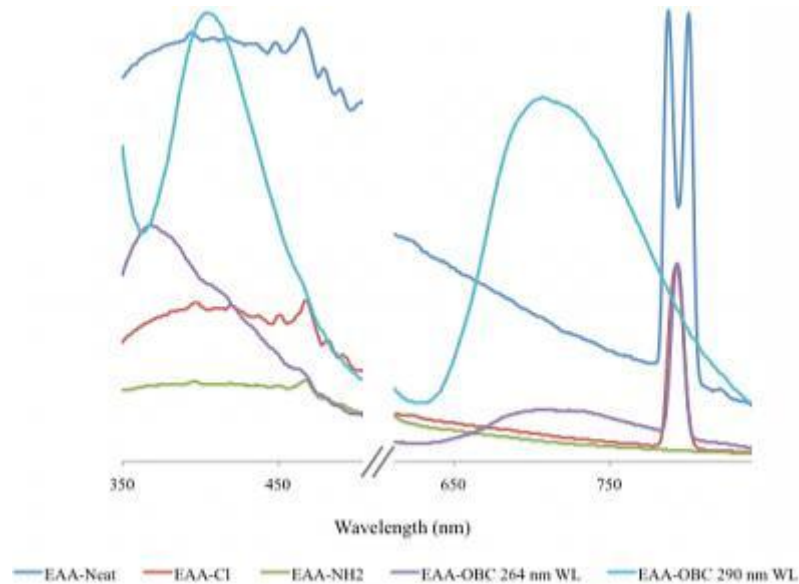


Figure 6.5 FS spectra for EAA-Neat, EAA-Cl, EAA-NH<sub>2</sub>, and EAA-OBC.

Examining the spectra, EAA-OBC spectra each have two peaks that indicate fluorescence in the visible region for both wavelengths at which the film was irradiated. A peak can be seen in the EAA-OBC-264 nm spectrum at a wavelength of ~365 nm. A nearby peak can be seen at ~410 nm for the EAA-OBC-290 nm spectrum. Emission in this region would fluoresce in the violet-blue region of visible light. There is also a significant peak at ~700 nm, which corresponds to a fluorescence in the red region of visible light. While the peak exists in both EAA-OBC spectra, the EAA-OBC-290 nm spectrum has a peak of much higher intensity in comparison to the EAA-OBC-264 nm spectrum. This is due to the fact that the absorbance maximum for the EAA-OBC film was at 290 nm and not 264 nm, which would result in stronger fluorescence at the 290 nm wavelength.

The FS spectra for EAA-Neat, EAA-Cl, EAA-NH<sub>2</sub>, and EAA-BDMF can be seen in Figure 6.6. Like with the FS spectra for EAA-OBC, the EAA-Neat, EAA-Cl, EAA-NH<sub>2</sub> spectra are shown for ~264 nm, since that wavelength corresponded to the absorbance maximum seen for EAA-BDMF. The spectra for both absorbance wavelengths are shown for EAA-BDMF.

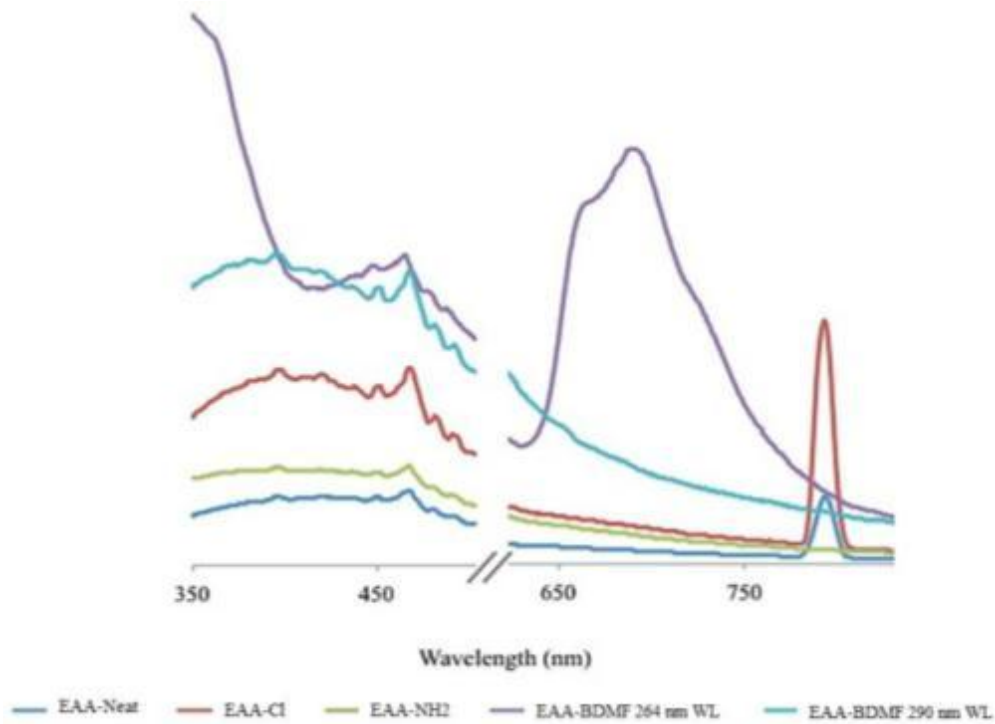


Figure 6.6 FS spectra for EAA-Neat, EAA-Cl, EAA-NH<sub>2</sub>, and EAA-BDMF.

Two peaks of interest can be seen in the EAA-BDMF FS spectra that indicate fluorescence in the visible region for both irradiated wavelengths. The left peak can be seen in the both the EAA-BDMF-264 nm and EAA-BDMF-290 nm spectra at a wavelength of ~460 nm. While not an intense peak, it corresponds to emission in the violet-blue region of visible light. There is a significant peak at ~700 nm in the EAA-BDMF-264 nm spectrum, which corresponds to a fluorescence in the red region of visible

light. This peak does not appear in the EAA-BDMF-290 nm spectrum due to the fact that the absorbance maximum for the EAA-BDMF film was at 264 nm and not 290 nm. Florescence would have a stronger appearance at the 264 nm irradiation wavelength.

### 6.4.3 UV Lamp Illumination

Since the films have been shown to fluoresce using analytical techniques, the next step was to place the films at all stages of film modification and surface grafting under a UV lamp and observe for film fluorescence. The films were placed in a glass UV-transparent petri dish and irradiated at  $\lambda=254$  nm. Unfortunately, the limitations of the UV lamp only allowed for irradiation at a single UV wavelength. The films prior to irradiation and the irradiated films can be seen in Figure 6.7. The physical appearance of the films did not change after irradiation.

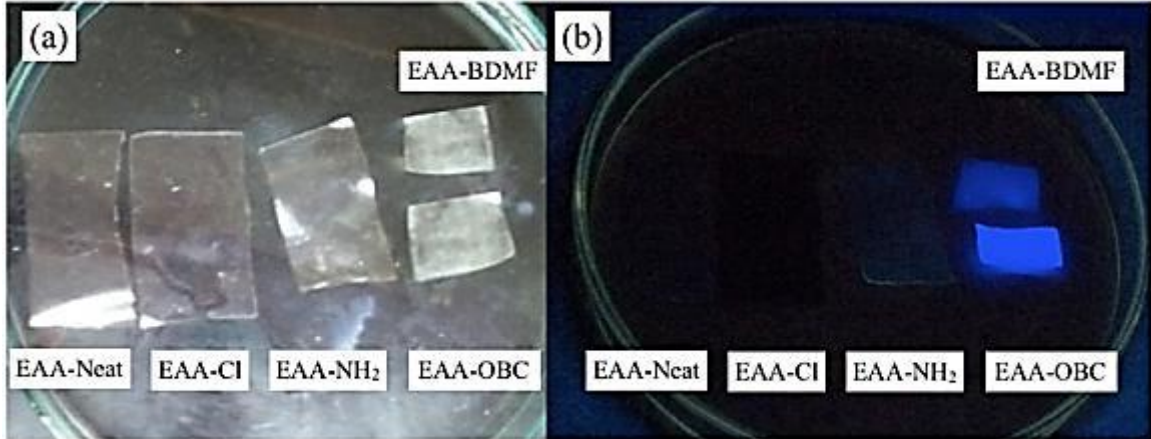


Figure 6.7 Films prior to UV irradiation (a) and during irradiation (b).

Observing Figure 6.7, it is clear that the grafting of the OBC and BDMF chemicals caused the EAA films to fluoresce. The films did not emit visible light at any reaction step prior to the light-sensitive chemicals being grafted to the surface-modified EAA films. While it was expected that EAA-BDMF would have a more intense

fluorescence at 254 nm due to the absorbance maxima of EAA-BDMF occurring at 264 nm, EAA-OBC had a stronger fluorescence at that wavelength. Since BDMF is a bulkier molecule, it could be that OBC grafted to the EAA-NH<sub>2</sub> film at a higher surface density due to its more linear geometry.

#### 6.4.4 FTIR and Fluorescence Spectroscopy of 6 Month Old Films

The stability of the EAA-OBC and EAA-BDMF films is important for further development of the films and any future applications. The films were stored in a desiccator for six months, then brought out to re-examine the FTIR spectra to confirm the functional groups of the reacted films are still intact and the FS spectra to confirm the films will still fluoresce.

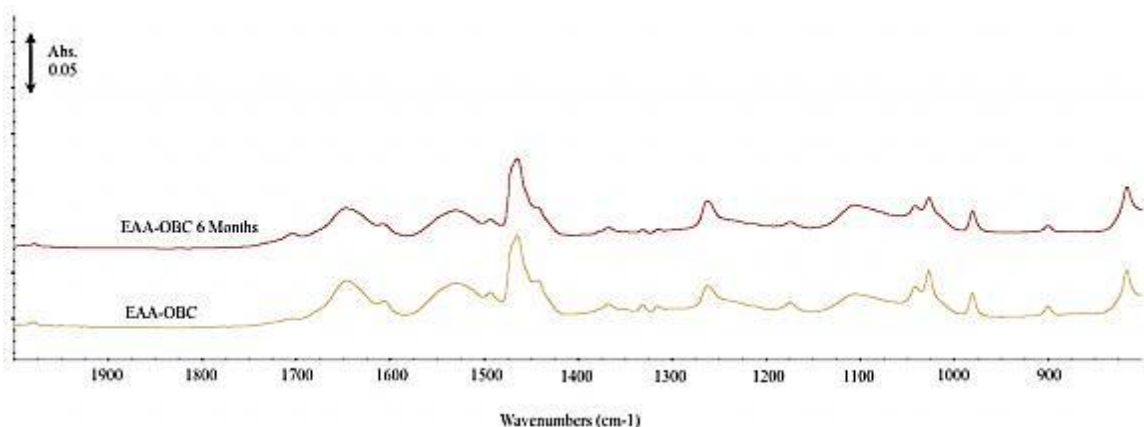


Figure 6.8 MIRacle-ATR FTIR spectral comparison of newly made EAA-OBC film with EAA-OBC film after 6 months.

A comparison of a newly made EAA-OBC film with the same film six months later is shown in Figure 6.8. From a visual inspection of the spectra, the spectra of the two films show no difference. To confirm the film was unchanged, the location of the peaks and the peak heights were also evaluated. The locations of the peaks of interest

remained unchanged after six months, however the peaks heights did have some changes. Comparing the six-month-old film to the newly made film, the peaks experienced both peak height increases and decreases. The maximum peak height increase was a 23.33 % increase at  $\sim 1108 \text{ cm}^{-1}$ . The maximum peak decrease was 27.03 % at  $\sim 1025 \text{ cm}^{-1}$ . The MIRacle-ATR data confirms the presence of the OBC chemical still intact after six months, and that the peaks only experienced slight changes in that time period.

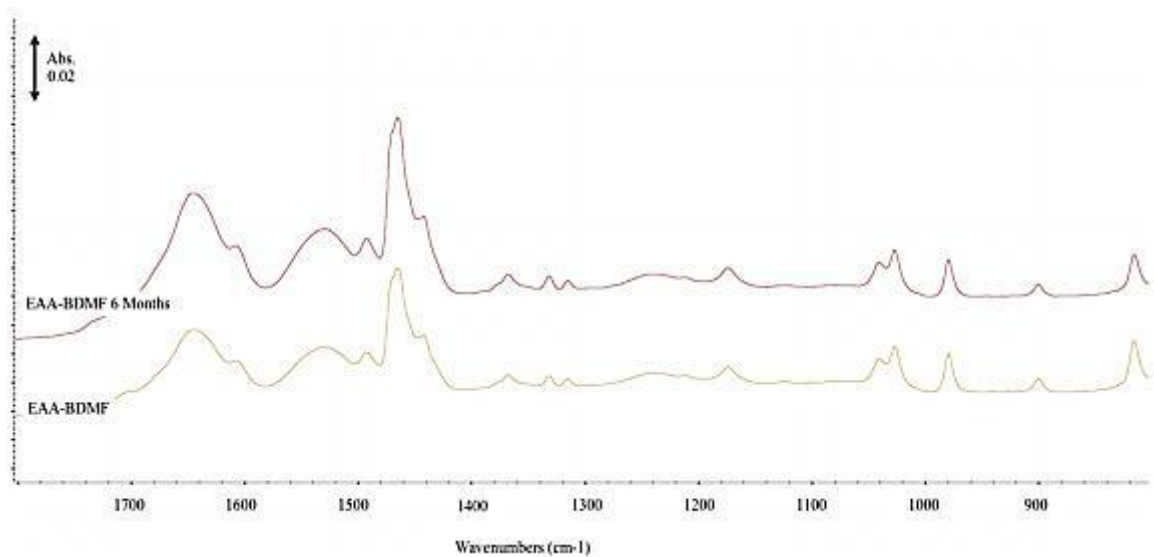


Figure 6.9 MIRacle ATR FTIR spectral comparison of newly made EAA-BDMF film with EAA-BDMF film after 6 months.

MIRacle-ATR spectra were also used to evaluate the EAA-BDMF film as a newly made film and after six months. Again, a visual inspection of the spectra reveals no apparent differences. The locations and peak heights of the peaks of interest were examined for any changes. The locations of the peaks experienced no changes, and the peak heights varied only slightly. The maximum peak height increase was 7.69% and occurred at  $\sim 1172 \text{ cm}^{-1}$ , and the maximum decrease in peak height happened at  $\sim 979 \text{ cm}^{-1}$ .

and was 3.85%. The MIRacle-ATR spectra confirmed that the light-sensitive chemicals were both intact for both films after a time period of six months.

Next, the films were evaluated using fluorescence spectroscopy for any changes in fluorescing activity. Figures 6.10 and 6.11 display the results of the FS spectra for the six-month-old films, as well as the spectra of the newly made films for comparison.

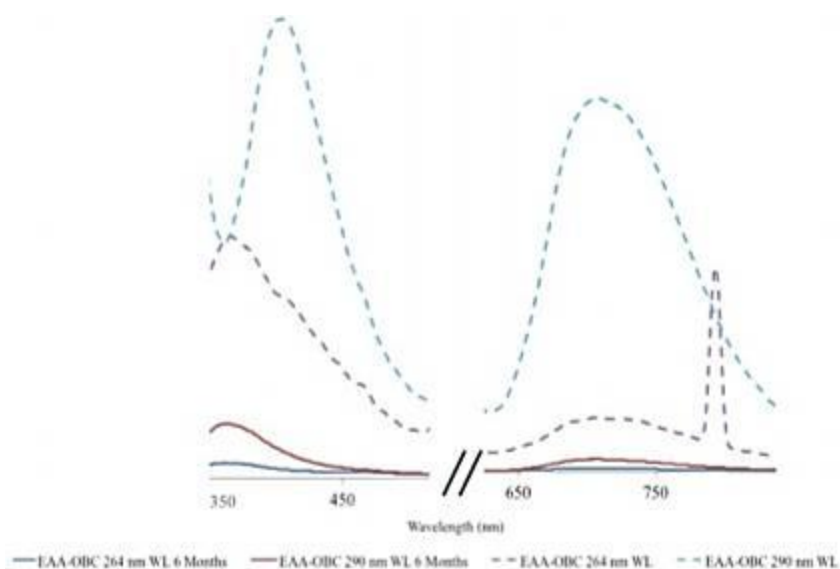


Figure 6.10 FS spectra of EAA-OBC film after six months and newly made EAA-OBC film for comparison.

The FS spectra for EAA-OBC reacted films are seen in Figure 6.10. The newly made films are shown as dashed lines for comparison to the film spectra of the six-month-old films. The films were again irradiated at two wavelengths, 264 nm and 290 nm. The aged films did produce peaks in the same locations as the newly made films, but the peak intensity was severely lower. However, this result does not indicate a degradation of the films after six months. The fluorescence spectrophotometer has an extremely small irradiating beam and can only collect spectra for a small spot of the film. Due to the availability of reactive groups from the neat film from which the films are



surface modified and subsequently reacted with the LS chemicals, only a small percentage of the film surface will contain the LS chemical groups. The beam may have collected spectra for an area of weak OBC presence. The important result from the FS data is that the film still fluoresces at the same wavelengths and therefore will emit in the blue and red regions of visible light.

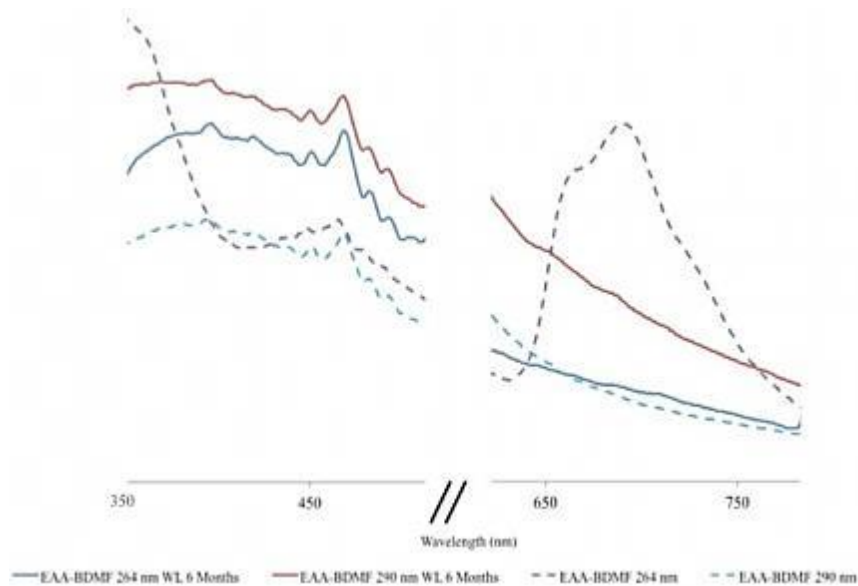


Figure 6.11 FS spectra of EAA-BDMF film after six months and newly made EAA-BDMF film for comparison.

The EAA-BDMF film produced different results than the EAA-OBC films after six months. It can be seen from Figure 6.11 that the FS spectra of EAA-BDMF aged film demonstrated an increase in intensity of the peak at ~460 nm; the exact opposite of the EAA-OBC results. This is yet another example of how the FS beam collects only a minimal area of sample surface for data analysis and the intensity of the peaks is not a complete indication of film fluorescence capabilities. The important fact of the existence of the peak is most valuable. However, the newly made film produced a strong peak at ~688 nm when irradiated at 264 nm. While the aged film at 264 nm did not produce a

distinct peak, the film did have moderate fluorescing activity in that region and is still expected to emit in the red region of visible light, along with the blue emission as indicated by the peak at  $\sim 460$  nm.

Lastly, the films were illuminated with a UV lamp at a wavelength of 254 nm, shown in Figure 6.12. Both films are clearly fluorescing in the blue region of visible light. The results from MIRacle-ATR FTIR, fluorescence spectroscopy and UV illumination indicate the presence of the LS chemicals on the surface of both films as well as confirm the fluorescing properties of the films remain after a period of six months.

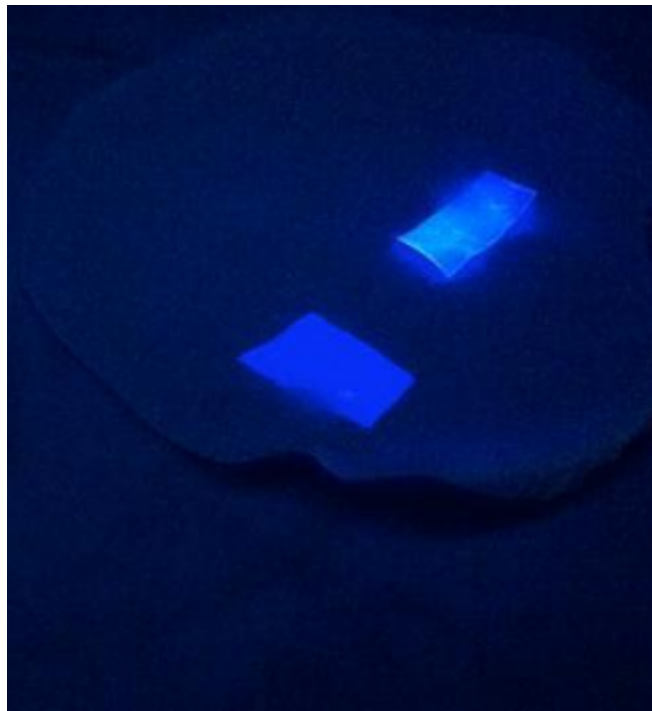


Figure 6.12 UV illumination of six month old EAA-BDMF (left) and EAA-OBC (right) at a wavelength of 254 nm.

## 6.5 Conclusions

The observed fluorescence of the EAA-OBC and EAA-BDMF samples demonstrates that grafting of OBC and BDMF to the surface-modified EAA films was successful. It was also shown that the activity of these light-sensitive chemicals was not significantly reduced by the use of the terminal functional groups in order to attach the molecules to the EAA films, as the conjugated structures remained intact. Absorbances of the films were measured using UV-Vis spectrophotometry. Using the absorbance maxima values from the UV-Vis data, the OBC- and BDMF-modified EAA films were irradiated at the absorbance maxima wavelengths. The fluorescence spectrophotometry results showed that the films would emit visible light in the violet-blue and/or red regions. Due to the promising data shown from these analytic techniques, the films were irradiated using a 254 nm UV lamp, and both films fluoresced strongly in the blue range of visible light. If films were irradiated at a higher wavelength, such as 700 nm where both films demonstrated emission peaks, it is expected that the films would also fluoresce red. The films were re-evaluated after six months using MIRacle-ATR FTIR, fluorescence spectrophotometry, and UV illumination, producing data that confirmed the presence of the OBC and BDMF chemicals still in tact on the surface of the films as well as spectra indicating the fluorescence stability of the films over an extended period of time and visible confirmation of fluorescing properties.

## 6.6 References

Imai, M.; Ikegami, M.; Momotake, A.; Nagahata, R.; Arai, T. Photoisomerization and Fluorescence Behavior of Polyphenylene-based Stilbene Dendrimers. *Photochem. Photobiol. Sci.* 2003, 2, 1181-1186.

Liu, D.; De Feyter, S.; Cotlet, M.; Stefan, Alina; Wiesler, Uwe-Martin; Herrmann, Andreas; Grebel-Koehler, Dorte; Qu, Jianqiang; Mullen, Klaus; Schryver, Frans C. Fluorescence and Intramolecular Energy Transfer in Polyphenylene Dendrimers. *Macromolecules* 2003, 36, 5918-5925.

Madigan, Jay [curator]. National Aeronautics and Space Administration: What wavelength goes with color?  
[http://science-edu.larc.nasa.gov/EDDOCS/Wavelengths\\_for\\_Colors.html](http://science-edu.larc.nasa.gov/EDDOCS/Wavelengths_for_Colors.html) (accessed February 20, 2012).

Mori, Shinichiro; Endo, Masahiro; Furukawa, Shigeo; Sunaoka, Masayoshi; Nonaka, Hiroi. "Development of high-radiation-sensitive polymer gel for magnetic resonance imaging in three-dimensional dosimetry". *Magnetic Resonance Imaging*, 2005, 23, 691-694.

Perepichka, Dmitrii F.; Perepichka, Igor F.; Meng Hong; Wudl, Fred. Light Emitting Polymers. , *Organic Light-emitting Materials and Devices, Marcel-Dekker Inc., CRC Press*, 2006.

Walters, Keisha B.; Hirt, Douglas E. Grafting of End-Functionalized Poly(*tert*-butyl acrylate) to Poly (ethylene-*co*-acrylic acid) film. *Polymer* 2006, 47, 6567-6574.

Cheung, Tsang; Butson, Martin J.; Yu, Peter K.N. "X-ray energy dependence of the dose response of SIRAD radiation dosimeters". *Applied Radiation and Isotopes*, 2007, 65 (7), 814-817.

Yu, J.W.; Kim, J.K.; Hong, J.M.; Kim, Y.C.; Cho, H.N.; Kim, D.Y.; Kim, C.Y. Molecular Design of Light Emitting Polymers. *Chinese Journal of Polymer Science* 2001, 18 (3), 227-237.

Zhao, Q.; Liu, S.; Huang, W. Polyfluorene-Based Blue-Emitting Materials. *Macrol. Chem. Phys.* 2009, 210, 1580-1590.

## CHAPTER VII

### RECOMMENDATIONS

#### 7.1 Recommendations for Artificial Saliva

Based on the inconsistency between drug-doped salivas in all three methods of characterization (pH, rheology, and pendant drop), it is suggested that future studies examine the effects of drug concentration and how varying these parameters influences the physicochemical and viscoelastic properties. Using one representative artificial saliva as opposed to three would eliminate the variances between saliva solutions, and the true effects of concentration and other investigated characteristics could be examined without having to take into effect the differences in saliva composition. Also, investigating the effect of phospholipid phosphatidylethanolamine (PE) in the artificial saliva as opposed to phosphatidylserine (PS) to see changes in physicochemical properties in artificial saliva and how the properties compare to natural saliva.

Investigating the effects of other influential factors such as lipophilicity, hydrophobicity, and particle charge would also be beneficial. A suggested method would be using the same core particle substrate as a standard reference, and coating the particle with varying materials with different properties, such as a hydrophilic poly(ethylene glycol) coating versus a hydrophilic amine functional polymer coating. Studying the lipophilicity of drugs using octanol-water partition coefficients (studies underway) is also extremely beneficial, since lipophilicity is a key parameter in drug diffusion. A review paper summarizing the effects of various surface chemistries and concentration

dependence would be an asset to the field of aerosol particulate studies and biological modeling.

Diffusion modeling would also be enhanced by modeling the gel and sol layers of mucus as opposed to one mucus substrate. Temperature-dependent diffusion studies using a temperature-controlled ATR-FTIR crystal would be beneficial. The temperature of the human body, at 37 °C, would affect the diffusion of a drug particle as opposed to 25 °C ambient temperature.

## **7.2 Recommendations for Light-sensitive Polymer Films**

The EAA-OBC and EAA-BDMF films both fluoresced blue when illuminated with UV light at a wavelength of 254 nm. Both films also produced peaks in the red region of visible light when characterized by fluorescence spectrophotometry (FS). It is recommended that the films be illuminated with other UV wavelengths to see the films fluoresce red. The films could also be illuminated a wavelength where no FS peaks were seen to see if the films have any fluorescence in those ranges. Investigating the properties of the films with other radiation sources such as gamma ( $\gamma$ ) or alpha ( $\alpha$ ) would provide insight to the potential of the films' surface chemistry as indicators for other types of irradiation. Grafting the film surface chemistry to other substrates with differing surface chemistry and terminal functional groups would also be beneficial for determining the effects of spacing on color emission.

Investigating environmental effects on the films and their aging properties would be an interesting characterization study. The films could be characterized as newly made films, and then stored in a variety of environmental conditions such as humid or dry

environments, as well as hot and cold surroundings. At various time intervals, the films could again be characterized to determine the effects of the various environments.

## APPENDIX A

### FTIR METHODS: ATR, TRANSMISSION, AND DRIFTS



## A.1 FTIR Methods: ATR, Transmission, and DRIFTS

All FTIR (Fourier transform infrared) spectroscopy data was collected on a Nicolet 6700 FTIR spectrometer (Thermo Electron Corporation) using Omnic software (version 8.1.10, Thermo Fisher Scientific 1992-2009). In this research, either a liquid nitrogen cooled MCT A\* (mercury-cadmium-telluride) detector or a deuterated triglycine sulfate (DTGS) detector with an extended range KBr beam splitter was used. Two accessories were used to collect attenuated total reflection (ATR-FTIR) spectra: (1) Pike Technologies Veemax II accessory with a 60° zinc selenide crystal for film and liquid samples or a 65° germanium crystal for gold wafer samples; (2) Pike Technologies MIRacle-ATR accessory with a 45° diamond/ZnSe crystal. For transmission FTIR, a universal sample holder was used. Diffused reflectance infrared Fourier transform spectroscopy (DRIFTS) were performed using a Pike Technologies EasyDiff accessory.

## A.2 FTIR Set-Up

1. Clear the air line (Figure A.1 below depicts the airline setup)
  - a. Check the sink to make sure there is no glassware and make sure everyone in the lab is wearing earplugs.
  - b. Carefully climb up on the counter to the right of the Waters GPC.
  - c. Close the yellow valve by positioning the handle perpendicular to the airline (Labeled 1 in Fig. A.1).
  - d. Open the red valve by positioning the handle parallel to the airline (Labeled 2 in Fig. A.1).

- e. There are two filters to the right of the yellow valve. Loosen the screws at the bottom of each filter. Air will be released from the bottom of the filters (Labeled 3 in Fig.A.1).

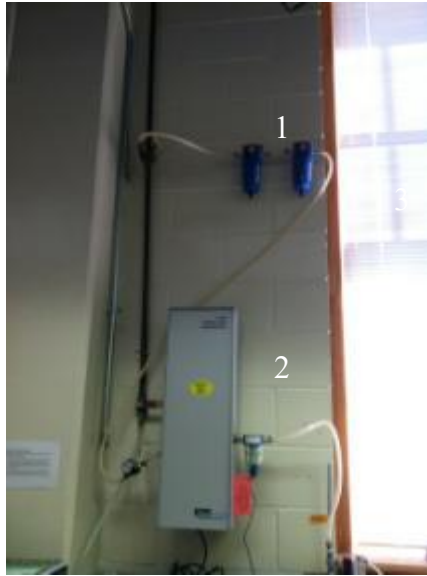


Figure A.1 Airline valve setup in PolySEL Lab 180

- f. Watch the airflow into the sink until there is no more moisture coming out of the hose with the compressed air that is also exiting. Once there is no more water, close the screws of the filters, then close the red valve, and then open the yellow valve.
  - g. Check the flow meter going into the FTIR to make sure there is 30 psi flowing into the FTIR.
2. Place the accessory being used into the FTIR
    - a. The Veemax II ATR accessory and the MIRacle-ATR accessory both have an air line that attaches to the FTIR at the bottom left of the FTIR

chamber. Each accessory also comes with two “ears” that attach to the entrance and exit of the FTIR and seals the accessory from external air. While not in use, each of the holes on the side of either accessory should be sealed with Parafilm<sup>®</sup> to prevent anything foreign from entering the accessory chamber.

- b. The DRIFTS accessory as well as Transmission accessory are run with the main chamber lid closed.
- c. Ask for help before attempting to transition between FTIR accessories for the first time.

3. Add liquid nitrogen to the liquid nitrogen trap to cool the MCT detector

- a. The liquid nitrogen chamber is on the left side of the FTIR covered by a circular lid.
- b. Open the lid, remove the plug and place the funnel (plastic funnel with metal stem and Styrofoam barrier) into the hole.
- c. Pour liquid nitrogen into the funnel slowly, allowing enough time the liquid nitrogen to flow into the FTIR liquid nitrogen chamber and to not overflow the funnel. If the liquid nitrogen overflows (the excess liquid nitrogen can be seen at the base of the funnel/entrance to the liquid nitrogen chamber), a loud crackling noise can be heard.

Overflowing the liquid nitrogen will damage the FTIR benchtop and accelerate the deterioration of the rubber gasket surrounding the liquid nitrogen chamber.

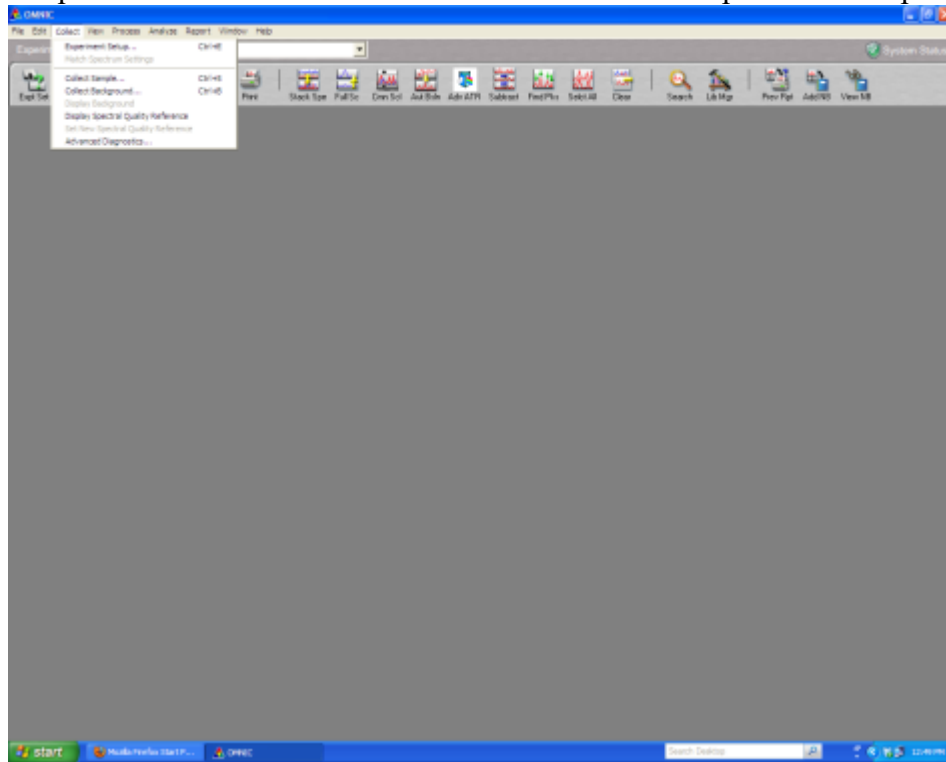
- d. Remove the funnel and gently place it on a paper towel on the benchtop. Since the funnel is frozen, it will crack if placed forcefully or dropped.
- e. Replace the plug into the liquid nitrogen chamber and close the chamber cover slightly. Wait a few minutes before completely closing the cover to the chamber to avoid damaging the plastic cover or rubber gasket. These will fracture if physically forced when frozen.
- f. Wait approximately 20 minutes for the detector to completely cool and the FTIR interior to purge prior to running samples.

#### 4. Aligning the FTIR

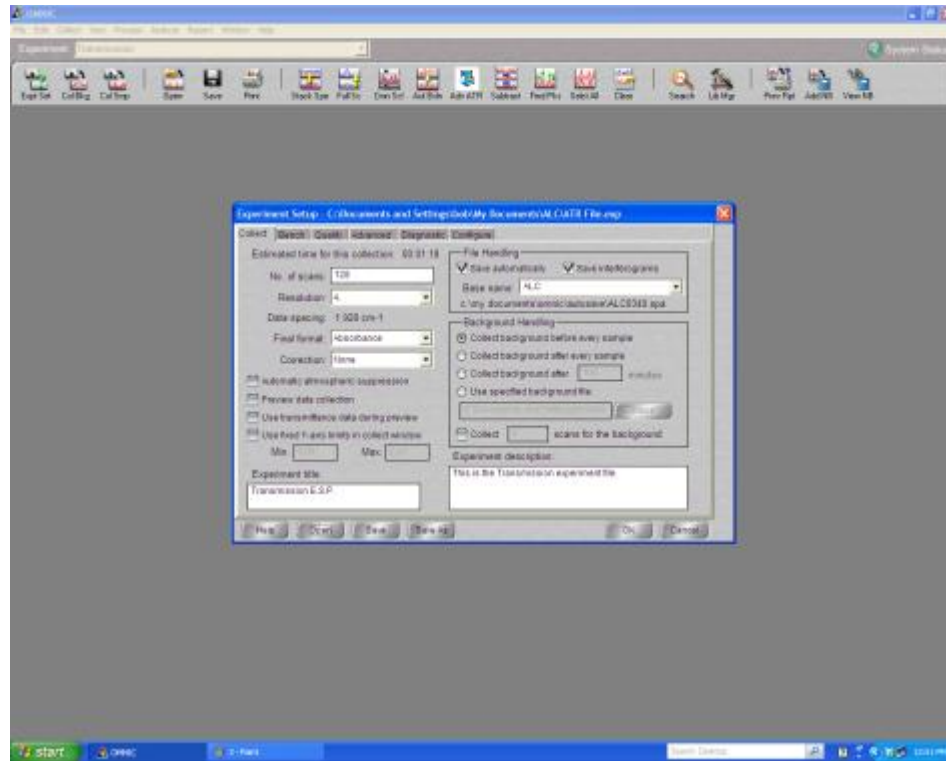
- a. Aligning the FTIR should be done once per week in the transmission mode. Instructions for alignment are available in the FTIR manual as well as a supplemental manual prepared by another member of the PolySEL research group.

### A.3 Data Collection and Use of OMNIC Software

Open the OMNIC Software and select “Collect → Experiment Setup”



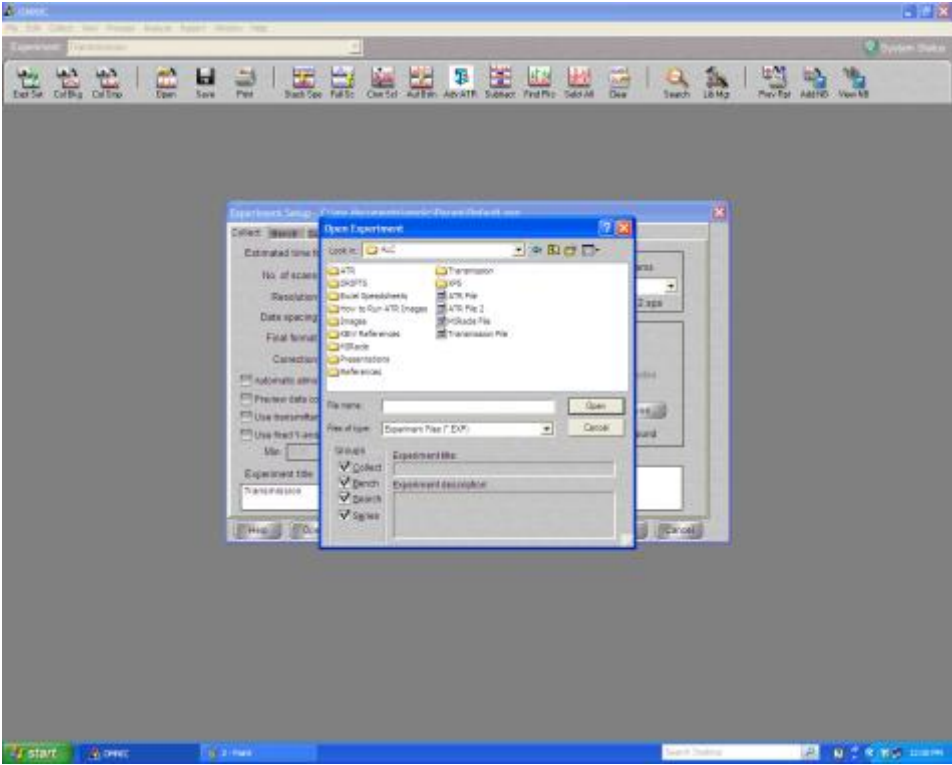
1. The Experiment Setup window will open



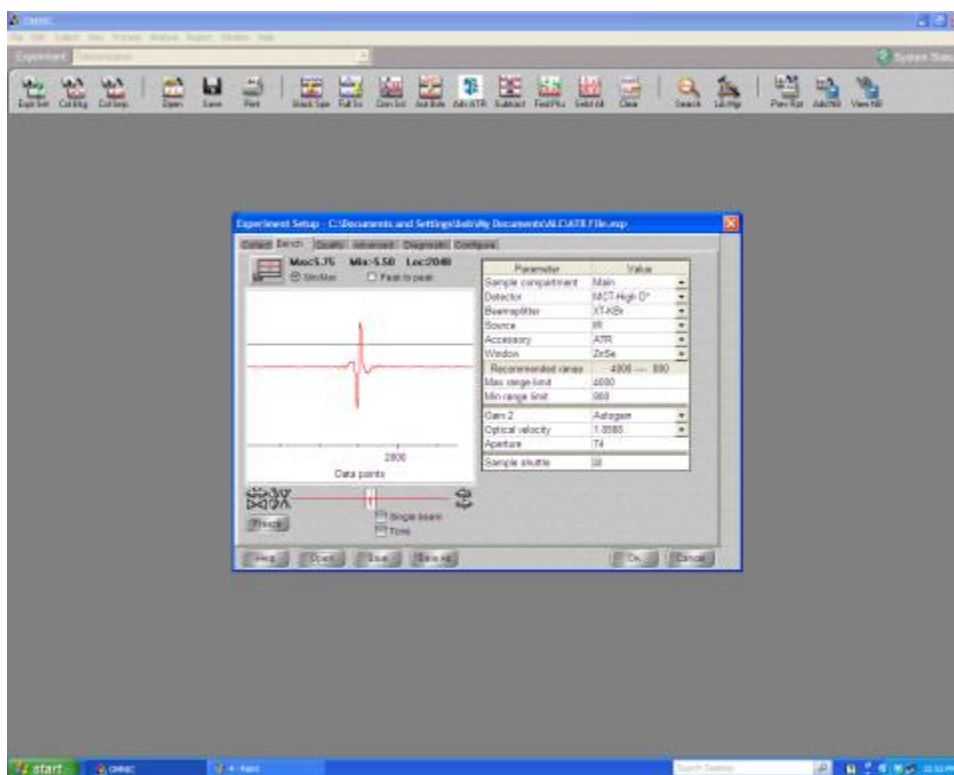
In the “Collect” tab, the number of scans, resolution, and background collection method is set. For polymer films, 128 or 256 scans are recommended. For liquid samples, 128 scans is recommended, except for time resolved diffusion spectra collection, where 64 or 32 scans is recommended due to the speed with which the spectra need to be collected and the need to not have combined/averaged (but rather discrete) spectral information. For Au wafers with thick surface coatings, 256 scans are recommended.

2. Typically, each user has saved setup files for the types of samples and FTIR each person uses. To access a saved setup file, click “open” on the bottom left of the collect tab, select the folder the file is saved in, and click “open”. The saved file with its parameters will load into the OMNIC Experiment Setup

window.



- It is also important to check the “Bench” tab in the Experiment Setup window prior to collecting the background or any samples

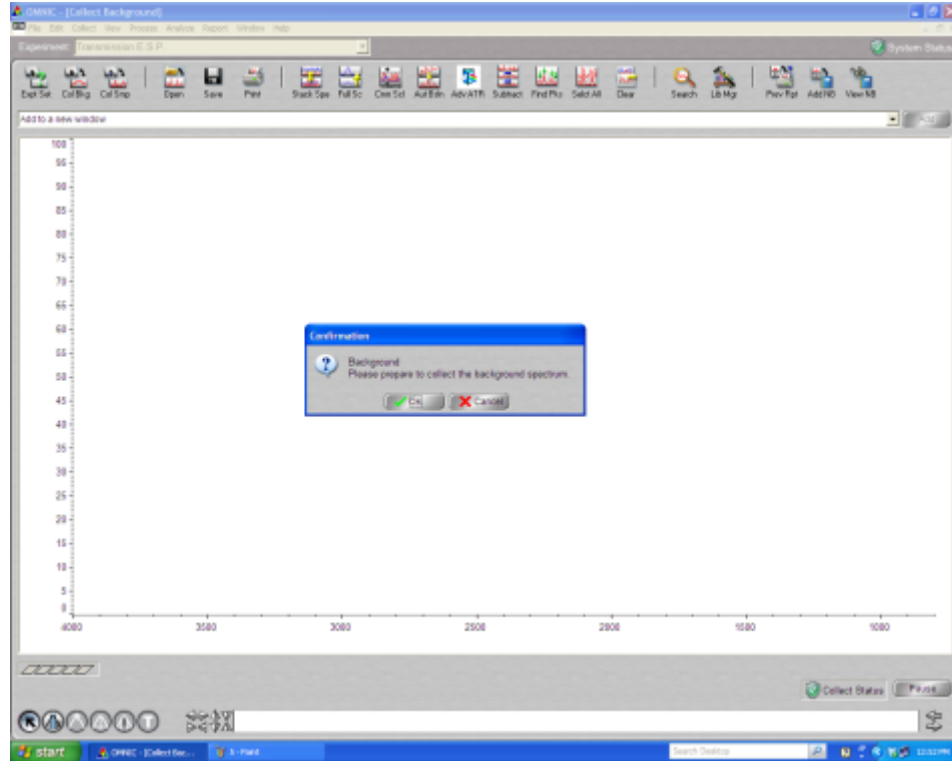


Here, the user can see the interferogram strength, change the type of detector for data collection, and edit the collection range, gain, and aperture. If the interferogram is too strong ( $>10$ ) such that the detector is saturated, a physical screen can be inserted at the FTIR beam path exit or the aperture can be reduced.

- Once the parameters have been confirmed in the Experiment Setup window, click “ok” at the bottom right of the Experiment Setup window. Next, go to the top left of the OMNIC software window and click “ColBkg” for “Collect

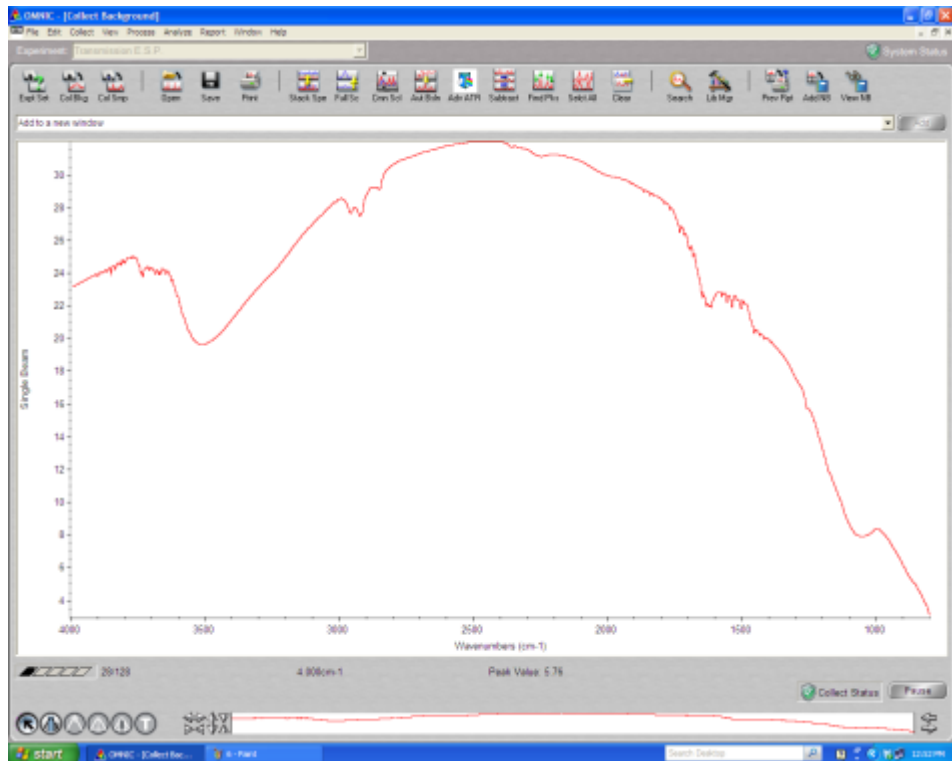


Background”.



A window will open to confirm that the user is prepared to collect the background. Make sure the crystal being used has been cleaned and allowed to dry (no residual solvent) for Veemax or MIRacle ATR, or that the chamber has been closed for DRIFTS or Transmission, and that the FTIR has had enough time to purge before collecting the background for all collection techniques. Without taking these steps, there will be strong water peaks that appear in the background and most likely there will subsequently be negative peaks in the sample spectra.

5. The background will begin collecting and take 1-3 minutes depending on the number of scans the user selected.



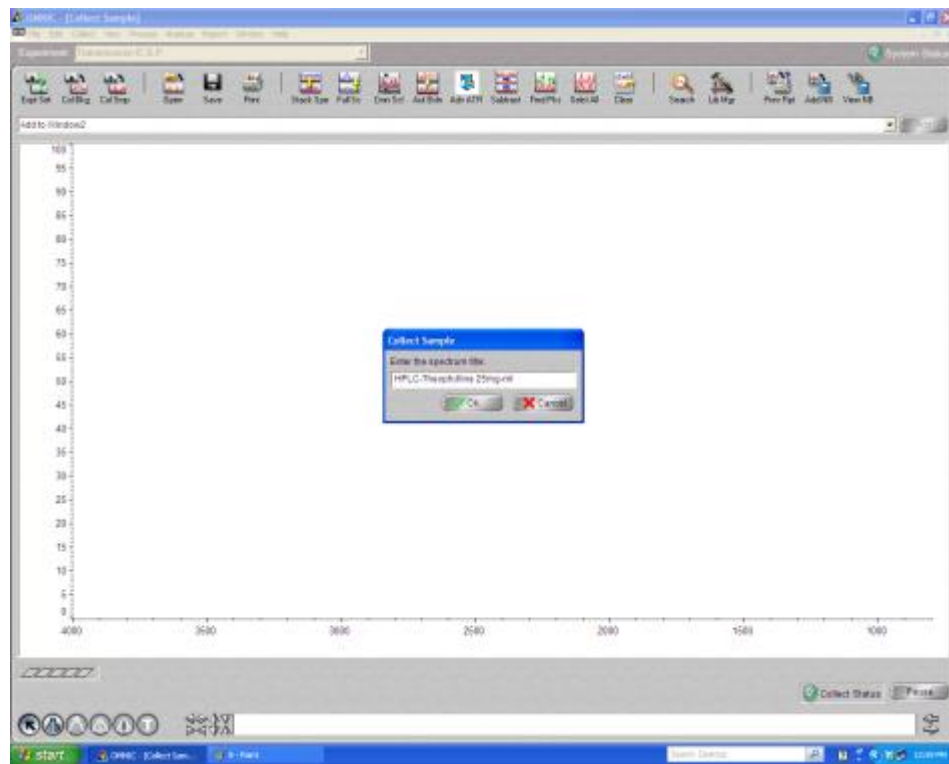
- Once the background has been collected, select “yes” in the popup window to add the background to a window.



Go to “File→ Save As” and save the background spectra in the folder of choice.

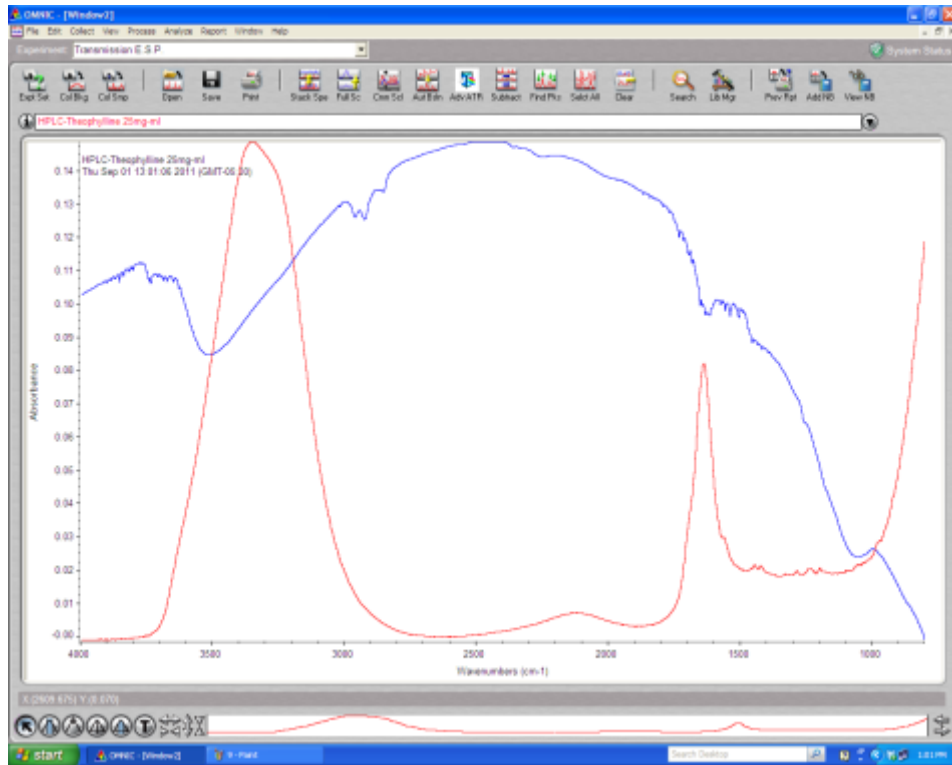
Next, back in the OMNIC software, go to “Collect→Experiment Setup→Use Specified Background” and select the background file that has previously been saved, and click “ok”.

7. Next, load the sample. Once the sample is situated, select “ColSmp” for “Collect Sample”. Name the sample in the first pop up window, click “ok”, and then “ok” again in the second pop up window. Sample spectra will then be collected.



8. Once the sample spectrum is done being collected, select “yes” to add the spectra to a window (usually the same window of the background). However,

be aware of which window OMNIC is adding the spectra in case any changes need to be made.



9. Next, the sample spectra can be saved individually or as a group if there are multiple spectra in the user's data folder.
10. Data collection using the OMNIC software follows the same procedure for each method of FTIR data collection. Make sure that the parameters are appropriate for the method being used.

## A.4 Sample Set-Up

### A.4.1 Veemax II ATR

The Veemax ATR is most commonly used for films or liquid samples with the ZnSe crystal and wafers with the 65° germanium crystal. The incidence angle for the

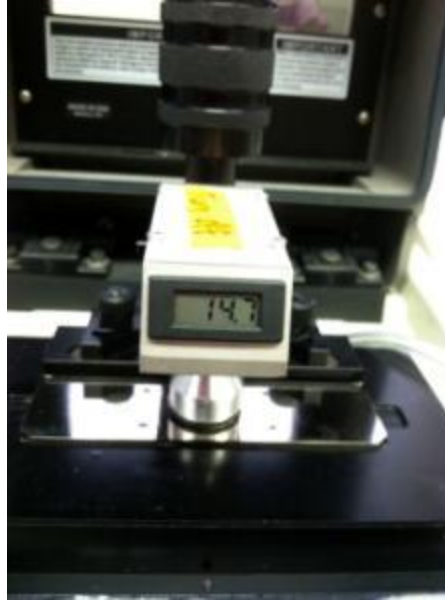
ZnSe crystal and the standard germanium crystal is  $60^\circ$  and  $65^\circ$  for the  $65^\circ$  germanium crystal. Adjust the incidence angle using the knob on the front of the Veemax accessory.

To clean any of the Veemax crystals, moisten a cotton ball generously with methanol, rub the crystal in a circular motion, dry the crystal with a new, dry cotton ball, and then wait a few minutes for any residual methanol to evaporate prior to placing a sample or collecting a background spectrum.

To collect sample spectra for films or wafers, place the sample on the crystal.

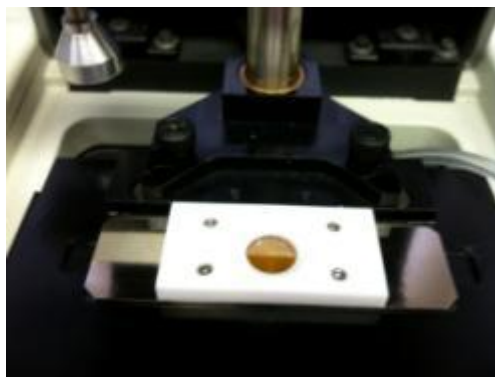


Set the sample in place by tightening the clamp slowly. Uniform force is necessary for consistent contact between the sample and the crystal. Without adequate contact, sample spectra will be noisy, inconsistent, and generally cannot be used without analysis for ratios in order to generate semi-quantitative data.



The sample is now ready for data collection. Once spectra collection is completed for this sample, loosen the clamp, rotate the clamp from over the crystal and sample, remove the sample carefully so to not scratch the crystal surface, and clean the crystal before moving on to the next sample.

To collect sample spectra for liquid samples, clean the crystal and then attach a previously cleaned liquid retainer, fastening the screws to the crystal plate using an Allen wrench. To clean the liquid retainer, methanol with a cotton ball is usually adequate. It is recommended that the user remove the rubber O-ring while cleaning to ensure there is no residual solvent or sample trapped beneath the O-ring. Cleaning using the glassware cleaning method can also be used. For especially difficult samples, sonication in methanol followed by wiping with methanol cotton ball is recommended. The liquid retainer can also be sonicated in water. Make sure the O-ring is replaced completely to ensure the seal with the ATR crystal is good.



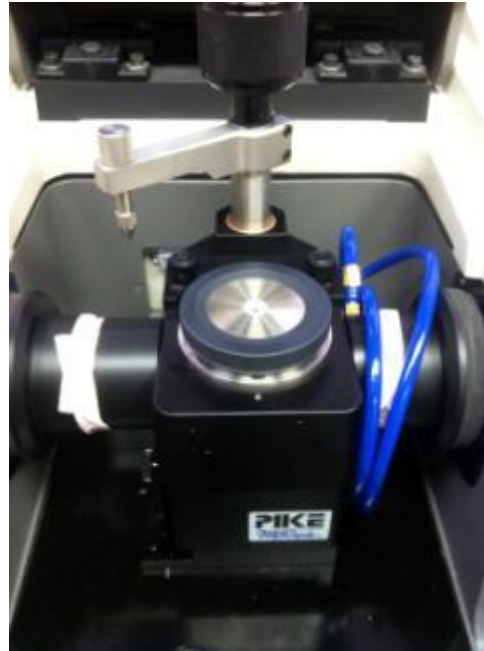
Using a pipet, gently add the liquid sample to the center of the crystal until the crystal is covered by a layer of the liquid. It is not necessary to fill the entire retainer volume with the liquid sample in order to collect good spectra. If the sample contains any hazardous or volatile components, cover the sample well with a clean glass slide to prevent evaporation and/or exposure of the user to a hazardous substance. For all liquid samples, monitor the liquid level as well as the edges of the liquid retainer to ensure no solvent is leaking under the retainer. Once the liquid has been placed on the crystal, the sample is ready for data collection.

Once spectra are collected, use a dry cotton ball to soak up the sample off the crystal surface before removing the liquid retainer. With the retainer still attached, clean the crystal with one or more methanol soaked cotton balls. Remove the retainer and clean the retainer and crystal thoroughly with methanol before moving on to the next sample.

#### **A.4.2 MIRacle ATR**

The MIRacle-ATR can be used for liquid, solid, and powder samples. The sample setup is very similar to the Veemax ATR setup. For solid samples such as films, there is no need for the liquid retainer or mounting ring to be attached. Clean the crystal the same way as with the Veemax ATR, wait for residual methanol to evaporate, collect the background, and then place the sample on top of the crystal and secure with the pressure

clamp and flat bottom pressure tip. For liquid or powder samples, attach the liquid retainer and secure the retainer with the mounting ring. For powder samples, gently “spoon” the sample into the sampling area with a spatula and use the pressure clamp with the concave tip to secure the powder.

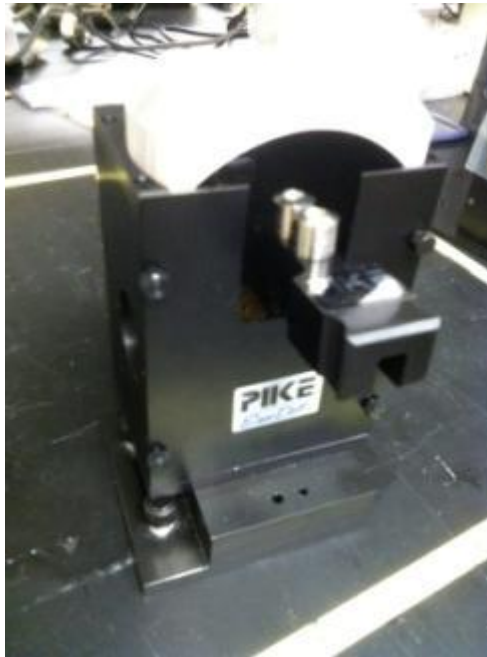


#### A.4.3 DRIFTS

DRIFTS is most commonly used to collect powder samples. To collect DRIFTS samples, a few preparation steps are required prior to setting up the sample for collection. First, measure out the powder sample and KBr powder in a 5:95 wt% ratio. Since only a small amount of powder mixture is required, 0.005 grams of sample and 0.095 grams of KBr powder is recommended. Mix the KBr powder and sample thoroughly in the mortar and pestle. Transfer to a weighing boat for ease of sample transfer into the DRIFTS sample cup or into a small vial for storage in the desiccator. Transfer sample into one of the metal sample cups in the DRIFTS sample preparation kit. Using a razorblade smooth



the surface to ensure a relatively flat sample surface from which the light will bounce. Prepare the second metal sample cup with neat KBr powder (no sample added) that has also been crushed and smoothed in the manner described above. Place the neat KBr powder sample container in the first sample slot (the slot the goes into the DRIFTS accessory first) and the Sample-KBr mixture sample container into the second sample slot (the slot further from the end that enters the DRIFTS accessory first). Very carefully, open the top of the FTIR hood and place the samples into the DRIFTS accessory.

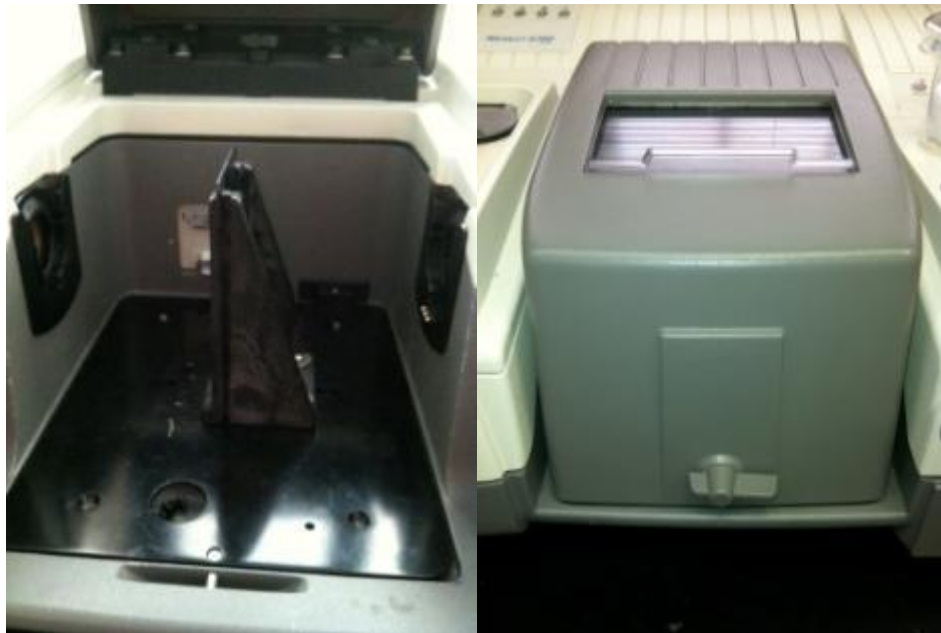


Pull back on the holder gently to not disturb the smooth powder, close the lid of the FTIR sample compartment hood and wait approximately 25-30 minutes for the FTIR to purge. Collect the neat KBr background when an appropriate amount of time has passed, then open the FTIR hood and quickly but carefully push the sample holder forward. The Sample-KBr mixture is now in place to have its spectrum collected.

Once the sample spectrum collection is completed, remove the sample holder and clean the metal sample cup containing the Sample-KBr powder mixture. Retain the neat KBr cup, if there are more samples to run. Or clean both sample cups if spectra collection is complete for all samples.

#### **A.4.4 Transmission FTIR**

Transmission FTIR is unique in that spectral information is collected from the entire sample thickness, as opposed to sample (sub) surface as is the case in the other FTIR collection methods described above. To use this method, light must be transmitted completely through the sample. The transmission method is therefore most commonly used on translucent gases, liquids, and (polymer) films. Insert the transmission accessory and close the FTIR sample compartment hood to allow the FTIR to purge. Wait approximately 25-30 minutes before collecting the background (open/empty sample compartment) and sample spectra.



For polymer films, place the sample in the sample clamp and after collecting the background, quickly slide the sample into the grooves in the Transmission accessory, and close the sliding door on the hood. The sample is now ready for spectra collection.

To remove the sample, open the lid to the FTIR hood and quickly and carefully slide the sample clamp out of the accessory. Keep the lid to the hood closed between samples.

APPENDIX B  
SURFACE ANALYSIS AND DEPTH OF PENETRATION: A COMPARISON OF  
DIFFERENT SURFACE-SENSITIVE FTIR TECHNIQUES

## B.1 Introduction to Surface Chemistry Characterization Methods

Several characterization methods are available to researchers to investigate the surface chemistry of samples. Commonly used techniques available to our laboratories include X-ray photoelectron spectroscopy (XPS), contact angle goniometry, Fourier transform infrared spectroscopy (FTIR), scanning electron microscopy (SEM), transmission electron microscopy (TEM) and atomic force microscopy (AFM). Each technique uses a different method to collect sample data. XPS uses an X-ray beam to irradiate samples and has a relative depth of penetration of 1  $\mu\text{m}$ , while FTIR uses an infrared beam and measures the sample's absorption of the IR beam. The FTIR depth of penetration can range from approximately 0.1 to  $>2 \mu\text{m}$  [Kwan 1998], depending on the parameters used. Contact angle goniometry has no penetration abilities, and conveys surface chemistry information using interfacial tension and contact angles, which are impacted by the surface functional groups present. In electron microscopy techniques a primary electron beam is passed through the sample and produce excited backscattered secondary electrons that generate a sample image [John Innes Center 2012]. TEM completely penetrates the sample thickness, while SEM scans the surface with the electron beam and has an approximate depth of penetration range of 0.1 to  $>3 \mu\text{m}$  that is dependent on sample composition, density, atomic weight, and beam energy [Muller 2008]. TEM specimens do have a maximum thickness dependent upon instrument capabilities. Samples with a thickness greater than the maximum thickness in their native state must be amenable to being sliced and cryotomed.

The versatility, reliability, and speed of FTIR spectroscopy make it an ideal characterization method. External reflectance (ER-FTIR) is an FTIR spectroscopic

technique that does not utilize a crystal since the IR beam from the source is reflected by the sample to the detector. Attenuated total reflectance (ATR-FTIR) does not require a solid surface, as is the case with ER-FTIR, and is a fast and easy FTIR technique. In addition, there are several options for crystal and ATR accessory configurations allowing for a wide range of sample types to be examined. Characteristics that must be considered include the ATR crystal properties, angle of incidence, sample material properties, and depth of investigation desired.

Of the factors that must be considered when configuring an ATR-FTIR study, one of the most important is the crystal selection. The primary consideration is, of course, the absence of IR light absorbance in the wavelength range of interest. Selection of the crystal is also dependent on the crystal chemical resistance for the sample and any solvent present, durability, hardness, and refractive index. Table B.1 summarizes some key properties of commonly used ATR-FTIR crystals.

Table B.1 Tabulated Summary of Commonly used ATR-FTIR Crystal Properties Important for Crystal Selection [Pike Technologies, 2011].

Crystal Material	Refractive Index	Long Wave Length Cutoff wavenumber (cm <sup>-1</sup> )	Hardness (kg/mm <sup>2</sup> )	General Sample and Solvent Compatibility
Diamond/ZnSe	2.4	525	5700	Can withstand hard, acidic or alkaline samples; pH range 1-14
Ge	4	780	550	General purpose, or rubber or carbon-filled samples; pH range 1-4
Si	3.4	1500	1150	Useful for far-IR spectral ranges; pH range 1-12
ZnSe	2.4	525	120	General purpose ATR crystal; pH range 5-9

Most commonly used ATR crystals have a refractive index between 2.4 and 4.0, which is higher than most organic samples [Dole 2011]. Organic solvents such as tetrahydrofuran, toluene, and acetone have refractive indices of 1.41, 1.50, and 1.37, respectively. In calculating depth of penetration, for a given sample higher crystal refractive indices result in lower depths of penetration. It is also important to consider sample composition when choosing an ATR crystal. For example, zinc selenide (ZnSe) would not be a good crystal choice for an acidic sample since it would etch the crystal surface [Kazarian and Chan, 2010]. A primary factor in obtaining quality ATR-FTIR data is dependent upon the sample surface since intimate contact is necessary to obtain suitable signal-to-noise ratio suitable. However, obtaining this contact area—generally

through use of a clamp—is an issue for hard and/or rough samples that would scratch the surface of a soft crystal such as ZnSe. Some chemicals can react and etch the surface of the crystal, as well as acidic solutions  $\text{pH} > 5$  [Dole 2011, Pike Technologies 2011]. Etched or scratched crystal surfaces result in lower crystal-sample contact and therefore lower quality spectra, lower depth of penetration, and potential accessory contamination since the scratches cannot be cleaned easily. Lower and inconsistent sample-crystal contact may result in spectral errors such as inaccurate peak detection, increased noise levels, and the presence of negative peaks. Refer to Appendix A for information on how to ensure consistent sample-crystal contact.

Crystal parameters are chosen to optimize sensitivity based on the crystal and sample compositions. One parameter that can be controlled is incidence angle. For a given sample-crystal combination, a higher incidence angle results in a lower depth of penetration and so consequently lower spectral peak intensities [Kazarian and Chan, 2010]. The minimum and maximum depths of penetration are important to consider when choosing an ATR crystal depending on whether only surface information is desired, or you also want to interrogate a significant portion of sub-surface space to maximize the signal or detect as functional groups that may be present in that region of the sample. Based on sample composition and theorized reactions, the crystal must be selected for compatibility with the sample. For example, self-assembled monolayers (SAMs) grafted from gold wafers need a crystal that is sensitive enough to allow beam penetration through the grafted surface chemistry, but must not penetrate completely through the monolayer to the gold wafer, since the gold will reflect an excess of light and overshadow the spectral peaks of the surface chemistry functional groups. For surface-modified films, a larger depth of penetration is desired due to the ability of some



molecules to penetrate into the film, while others are too large and restricted to the film's surface. A larger depth of penetration would permit the analysis of a greater thickness of film.

Figure B.1 illustrates how the FTIR instrument collects ATR spectra. The IR beam is transmitted through the crystal where it reflects evanescent waves off the crystal and into the sample surface, where light is absorbed or reflected. Reflected light is bounced back to the detector. Evanescent waves are only effective if the crystal has a higher refractive index than the sample. The outputted spectrum contains absorbance peaks that correspond to molecular motions of the functional groups that made contact with the reflected light.

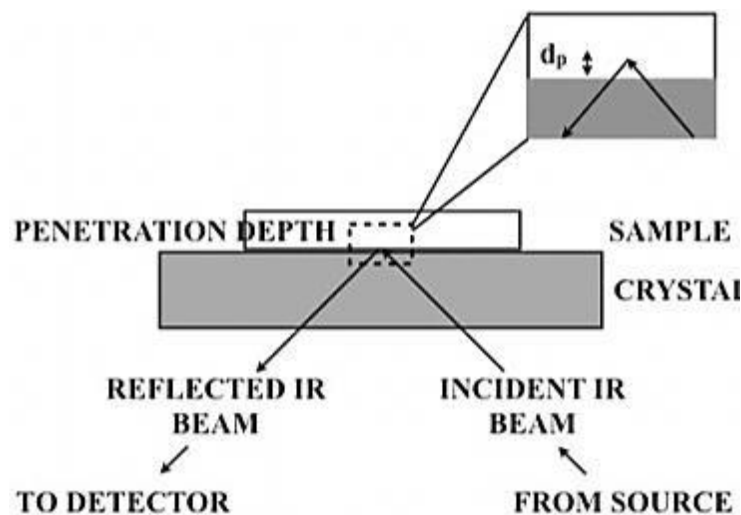


Figure B.1 Spectra collection using a single-bounce attenuated total reflectance (ATR) FTIR accessory.

## B.2 Depth of Penetration

There are several factors that affect the depth of penetration of the FTIR light source and therefore the portion of the sample interrogated. Equation B.1 [Dole 2011] is used to calculate the depth of penetration of the FTIR light source into the sample:

$$d_p = \frac{\lambda}{2 \rho (n_1^2 \sin^2 \theta - n_2^2)^{1/2}} \quad \text{Eq. B.1}$$

where  $\lambda$  is the wavelength of light,  $\theta$  is the angle of incidence of the IR beam, and  $n_1$  and  $n_2$  are the refractive indices of the crystal and sample, respectively.

### B.3 Depth of Penetration: Comparing ATR Techniques

ATR experiments in our laboratories utilize different crystals (with different refractive indices) and different incidence angles when collecting sample spectra. While other crystal options are available from vendors, in our laboratories the MIRacle ATR accessory is configured with a 45° ZnSe-diamond crystal, and the Veemax ATR can be outfitted with a ZnSe (60°) or germanium (60° or 65°) crystal. Table B.1 lists the refractive indices, incidence angles, and ranges of depth of penetrations for the crystals used for this research. The depth of penetration ranges shown are calculated for a poly(ethylene co-acrylic acid) (EAA) sample which has a refractive index of 1.408. There are two different detectors available on the Nicolet 6700 FTIR that was used for data collection, MCT and DGTS. Each is capable of collecting over a different wavenumber ( $1/\lambda$ ) range; the MCT and DGTS detector wavenumber ranges used in this research are 4000-800  $\text{cm}^{-1}$  and 7000-400  $\text{cm}^{-1}$ , respectively. Since wavelength is a variable in the depth of penetration calculation, the exact wavenumber (or wavenumber range) of interest impacts the  $d_p$  (or  $d_p$  range). Therefore, if the same wavenumber range is being used for both detectors, there is no difference in the  $d_p$ . It can be seen from Table B.2 that the diamond crystal, with its corresponding parameters, gives the MIRacle ATR the greatest depth of penetration, at least for the EAA films.

Table B.2 Table of Refractive Indices [Kazarian and Chan, 2010], Incidence Angles, and Calculated Depth of penetration ( $d_p$ ) ranges for an EAA film sample ( $n_2=1.408$ ) for the four ATR crystal options available in our laboratories.

Crystal Material	Crystal Refractive Index ( $n_1$ )	Incidence Angle ( $\theta$ )	EAA $d_p$ range ( $\mu\text{m}$ )	
			MCT detector	DTGS detector
Diamond	2.4	45	0.42-2.10	0.24-4.20
Zinc Selenide	2.4	60	0.26-1.30	0.15-2.60
Germanium	4.0	60	0.13-0.63	0.07-1.26
Germanium	4.0	65	0.12-0.60	0.07-0.60

Note that the available  $d_p$  for each crystal option varies based upon the available wavenumber range of each detector (MCT: 4000-800  $\text{cm}^{-1}$ ; DTGS: 7000-400  $\text{cm}^{-1}$ ).

#### B.4 Comparing spectra of ATR Techniques

Figure B.2 shows a common scale comparison of Veemax and MIRacle ATR-FTIR spectra for an EAA-NH<sub>2</sub> film. MIRacle ATR provides stronger (higher intensity) peaks than the Veemax ATR. This is due to the fact that MIRacle ATR has a greater depth of penetration during sample collection. Since more sample is being contacted by the IR radiation, there is a strong signal. When compatible with an experiment and sample type, the MIRacle accessory is therefore the preferred technique.

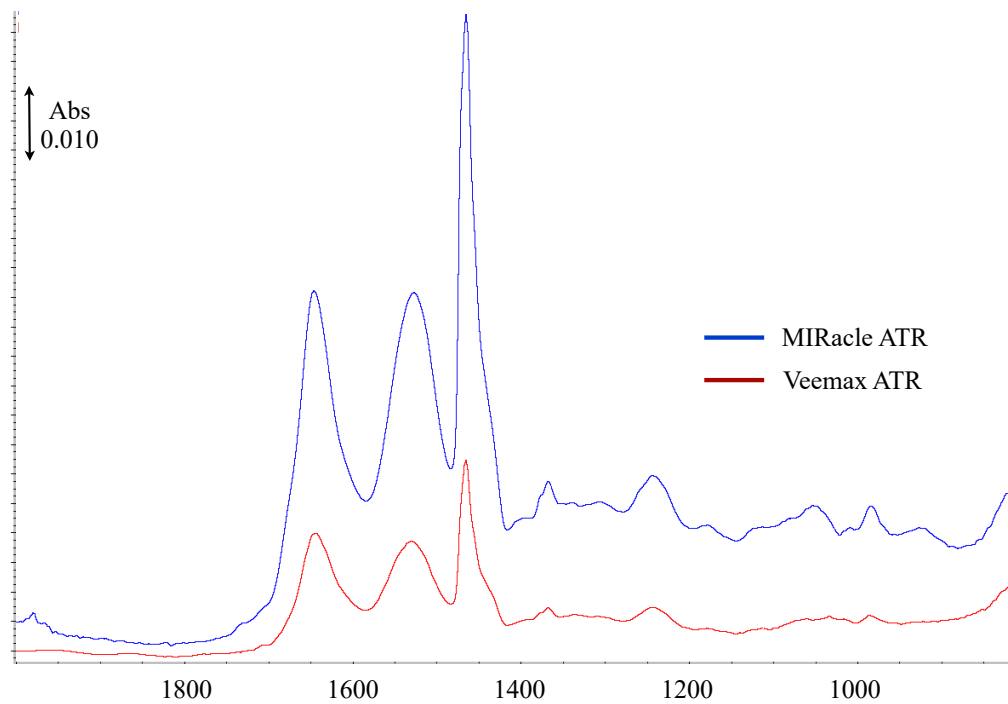


Figure B.2 Comparison of MIRacle and Veemax ATR spectra for an EAA-NH<sub>2</sub> film with absorbance presented on a common scale.

## B.5 References

Dole, M.N. Advance Applications of Fourier Transform Infrared Spectroscopy. *International Journal of Pharmaceutical Sciences: Review and Research* 7, 2, 2011.

Kazarian, S.; Chan, K. Macro-and Micro-Attenuated Total Reflection Fourier Transform Infrared Spectroscopic Imaging. *Applied Spectroscopy*, 2010, 64(5) 135A-152A.

Kwan Jr., Kermit S. The Role of Penetrant Structure on the Transport and Mechanical Properties of a Thermoset Adhesive. Ph.D. Dissertation. Virginia Polytechnic Institute and State University, Blacksburg, VA, 1998. Chapter 4: FTIR-ATR Diffusion Study. p. 37.

Meyer, Veronika R. Practical High-Performance Liquid Chromatography, 5<sup>th</sup> ed. 2010, John Wiley and Sons, Ltd.: United Kingdom, p. 82.

Muller, David. Scanning Electron Microscopy, 2008.  
[http://www.ccmr.cornell.edu/igert/modular/docs/3\\_Scanning\\_Electron\\_Microscopy.pdf](http://www.ccmr.cornell.edu/igert/modular/docs/3_Scanning_Electron_Microscopy.pdf)  
(accessed October 21, 2011).

Pike Technologies ATR Crystal Selection. <http://www.piketech.com/ATR-Crystal-Selection.html> (accessed October 9, 2011).

APPENDIX C  
COMPRESSION MOLDER OPERATIONAL GUIDELINES AND PRODUCTION OF  
EVOH FILMS USING COMPRESSION MOLDING

### C.1 Compression Molder Operational Guidelines

A compression molder is available in the Swalm School of Chemical Engineering at Mississippi State University for use, with approval, in the Unit Operations Laboratory. The compression molder was manufactured by Carver, Inc. (model number 3893.4PR1A00, Wabash, Indiana). Due to the danger of using a compression molder, it is important to understand fully how to use the compression molder prior to operating the machine without assistance. A brief set of directions for how to use the compression mold follows.

1. Turn on the main power supply using the large switch to the right of the compression molder.



Figure C.1 Main power source switch.

2. Turn on the power to the compression molder using the red switch located on the right side of the compression molder.



Figure C.2 Picture indicating red switch for powering compression molder.

3. Power on the hydraulic pumps (right rocker) and heated plate (left rocker) using the switches on the instrument panel.



Figure C.3 Instrument control panel.



4. Adjust the temperatures for the upper and lower plates using up and down arrows on the control panel. Set and confirm final use temperatures using the right most button for each temperature controller.
5. Set the pressure by using manual mode (“man”) on right control panel, and set pressure to pounds by pressing “set” three times. Use up and down arrows to choose pressure and confirm by pressing “man”.
6. Wait for the plates and mold to heat to the set temperature.



Figure C.4 Carver, Inc. compression molder (model 3893.4PR1A00).

7. Place the material in mold (prior application of silicon release spray is recommended). Press both green buttons simultaneously and hold until the

desired pressure is reached. Leave sample in press for desired length of time. Press the red button to release the plates. Warning: samples come out of the compression molder at extremely high temperatures. Wearing hot gloves remove the mold carefully and allow the mold to cool before handling the sample.

8. To shut down the instrument, first cool mold to room temperature by opening the water line to instrument using the water spigot on the wall to the right of the press. Next turn off the control panel using the power button on the right side of the instrument and finally shut off the main power source.

## **C.2 Using the Compression Molder to Make EVOH Films**

EVOH (ethyl vinyl alcohol) pellets, produced by Dow Chemical, were molded into films using a compression molder. The films were processed at 190° C and 4000 pounds. Prior to pressing, EVOH pellets must first be dried in a vacuum oven (no heat applied) for 24 hours to evaporate any water that may have adsorbed onto the surface of the pellets. Figure C.5 shows a film that was produced without first drying the pellets.



Figure C.5 EVOH film produced at 190° C and 4000 lb<sub>f</sub> without drying pellets.

As can be seen from Figure C.5, if the pellets are not dried prior to compression molding, a brittle, irregular film is produced. With drying, a thinner, more uniform film is produced. Figure C.6 shows a film produced from dried EVOH pellets.



Figure C.6 EVOH film produced at 190° C 4000 lbs. with dried pellets.

APPENDIX D  
CONTACT ANGLE GONIOMETRY OPERATIONAL GUIDELINES FOR DATA  
COLLECTION AND ANALYSIS

## D.1 Instrument Specifications

All contact angle and pendant drop data was collected using a Kruss EasyDrop with a Teli CCD camera and analyzed using Drop Shape Analysis (DSA) software (version 1.90.0.14, Kruss).

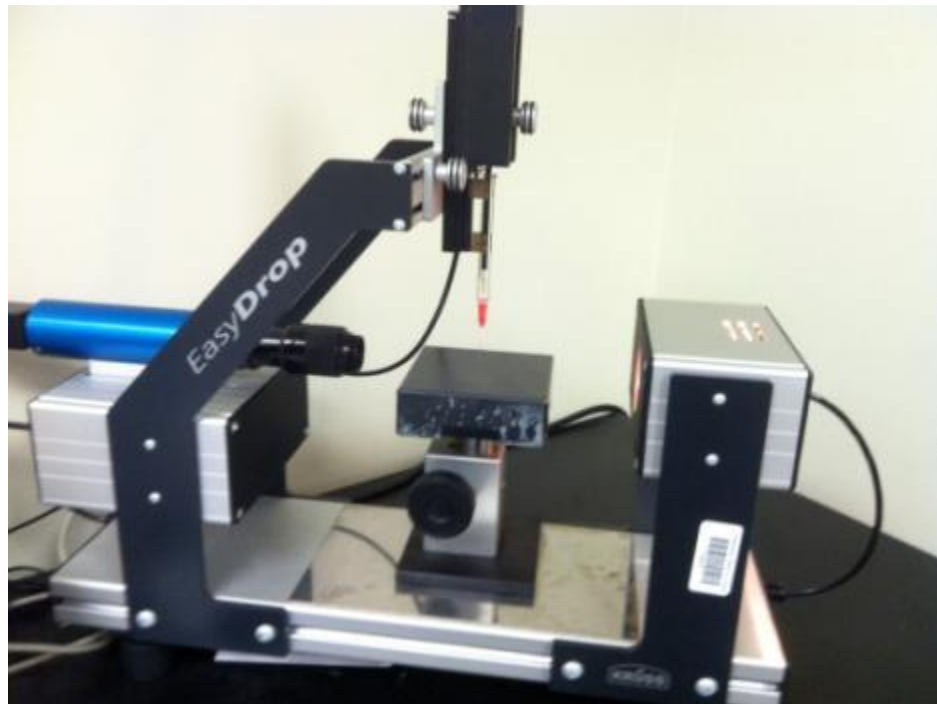


Figure D.1 Kruss EasyDrop Contact Angle Goniometer with syringe loaded.

## D.2 Instrument Set-Up

1. Ensure the instrument is level using a small level placed on the sample stage. Adjust the feet of the EasyDrop if the level needs to be adjusted.
2. Attach either a red (sessile drop) or green (pendant drop) needle to a Hamilton syringe.

3. Flush the needle several times using the fluid that will be used for data collection.
4. Fill the needle, and ensure there are no bubbles in the tip.
5. Open DSA software, then go to the Device Control Panel and open the “Dosing” tab.
6. Click the button for “Contin” to set the dosing control to continuous.
7. Note: The up arrow indicates moving the plunger of the syringe up and the down arrow indicates moving the syringe plunger down. Using the up or down arrows, adjust the position of the syringe plunger holder to the proper position and insert the syringe into the holder extremely carefully to avoid breaking the glass syringe barrel. Refer to Figure D.2 for an illustration of proper syringe placement.

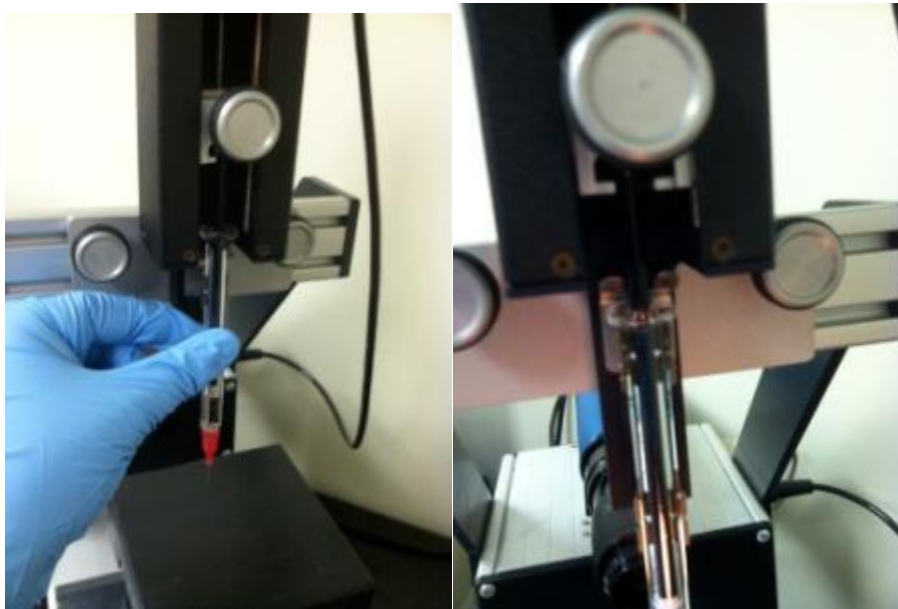


Figure D.2 Images depicting the proper syringe (left) and syringe plunger (right) placement on the Kruss EasyDrop Contact Angle Goniometer.

- Using the dosing control down arrow, depress the syringe plunger until fluid is dispensed out of the needle.

### **D.3 Static Contact Angle**

Before running experimental samples, the static contact angle procedure should be performed on polymer standards (EAA, PTFE, and LDPE) with HPLC water. Table D.1 at the conclusion of this appendix summarizes the reference contact angles for these materials.

- Place sample on sample stage.
- In the DSA software, go to file, menu and click “F-G window.”
- Click on the “Live Video Feed” button (icon of video camera) and make sure the camera and live video window are focused.
- Increase illumination strength to 32 by going to the DSA device control panel and “Imaging” tab.
- Loosen the screw on the back of syringe holder to lower needle into frame. The tip of the syringe needle should be visible on the screen within the live video feed. Tighten the thumb screw once needle is in frame.
- In the DSA device control panel, click the “Dosing” tab, then set the dosing method to “Volume” and set the volume to 5  $\mu\text{L}$ .
- Press the up arrow to dispense 5  $\mu\text{L}$  of fluid.
- Using the up and down dial on the sample holder, slowly raise the sample until it just touches the drop and the drop comes down onto the surface of the sample, then lower the sample platform.

9. Zoom in on the sample using the zoom dial on the camera until the drop almost fills (~ 80%) the F-G window feed, then capture a photo of the drop using the “Snap” button on the tool bar (icon of a camera).
10. Right click on the F-G window, go to “Drop Type”, and click on “Sessile Drop”, then go to “Drop Subtype” and select “Normal Sessile Drop”. Also, make sure “Auto Detect Substrate” is unchecked.
11. Right click on the F-G window, go to baseline type, and select “Linear.”
12. Click on the baseline shown in F-G window, and adjust using arrow keys. The baseline should intersect the drop where the drop meets the substrate.
13. Go to file menu and open “Result Window”, then right click on F-G window and select the appropriate fitting method under contact angle using.
14. Record results in lab notebook and/or data spreadsheet. Save the drop photo file.

#### **D.4 Pendant Drop**

The data collection method of pendant drop is very similar to contact angle.

1. In the DSA software, go to file, menu and click “F-G window.”
2. Click on the “Live Video Feed” button (picture of video camera) and make sure the camera and live video window is focused.
3. Increase illumination strength to 32 by going to the DSA device control panel and “Imaging” tab.
4. Loosen the screw on the back of syringe holder to lower needle into frame. The tip of the syringe needle should be visible on the screen within the live video feed. Tighten the thumb screw once needle is in frame.



5. In the DSA device control panel, click the “Dosing” tab, then set the dosing method to “Volume” and set the volume to 10  $\mu\text{L}$ .
6. Press the up arrow to dispense 10  $\mu\text{L}$  of fluid.
7. Zoom in on the sample using the zoom dial on the camera until the drop almost fills the F-G window feed, then take a picture of the drop using the “Snap” button on the tool bar (button has picture of a camera).
8. Right click on the FG window, go to “Drop Type”, and click on “Pendant Drop”. Also, make sure “Auto Detect Substrate” under “Drop Subtype” is unchecked.
9. On the tool bar, select the “Baseline Detection” button (button looks like a circle representing a sessile drop with a horizontal line through the center).
10. Click on the baseline shown in F-G window, and adjust using arrow keys. The baseline should intersect the drop where the top of the drop meets the bottom of the needle.
11. On the tool bar, select “Extraction” (button looks like outline of a pendant drop), then select “FIT”.
12. Record results and save a picture of the drop.

Table D.1 Reference static contact angles for standard materials

Polymer Film	Reference Contact Angle	Reference
EAA	87-99	Scaffaro et al., 2011; Janorkar et al., 2004
LDPE	99	Popelka et al., 2012
PTFE	109-116	Wu, 1982; Busscher, 1983

## D.5 References

Busscher, H.J., *et al*, *J. Coll. Interface Sci.*,1983, 95.

Janorkar, Amol V.; Luo, Ning.; Hirt, Douglas E. Surface Modification of an Ethylene-Acrylic Acid Copolymer Film: Grafting Amine Terminated Linear and Branched Architectures.” *Langmuir* 2004, 20, 7151-7158.

Popelka, Anton; Novak, Igor; Lehocky, Marian; Chodak, Ivan; Sedliacik, Jan; Gajtanska, Milada; Sedliacikova, Marian; Vesel Alenka; Junkar, Ita; Kleinova, Angela; Spirkova, Milena; Bilek, Frantisek. Anti-bacterial Treatment of Polyethylene by Cold Plasma for Medical Purposes. *Molecules*, 2012, 17, 762-785.

Scaffaro, Robert; Botta, Luigi; Lo Re, Giada; Bertani, Roberta; Milani, Roberto.; Sassi, Alessandro. Surface modification of poly (ethylene-co-acrylic acid) with amino-functionalized silica nanoparticles. *Journals of Materials Chemistry*, 2011, 21, 3849.

Wu, S. *Polymer Interface and Adhesion*, Marcel Dekker, New York, NY, 1982, p. 87.

APPENDIX E  
DETERMINATION OF OPTIMAL REACTION TIMES FOR PRELIMINARY EAA  
SURFACE MODIFICATION STEPS

## E.1 Determination of Optimal Reaction Times for Preliminary EAA Surface Modification Steps

Prior to grafting the light-sensitive polymers to the surface of EAA films, preliminary chemical transformations were required to modify the surface chemistry. For these preliminary reaction steps—conversion of carboxyl groups to acid chlorides and then to primary amines—it was important to optimize the reactions conditions. The focus was on identifying the shortest reaction time that allowed for complete reaction, as assessed by FTIR, in order to streamline the synthesis steps and minimize any side reactions or damage to the films. Figure E.1 illustrates the preliminary reaction steps: (1) conversion of  $-\text{C}(=\text{O})\text{OH}$  for the neat EAA film to  $-\text{C}(=\text{O})\text{Cl}$ , and (2) subsequent conversion of  $-\text{C}(=\text{O})\text{Cl}$  to an amide ( $-\text{C}(=\text{O})\text{N}$ ) with a terminal  $\text{NH}_2$ .

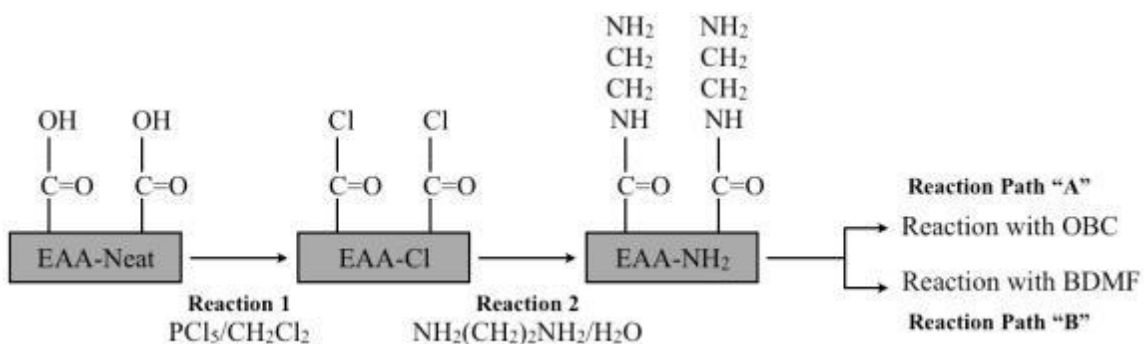


Figure E.1 Primary reaction steps for surface modification of EAA film: conversion of carboxylic acid to acid chloride using  $\text{PCl}_5$  and subsequent conversion to primary amines using ethylene diamine.

As seen in Figure E.1, the  $-\text{OH}$  in the EAA-Neat film was converted to  $-\text{Cl}$  using a 0.3 g/mL phosphorous pentachloride ( $\text{PCl}_5$ )/dichloromethane ( $\text{CH}_2\text{Cl}_2$ ) solution [Walters and Hirt, 2006]. This reaction is relatively quick, and the progression of the

reaction was monitored using ATR-FTIR. The right side of Figure E.1 indicates the reaction steps the films undergo after the initial primary reaction steps. These reaction paths (“A” and “B”) are described in more detail in section 5.4.2 of Chapter 5, “Surface Modification and Chemical Grafting of Poly (Ethylene co-acrylic acid) Films”. Figure E.2 shows ATR-FTIR spectra of the EAA-Cl film at various reaction times.

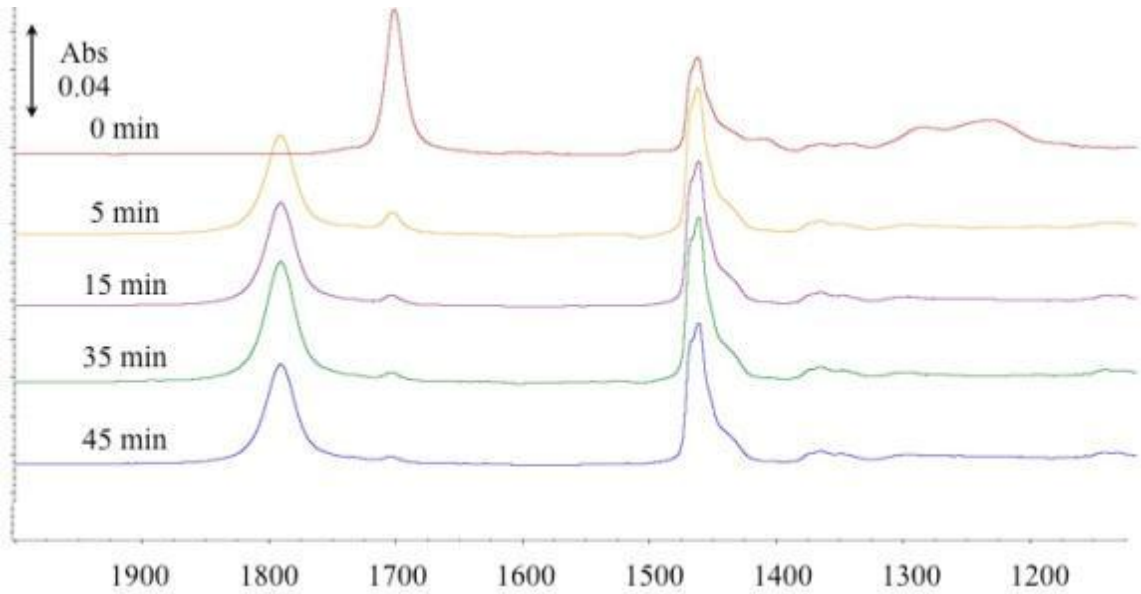


Figure E.2 ATR-FTIR spectra of EAA-Cl films at reaction times of 0, 5, 15, 35, and 45 minutes showing progressive decrease in the acid carbonyl (at  $\sim 1700 \text{ cm}^{-1}$ ) and increase in the acid chloride carbonyl (at  $\sim 1795 \text{ cm}^{-1}$ ).

Evaluating the spectra, the strong peak observed in the 0 min spectrum at  $\sim 1700 \text{ cm}^{-1}$  corresponds to the carbonyl stretch of carboxylic acid [Silverstein and Webster, 1998, Kupstov and Zhizhin, 1988] and the height of this peak decreases with reaction time. The  $\sim 1795 \text{ cm}^{-1}$  peak corresponds to the carbonyl stretch of acid chloride [Silverstein and Webster, 1998, Kupstov and Zhizhin, 1988]. As expected this peak is absent in the 0 min spectrum (EAA-Neat) but is present in all of the reacted film spectra,

and its intensity increases progressively with reaction time. Table E.1 lists the quantitative peak heights for the time intervals shown in Figure E.2.

Table E.1 Carbonyl peak height values for the transformation from carboxylic acid ( $1700\text{ cm}^{-1}$ ) to acid chloride ( $1795\text{ cm}^{-1}$ ) during the reaction of EAA with  $\text{PCl}_5$  to form EAA-Cl.

Film Reaction Time (minutes)	Peak Height (Abs.), Peak at $1700\text{ cm}^{-1}$	Peak Height (Abs.), Peak at $1795\text{ cm}^{-1}$
0	0.0377	0.0000
5	0.0058	0.0258
15	0.0028	0.0286
35	0.0018	0.0269
45	0.00600	0.0269

The measured acid chloride carbonyl peak height at 35 min and 45 min are equal, indicating the reaction is apparently complete at 35 min. To minimize any batch-to-batch variation in yields, all EAA- $\text{PCl}_5$  films were reacted for 45 min to ensure the reaction had gone to completion prior to proceeding with the next step.

The second preliminary reaction that needed to be optimized was the conversion of  $-(\text{C}=\text{O})\text{Cl}$  to  $-(\text{C}=\text{O})\text{N}$  with a terminal  $\text{NH}_2$ . As shown in Figure E.1, the EAA-Cl to EAA- $\text{NH}_2$  step was achieved using a 0.0025 g/mL ethylene diamine/water solution. This reaction progression was also monitored using ATR-FTIR. Figure E.3 shows the ATR-FTIR spectra for the EAA- $\text{NH}_2$  films at various reaction times.

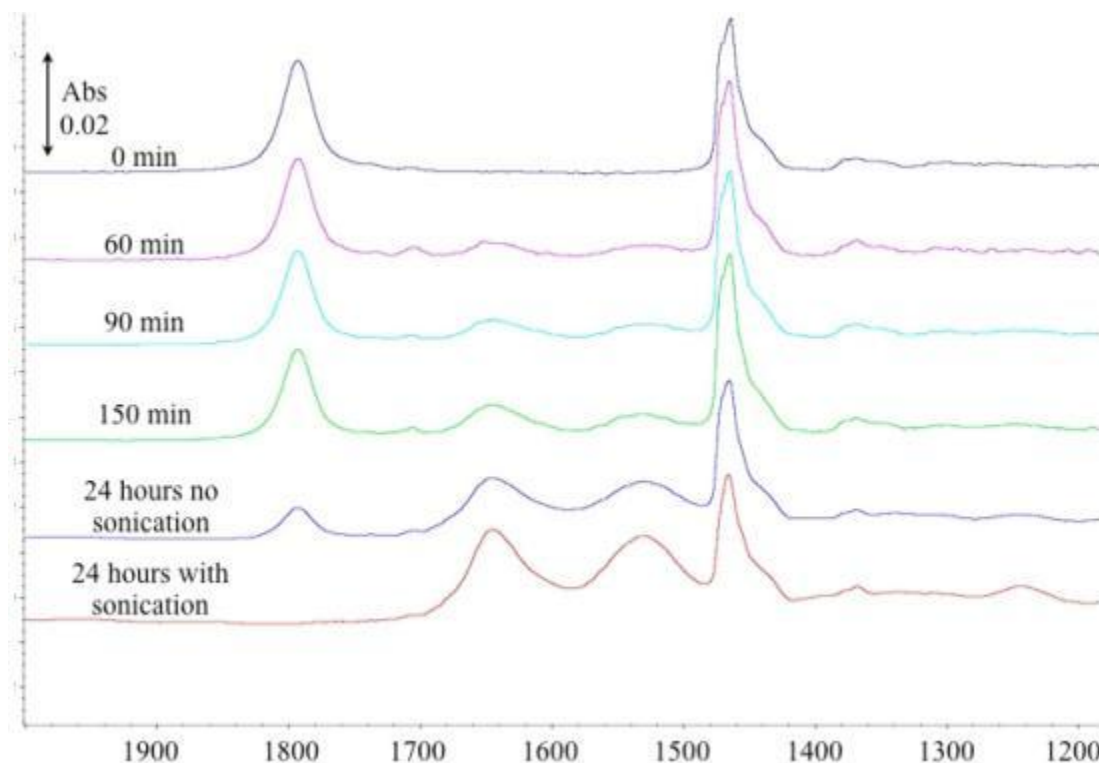
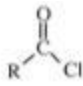
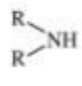
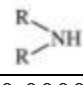


Figure E.3 ATR-FTIR spectra of EAA-NH<sub>2</sub> films at reaction times of 0, 60, 90, and 150 min and 24 hours—with and without sonication. Sonicated films had complete surface reaction with the ethylene diamine, while unsonicated films contained some unreacted surface -Cl groups (presence of peak at  $\sim 1800\text{ cm}^{-1}$ ).

Examining the spectra, the acid chloride peak from EAA-Cl can be seen in the 0 min spectrum at  $\sim 1800\text{ cm}^{-1}$ . As anticipated, this peak decreases with increasing time. Two peaks at  $\sim 1646\text{ cm}^{-1}$  and  $\sim 1530\text{ cm}^{-1}$  are not present in the 0 minute spectrum but is seen in all the other spectra, indicating the peak corresponds to the -NH<sub>2</sub> reacted films. These peaks indicate the formation of a secondary amide [Silverstein and Webster, 1998, Kupstov and Zhizhin, 1988], replacing the acid chloride of the EAA-Cl film, and increases in intensity as time increases. The secondary amide peaks begin to appear as early as 60 minutes, but even after 150 minutes the acid chloride peak was still present. The films were reacted for 24 hours and still showed the acid chloride peak. After

sonication for 24 hours, the acid chloride peak had receded and the secondary amide peaks were fully formed, indicating the reaction had gone to completion. Table E.2 gives numerical peak height values for the peaks of interest in the EAA-NH<sub>2</sub> reaction series.

Table E.2 Peak height values for functional groups of interest in the reaction of EAA-Cl to EAA-NH<sub>2</sub>.

Film Reaction Time (minutes)	Peak Height (Abs.), Peak at 1800 cm <sup>-1</sup> 	Peak Height (Abs.), Peak at 1646 cm <sup>-1</sup> 	Peak Height (Abs.), Peak at 1530 cm <sup>-1</sup> 
0	0.0269	0.0000	0.0000
60	0.0197	0.0020	0.0017
90	0.0192	0.0059	0.0037
150	0.0131	0.0078	0.0066
24 Hours, No Sonication	0.0054	0.0109	0.0091
24 Hours, With Sonication	0.0000	0.0182	0.0149



## E.2 References

Bruno, Thomas J.; Svoronos, Paris D.N. CRC Handbook of Fundamental Spectroscopic Correlation Charts. Taylor and Francis : Boca Raton, FL, 2006, Fig. 2.7

Kupstov, A.H.; Zhizhin, G.N. Handbook of Fourier Transform Raman and Infrared Spectra of Polymers. Elsevier: New York, 1988, p. 11.

Silverstein, R.M.; Webster, F.X. Spectrometric Identification of Organic Compounds; John Wiley & Sons Inc.: New Jersey, 1998, 99-102.

Walters, Keisha B.; Hirt, Douglas E. Grafting of End-Functionalized Poly(*tert*-butyl acrylate) to Poly (ethylene-*co*-acrylic acid) film. *Polymer* 47 (2006) 6567-6574.

APPENDIX F  
GRATING OF POLY(ETHYLENE GLYCOL DIACRYLATE) TO AMINE SURFACE-  
MODIFIED EAA FILMS

## F.1 Introduction

The grafting of poly(ethylene glycol diacrylate) (PEGD), a difunctional polymer, was initially going to be used to aid in the grafting of (bromomethyl)-9,9-dihexyl-9H-fluorene) (BDMF) to the amine-modified EAA films (EAA-NH<sub>2</sub>) through the terminal acrylate groups. However, successful reaction between BDMF and EAA-NH<sub>2</sub> was achieved without aid from the acrylate reactive groups of PEGD. This work can be found in section 5.4.2 of Chapter 5, “Surface Modification and Chemical Grafting of Poly(ethylene co-acrylic acid) Films”. While the PEGD reaction was not needed to grafting of PEGD to the EAA-NH<sub>2</sub> films, the reaction method was successful. The procedure and preliminary results are presented here since this reaction could be useful to another researcher.

## F.2 Results

Two different molecular weights of PEGD were investigated since it was suspected that the additional polymer length might affect the grafting of PEGD to EAA-NH<sub>2</sub> or the subsequent grafting of BDMF to the free terminal acrylate group of PEGD. The PEGD molecular weights examined were M<sub>n</sub> = 258 (n=4) and M<sub>n</sub> = 575 (n=11) (Sigma Aldrich, CAS 26570-48-9) referred to as PEGD258 and PEGD575, respectively. The chemical structure of PEGD is shown in Figure F.1.

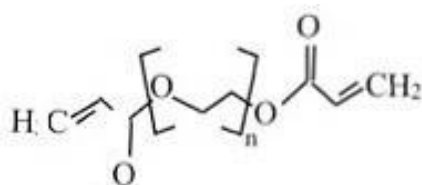


Figure F.1 Chemical structure of poly(ethylene glycol diacrylate) (PEGD).

For the grafting reaction, sodium hydroxide (NaOH) was used as a base catalyst. The molar ratio of PEGD to NaOH was 2:1, and both acetone and toluene were tested as the solvent. PEGD was in solution with the solvent at 5 mM. The films were reacted for 5 hours at 60 °C. on a hot plate. Due to the bulkiness of the PEGD chemical this reaction takes several hours. The films were enclosed in individual vials, constantly stirred using a magnetic stir bar, and were insulated with sand that was also heated to 60° C. The films were all reacted concurrently. At the conclusion of the reaction time, each film was removed with tweezers, rinsed three times with clean solvent, and then dried at room temperature in a vacuum oven (at a pressure of 30 mmHg). A schematic of the reaction steps in Figure F.2 shows that the terminal C=C group reduces to a single group to attach to the terminal –NH<sub>2</sub> of the film via the terminal carbon. The –NH<sub>2</sub> of the EAA-NH<sub>2</sub> film loses an –H in order to bond with the C of the acrylate on the PEGD molecule. This is a Michael's addition reaction [Russell et al., 2000, Mather et al., 2006]. ATR-FTIR spectroscopy was used to monitor the reaction progression.

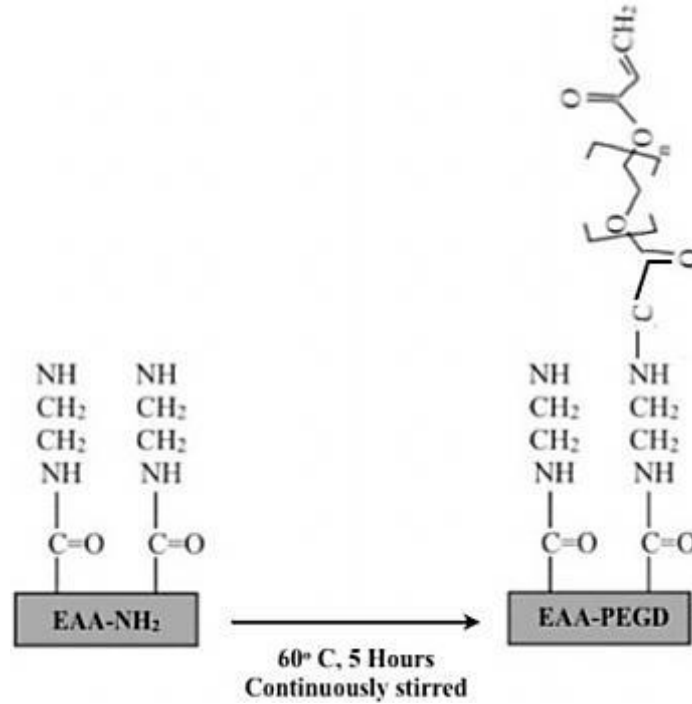


Figure F.2 Reaction scheme for the reaction of PEGD with EAA-NH<sub>2</sub>.

Figure F.3 shows the ATR-FTIR spectra for EAA-NH<sub>2</sub> (2) and several samples of EAA-PEGD (3a-4b) under different reaction conditions to illustrate the changes in surface functional groups. There are several spectral differences between EAA-NH<sub>2</sub> and the PEGD reacted films. Three peaks in particular are of interest in the PEGD-reacted films and located at approximately 1750 cm<sup>-1</sup>, 1240 cm<sup>-1</sup>, and 1020 cm<sup>-1</sup>. Based on the PEGD chemical structure and the proposed reaction scheme, these peaks are associated with the reaction of PEGD with the surface of EAA-NH<sub>2</sub> via covalent bonding. The peak at ~1750 cm<sup>-1</sup> corresponds to the C=O stretching vibration of ketones present in the PEGD structure [Bruno and Svoronos, 2006, Silverstein and Webster, 1998]. The peak at ~1240 cm<sup>-1</sup> corresponds to the C-O stretching vibration of the esters present in the PEGD structure [Bruno and Svoronos, 2006, Silverstein and Webster, 1998]. The vinyl (acrylate) groups present in the PEGD structure absorb at ~1020 cm<sup>-1</sup> [Bruno and

Svoronos , 2006, Silverstein and Webster, 1998]. Using ATR-FTIR, the presence of PEGD functional groups on the surface of the EAA-NH<sub>2</sub> films confirmed the grafting of PEGD to the EAA film surfaces.

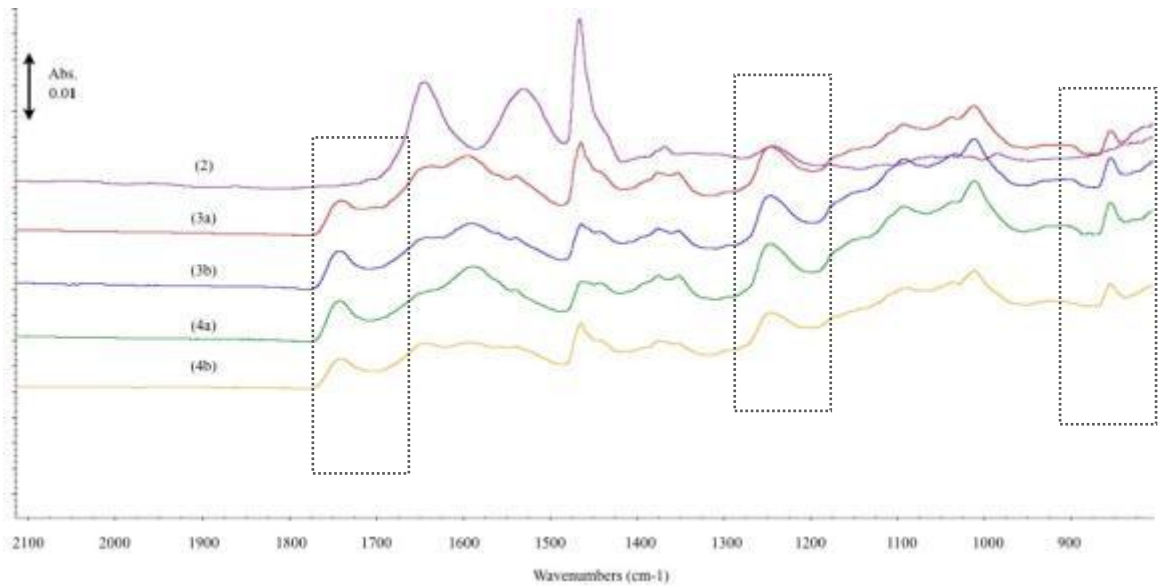


Figure F.3 ATR-FTIR spectra of EAA-NH<sub>2</sub> (2), EAA-PEGD575-Acetone (3a), EAA-PEGD575-Toluene (3b), EAA-PEGD258-Acetone (4a) and EAA-PEGD258-Toluene (4b). Spectral peaks of interest are boxed.

### F.3 References

Bruno, Thomas J.; Svoronos, Paris D.N. CRC Handbook of Fundamental Spectroscopic Correlation Charts. Taylor and Francis : Boca Raton, FL, 2006, Fig. 2.2.

Mather, Brian D.; Viswanathan, Kalpana; Miller, Kevin M.; Long, Timothy E. Michael addition reactions in macromolecular design for emerging technologies. *Progress In Polymer Science*, 2006, 31, 487-531.

Russell, Ryan J.; Sirkar, Kaushik; Pishko, Michael V. Preparation of nanocomposite poly(allylamine)-poly(ethylene glycol) thin films using Michael addition. *Langmuir*, 2000, 16, 4052-4054.

Silverstein, R.M.; Webster, F.X. Spectrometric Identification of Organic Compounds; John Wiley & Sons Inc.: New Jersey, 1998, pp. 81, 91, 92, 98.

APPENDIX G  
NANOPARTICLES IN DRUG DIFFUSION



## **G.1 Introduction**

Nanoparticles have attracted increased interest in recent decades for a variety of applications. They have been investigated for use in many applications, such as chemicals (catalysts), biology (biosensing, bioimaging) [De et al., 2008], semiconductors, and drug delivery [Zhang et al., 2011] and have the potential for applications in water purification, medical diagnostics (quantum dots), and generation and conservation of energy [Card et al., 2008]. Nanoparticles are already present in many consumer products, including ultraviolet B radiation-protective sunscreen, topical silver nanoparticles for antimicrobial and odor-reducing applications, and cosmetics [DeLouise, 2012; Card et al., 2008]. The small size of nanoparticles (>100-200 nm) makes them adaptable for a multitude of functions. Of particular interest is the use of nanoparticles in inhalation drug delivery systems for treatment of pulmonary conditions. Some valuable properties of nanoparticles, such as large relative surface area [Zhang et al., 2011], good solubility in pulmonary mucus [Card et al., 2008], and surface morphology [Chow et al., 2007] make them a promising material for inhalation drug delivery.

## **G.2 Characteristics of Nanoparticles**

Nanoparticles have the ability to be optimally designed for particular applications. Characteristics such as numerous particle formation techniques, narrow particle size distribution, improved drug stability, enhanced bioavailability, continual release and precise site targeting allow for optimization of nanoparticle systems [Chow et al., 2007]. The ability to engineer particles is advantageous for the designing of final drug products and their precise characteristics to specific applications, the consistency of particle properties, and development of treatment techniques for respiratory drug delivery

systems. For example, large surface area, one of the more influential properties of nanoparticles, results in faster drug release and shorter times to reach high drug concentrations at the absorption site [Zhang et al., 2011]. It also increases solubility and dissolution rate and minimizes macrophage clearance [Zhang et al., 2011].

Not all characteristics of nanoparticles positively affect the path of nanoparticles within the respiratory system. Size-related challenges such as exhalation and mucociliary clearance are frequently encountered. Submicron particles, such as nanoparticles, have a higher risk of being exhaled due to their small size [Chow et al, 2007]. Holding the breath after inhalation helps the nanoparticles deposit before being exhaled. Nanoparticles must also be engineered with specific properties such as shape, hydrophobicity and particle diameter [Chow et al., 2007] that are particularly advantageous for the desired quick dissolution or sustained release drug behaviors that are pertinent to each application. By considering these properties and designing the nanoparticle systems accordingly, the small size challenges of nanoparticles can be overcome and even beneficial.

An additional challenge that is encountered with nanoparticles is agglomeration. Nanoparticles can assemble into particles larger than 1 micron [Card et al., 2008]. Due to their large surface area, nanoparticles possess high Gibbs free energy, making it challenging to prevent agglomeration and prevent formulation instability [Zhang et al., 2011]. Nanoparticle surface modifications can be designed to limit interactions between particles, lessening the tendency for agglomeration and therefore increasing the probability for inhalation and deposition in the lungs [Card et al., 2008]. In some instances, the nanoparticle susceptibility to agglomeration may be regarded as a positive characteristic. Controlling agglomeration in nanoparticles can result in nanoparticle agglomerate dry powders that can be customized to the desired physicochemical

characteristics for aerosol delivery and dissolution [El-Gendy et al., 2011]. An example of this with asthma drugs is highlighted in Section G.4, Nanoparticles in Inhalation Medicine.

As seen in Chapter Three with drug particles, other factors affect the deposition and diffusion on inhaled particles. Factors such as molecular weight, pH, and charge influence the path of the particulates in the lung. An inverse relationship between molecular weight and diffusion coefficient has been regularly reported [Khanvilkar et al., 2001]. It has also been found that hydrophobic particles have lower permeabilities due to the hydrophobic nature of the mucus [Khanvilkar et al., 2001; Norris and Sinko, 1997]. Additionally, pH was found to influence the diffusion of drugs across the membrane. An increase in pH produced an increase in diffusion coefficient and a decrease in lag time [Shaw et al., 2005].

### **G.3 Fate of Nanoparticles in the Lung**

The advantages of pulmonary lung delivery have previously been discussed [See Chapters 1-3]. Using nanoparticles as a vehicle for drug delivery to the lungs presents vast opportunities for enhanced drug efficiency. The path of nanoparticles in the lung must be investigated so the particles can be engineered with the most essential properties in mind. Nanoparticles, unlike larger drug particles, will deposit primarily by diffusion in the lung after inhalation. Due to the small size of nanoparticles, convection, a critical characteristic in micron-scale inhaled particles, is no longer a dominant factor [Zhang et al., 2011]. It is important to note, however, that the deposition of micron-sized agglomerates of nanoparticles is controlled by convection [Zhang et al., 2011].

Upon landing on the pulmonary mucosal surface, the physiochemical characteristics of the nanoparticles, particularly the size and surface chemistry, will ultimately dictate the rate and efficiency of diffusion across the mucus layers. Ideally, the mucus layer will enhance dissolution of the particle and help it descend further into the mucus, first through the upper gel phase of the mucus layer and eventually through the sol phase. Agglomerates may remain in the gel layer, or separate back into individual nanoparticles and follow the same path of dissolution and absorption [Zhang et al., 2011]. The rate of nanoparticle absorption depends on site of deposition in the lung (varying mucus layer and epithelial wall thicknesses) as well as nanoparticle properties such as polarity and solubility. Polar/hydrophilic nanoparticles dissolve readily in mucus [Zhang et al., 2011]. After absorption, the particle is uptaken by the epithelium or alveolar macrophages [Zhang et al., 2011]. Some nanoparticles may transport across the epithelia and into the bloodstream. From the bloodstream nanoparticles may reach organs or sites such as lymph nodes or bone marrow [Sung et al., 2007].

#### **G.4 Nanoparticles in Inhalation Medicine**

The vast amount of research that has been published has demonstrated the potential of nanoparticles for treatments of lung conditions. In 2007 alone over 200 scientific publications related to engineered nanoparticles were published [Card et al., 2008], a significant increase from the late 1990s when annual publications were below fifty for engineered nanoparticle studies. Since initial investigations into the use of nanoparticles for drug delivery began in the 1960s [Sung et al., 2007], several methods of delivering nanoparticles into the lung for therapeutic actions have been developed. Nanoparticles can dissolve, entrap, or encapsulate the drug or be physically or chemically

adsorbed to the active drug [Sung et al., 2007; Parveen et al., 2012]. Their small size allows them to efficiently penetrate barriers and into individual cells, which reduces negative side effects and increases the therapeutic effect [Parveen et al., 2012].

Nanoparticles used in biological systems are typically synthetic biodegradable polymeric particles, and the degradation of these materials can be manipulated to control the drug release rate [Sung et al., 2007]. The wide range of delivery methods have enabled nanoparticles to be effectively designed and researched as potential methods for the treatment of many pulmonary illnesses, including lung cancer, tuberculosis, and asthma. The broad spectrum of diseases with nanoparticle research is a significant contribution to the future of inhalation nanoparticle treatments. Several examples of nanoparticle-based delivery methods currently being studied are outlined below.

Anticancer drugs are known to cause severe negative side effects in cancer patients. Studies have been conducted for the potential uses of inhalation routes for delivery of the chemotherapy drugs. Due to unresolved systemic side effects and toxicity issues that limit the amount of drug that can be administered, pulmonary delivery systems still face many challenges before they can be employed in regular cancer treatments [Roa et al., 2011]. Nanoparticles, however, can be targeted to specific cell types and combine the concepts of specific directed drug delivery and the benefits of using nanoparticles for lung cancer treatment [Roa et al., 2011]. A study was conducted using doxorubicin-loaded nanoparticles in H460 and A459 lung cancer cells in mice. It was determined that inhaled doxorubicin nanoparticle powders increased survival time in affected mice compared to intravenous administration of the same dosage of drug [Roa et al., 2011].

Nanoparticles have also been investigated in the treatment of tuberculosis (TB). Therapeutic plasma levels of antitubercular drugs increased for up to 6 days when guinea

pigs took a single inhaled dose of aerosolized poly (DL-lactide-co-glycolide) nanoparticles doped with the drugs isoniazid, rifampicin, or pyrazinamide [Card et al., 2008]. Repeated inhalation treatments had higher levels of therapeutic plasma drug levels success than more frequent oral administration of the antitubercular drugs [Card et al., 2008]. Another study (*in vivo*) on guinea pigs found that the same drugs (isoniazid, rifampicin, or pyrazinamide) were more effective than oral drug administration when encapsulated in alginate nanoparticles and administered through inhalation [Zahoor et al., 2005; Card et al., 2008]. By investigating the use of nanoparticles to (1) target alveolar macrophages that harbor TB bacilli and (2) sustain high drug concentrations in the lung [Misra et al., 2011], the future of nanoparticle aerosol treatment for TB remains promising.

Asthma is yet another condition that nanoparticles have been demonstrated as a successful treatment option. Most pharmaceutical drugs used to treat asthma have particle sizes between 1-5  $\mu\text{m}$ , which is the ideal particle size to prevent exhalation or mucociliary clearance that occurs with smaller particles [El-Gendy et al., 2011]. To avoid the clearance of nanoparticles from the lung, nanoparticle size asthma drugs have been purposely agglomerated and evaluated for their potential as treatments for asthma. Suspensions containing agglomerated nanoparticles were used to develop aerosols of the asthma medications albuterol and fluticasone. Additionally, an aerosolized blend of dried agglomerated fluticasone and albuterol in solution was evaluated [El-Gendy et al., 2011]. Powders of the single drug agglomerates or combined therapeutics possessed desirable aerodynamic properties, particle sizes, and also increased surface area resulting in 75% total deposition compared to only 22-30% total deposition as has been reported for albuterol administered through metered-dose inhaler [Dhand, 2005]. The powders of the

single drug agglomerates or combined therapeutics also experienced increased dissolution [El-Gendy et al., 2011] over traditional micron-sized single drug particles. The formulation presented in this thesis presents promising data and conclusions that immensely support further development of nanoparticles as treatments for asthma.

## **G.5 Toxicity of Nanoparticles**

Nanoparticle toxicity is a highly debated topic in regards to patient side effects in nanoparticle research. Much of the nanoparticle toxicity investigation stems from negative environmental factors such as air pollution, industrial exhaust, and naturally occurring nanoparticles (viruses or allergens [DeLouise, 2012]). The ability of these ambient ultrafine particles (particles with an aerodynamic diameter  $>100$  nm) to diffuse through the pulmonary mucus and through the epithelial and endothelial cells to organs and even the central nervous system is cause for concern and further investigation. Due to the large surface area of nanoparticles, which as previously been discussed, nanoparticles are biologically active and have the physiochemical properties to enter through the lungs and other body systems. Environmental (urban and industrial) nanoparticles are generally insoluble in the pulmonary mucus and lung and non-biodegradable materials, such as carbon black, carbon nanotubes, ultrafine asbestos, silica, and metal-based nanoparticles such as titanium dioxide [Card et al., 2008]. Therapeutic nanoparticles are biodegradable [Sung et al., 2007] and therefore affect the body differently.

In light of the detrimental effects environmental nanoparticles have demonstrated, the effects of engineered nanoparticles are also under investigation. Engineered nanoparticles have distinctive and specifically designed properties that render them valuable to treat lung ailments and are biologically degradable [Sung et al., 2007], unlike

environmental nanoparticles. While engineered nanoparticles could potentially trigger adverse pulmonary effects on the respiratory system, most engineered nanoparticles are intended for treatment purposes and are designed to avoid any detrimental effects. There is an extreme lack of knowledge regarding toxicity of engineered nanoparticles and a set of guidelines needs to be established in order to have a common scale to compare potential toxicities of multiple types of nanoparticles [Card et al., 2008].

## **G.6 Conclusions**

From the concise summary of published studies and nanoparticle characteristics presented here, it is clear that the exploration into nanoparticle-based pulmonary lung drug delivery applications is only just beginning. Initial results have yielded positive results for the ability of nanoparticle-based therapies to improve respiratory conditions, and have provided a foundation to direct the development of future nanoparticle-based drug delivery methods. Engineered particles can overcome obstacles of sub-micron sized particles and existing aerosol drugs. The precise design and targeted drug delivery potential make nanoparticulate therapy an area that deserves further investigation.

A successful, validated method for the determination of diffusion coefficients for aerosol drugs through a representative pulmonary mucus has been previously discussed in Chapter 6 of this thesis. This method could also be applied to other biological fluids of interest. These diffusivities are necessary to model the transport properties of these drugs and in turn, nanoparticles in assessing their bioavailability in the lung, regardless of origin (environmental or engineered). Modeling the diffusion coefficients of nanoparticles will enhance past and present studies on the potential of nanoparticles for



drug delivery as well as studying the effects of industrial or naturally occurring nanoparticles on the lung.

## G.7 References

- Card, Jeffrey W.; Zeldin, Darryl C.; Bonner, James C.; Nestmann, Earle R. Pulmonary applications and toxicity of engineered nanoparticles. *American Journal of Physiology: Lung Cellular and Molecular Physiology*, 2008, 295, L400-L411.
- Chow, Albert H. L.; Tong, Henry H.Y.; Chattopadhyay, Pratibhash; Shekunov, Boris Y. Particle engineering for pulmonary drug delivery. *Pharmaceutical Research*, 2007, 24, 411-437.
- De, Mrinmoy; Ghosh, Partha S.; Rotello, Vincent M. Applications of nanoparticles in biology. *Advanced Materials*, 2008, 20, 4225-4241.
- DeLouise, Lisa A. Applications of nanotechnology in dermatology. *Journal of Investigative Dermatology*, 2012, 132, 964-975.
- Dhand MD, Rajiv. Inhalation therapy with metered-dose inhalers and dry powder inhalers in mechanically ventilated patients. *Respiratory Care*, 2005, 50, 1331-1345.
- El-Gendy, Nashwa; Pornputtapitak, Warangkana; Berkland, Cory. Nanoparticle agglomerates of fluticasone propionate in combination with albuterol sulfate as dry powder aerosols. *European Journal of Pharmaceutical Sciences*, 2011, 44, 522-533.
- Khanvilkar, Kavita; Donovan, Maureen D.; Flanagan, Douglas R. Drug transfer through mucus. *Advanced Drug Delivery Reviews*, 2001, 48, 173-198.
- Misra, Amit; Hickey, Anthony J.; Rossi, Carlo; Tereda, Hiroshi; Makino, Kimiko; Fourie, P. Bernard; Colombo, P. Bernard. Inhaled drug therapy for treatment of tuberculosis. *Tuberculosis*, 2011, 91, 71-81.
- Norris, D.A.; Sinko, P.J. Effect of size, surface charge, and hydrophobicity on the translocation of polystyrene microspheres through gastrointestinal mucin. *Journal of Applied Polymer Science*, 1997, 63, 1481-1492.
- Parveen, Suphiya; Misra, Ranjita; Sahoo, Sanjeeb K. Nanoparticles: a boon to drug delivery, therapeutics, diagnostics, and imaging. *Nanomedicine: Nanotechnology, Biology, and Medicine*, 2012, 8, 147-166.
- Roa, Wilson H.; Azarmi, Shirzad; Al-Hallak, M.H.D. Kamal; Finlay, Warren H.; Magliocco, Anthony M.; Lobenberg, Raimar. Inhalable nanoparticles, a non-invasive approach to treat lung cancer in a mouse model. *Journal of Controlled Release*, 2011, 150, 49-55.
- Shaw, Lance R.; Irwin, William J.; Grattan, Tim J.; Conway, Barbara R. The influence of excipients on the diffusion of ibuprofen and paracetamol in gastric mucus. *International Journal of Pharmaceutics*, 2005, 290, 145-154.

Sung, Jean C.; Pulliam, Brian L.; Edwards, David A. Nanoparticles for drug delivery to the lungs. *TRENDS in Biotechnology*, 2007, 25, 563-570.

Zahoor, A.; Sharma, S.; Khuller, G.K. Inhalable alginate nanoparticles as antitubercular drug carriers against experimental tuberculosis. *International Journal of Antimicrobial Agents*, 2005, 26, 298-303.

Zhang, Jian; Wu, Libo; Chan, Hak-Kim; Watanabe, Wiwik. Formation, characterization, and fate of inhaled drug nanoparticles. *Advanced Drug Delivery Reviews*, 2011, 63, 441-455.